


Fall 11-25-2016

# DEVELOPMENT OF METAL MATRIX COMPOSITE GRIDLINES FOR SPACE PHOTOVOLTAICS

Omar K. Abudayyeh  
*University of New Mexico*

Follow this and additional works at: [https://digitalrepository.unm.edu/cbe\\_etds](https://digitalrepository.unm.edu/cbe_etds)

 Part of the [Chemical Engineering Commons](#), and the [Materials Science and Engineering Commons](#)

---

## Recommended Citation

Abudayyeh, Omar K.. "DEVELOPMENT OF METAL MATRIX COMPOSITE GRIDLINES FOR SPACE PHOTOVOLTAICS."  
(2016). [https://digitalrepository.unm.edu/cbe\\_etds/58](https://digitalrepository.unm.edu/cbe_etds/58)

This Dissertation is brought to you for free and open access by the Engineering ETDs at UNM Digital Repository. It has been accepted for inclusion in Chemical and Biological Engineering ETDs by an authorized administrator of UNM Digital Repository. For more information, please contact [disc@unm.edu](mailto:disc@unm.edu).

**Omar Kamal Abudayyeh**

*Candidate*

---

**Engineering**

*Department*

---

This dissertation is approved, and it is acceptable in quality and form for publication:

*Approved by the Dissertation Committee:*

Sang M. Han, Chairperson

---

Ganesh Balakrishnan

---

Sang Eon Han

---

David M. Wilt

---

**DEVELOPMENT OF METAL MATRIX COMPOSITE  
GRIDLINES FOR SPACE PHOTOVOLTAICS**

**BY**

**OMAR KAMAL ABUDAYYEH**

B.A., Chemistry, University of New Mexico, 2009  
M.S., Chemical Engineering, University of New Mexico, 2015

DISSERTATION

Submitted in Partial Fulfillment of the  
Requirements for the Degree of  
**Doctor of Philosophy**

**Engineering**

The University of New Mexico  
Albuquerque, New Mexico

**December, 2016**

## DEDICATION

*Ephesians 1:3, “Blessed be the God and Father of our Lord Jesus Christ, who has blessed us with every spiritual blessing in the heavenliest in Christ.”*

I dedicate this work to my wonderful parents, Dr. Kamal B. Abudayyeh and Mrs. Hilda J. Akrouk, for their amazing love, support, and encouragement throughout my life. Thank you for believing in me and teaching me to believe in myself, in God, and in my dreams. I love you both endlessly.

I also dedicate this work to my precious love, my fiancée Yasmin N. Nasrat, for her never ceasing love, marvelous inspiration, and enduring patience throughout this entire time. Thank you my love!

## ACKNOWLEDGMENT

I wholeheartedly acknowledge Prof. Sang M. Han, my advisor and dissertation chair, for his continued support and valuable mentoring throughout all the years. Thank you, Prof. Han, for allowing me this amazing opportunity to be part of your research group.

I thank Mr. Dave M. Wilt from the Air Force Research Laboratory for the many valuable discussions and for allowing me access to conduct my research at the state-of-the-art AFRL facilities. It has been an honor working with you Mr. Wilt over the past 4 years.

I thank Dr. Geoffrey K. Bradshaw from the AFRL for the long hours of training to perform solar cell characterization and developing the mechanical setup for cracking cells.

I thank 1<sup>st</sup> Lt. Nathan D. Gapp from the AFRL for his efforts in creating the strain failure test setup and performing the initial pull tests.

I thank Mr. Ian Simson and Mr. Neil Snyder from the Advanced Power Generation Laboratory at the AFRL for their help with various projects.

We acknowledge a generous financial support from the Air Force Research Laboratory (FA9453-14-1-0242) to conduct this engineering research.

# **DEVELOPMENT OF METAL MATRIX COMPOSITE GRIDLINES FOR SPACE PHOTOVOLTAICS**

**By**

**Omar Kamal Abudayyeh**

**B.A., Chemistry, University of New Mexico, 2009**  
**M.S., Chemical Engineering, University of New Mexico, 2015**  
**Ph.D., Engineering, University of New Mexico, 2016**

## **ABSTRACT**

Space vehicles today are primarily powered by multi-junction photovoltaic cells due to their high efficiency and high radiation hardness in the space environment. While multi-junction solar cells provide high efficiency, microcracks develop in the crystalline semiconductor due to a variety of reasons, including: growth defects, film stress due to lattice constant mismatch, and external mechanical stresses introduced during shipping, installation, and operation. These microcracks have the tendency to propagate through the different layers of the semiconductor reaching the metal gridlines of the cell, resulting in electrically isolated areas from the busbar region, ultimately lowering the power output of the cell and potentially reducing the lifetime of the space mission. Pre-launch inspection are often expensive and difficult to perform, in which individual cells and entire modules must be replaced. In many cases, such microcracks are difficult to examine even with a thorough inspection. While repairs are possible pre-launch of the space vehicle, and even to some extent in low-to-earth missions, they are virtually impossible for deep space missions, therefore, efforts to mitigate the effects of these microcracks have substantial

impact on the cell performance and overall success of the space mission. In this effort, we have investigated the use of multi-walled carbon nanotubes as mechanical reinforcement to the metal gridlines capable of bridging gaps generated in the underlying semiconductor while providing a redundant electrical conduction pathway. The carbon nanotubes are embedded in a silver matrix to create a metal matrix composite, which are later integrated onto commercial triple-junction solar cells.

## TABLE OF CONTENTS

<b>CHAPTER 1 INTRODUCTION .....</b>	<b>1</b>
Multi-Junction Technology Overview .....	4
Inverted Metamorphic Multi-Junction Cells .....	8
Radiation Resistance of III-V .....	10
Effects of Microcracks on Solar Cells .....	11
<b>CHAPTER 2 CYANIDE-FREE SILVER ELECTROPLATING.....</b>	<b>16</b>
Background.....	16
The Electrolyte Double-Layer .....	19
Experimental Methods and Results .....	23
Direct Electroplating on Small-Featured PV Gridlines .....	29
Initial Optimization of Ag Deposition without use of Photoresist .....	30
Optimization of Ag Deposition on Solar cells using Photoresist .....	32
Conclusion .....	35
<b>CHAPTER 3 CARBON NANOTUBES CHEMICAL FUNCTIONALIZATION AND DEPOSITION.....</b>	<b>37</b>
Introduction .....	37
Experimental Methods and Results .....	39
Carbon Nanotubes Chemical Functionalization .....	39
Carbon Nanotubes Deposition Methods .....	42



Electrodeposition of CNT-COO <sup>-</sup> .....	43
Nanospreading Technique .....	45
Drop-Casting Method .....	49
Spray-Coating Technique .....	51
<b>CHAPTER 4 DEVICE INTEGRATION AND CHARACTERIZATION.....</b>	<b>64</b>
Electromechanical Characterization .....	64
MMC Integration on PV Cells .....	72
Solar Cell Characterization Methods .....	77
Effects of Microcracks on Performance of TJ Solar Cells .....	81
Experimental Methods .....	82
Results and Discussion .....	85
Single-Crack .....	85
Thermal Mismatch Multi-Cracking .....	90
Effects of Microcracks on MMC-Enhanced TJ Solar Cells .....	93
Conclusion .....	100
<b>References .....</b>	<b>101</b>

## **Chapter 1**

### **Introduction**

Photovoltaic (PV) solar cells have evolved throughout the years from the use of low efficiency silicon (Si) based devices to more complex and higher efficiency III-V solar cells. Shortly after the fabrication of the first solar cells at Bell Laboratories in the early 1950s [1], the application of solar cells to power satellites soon followed with the solar-powered Vanguard I in 1958 [2]. However, in the space environment solar cells suffer degradation due to the bombardment by fluxes of electrons and protons and by high energy particles [3]. Upon collision with nuclei these high energy particles create primary defects, such as interstitials and vacancies [4]. The resulting defects introduce energy traps deep into the bandgap of the semiconductor which act as recombination sites for minority carriers created by light with majority carriers. This degradation due to radiation in the space environment has motivated the search within the space community to find materials with greater tolerance to such high energy radiation [5].

Depending on the space vehicle location within the space environment, PV cells are required to have specific operational requirements. Earth-orbiting space missions are divided into three main categories: low-earth orbit (LEO), geosynchronous earth orbit (GEO), and mid-altitude earth orbit (MEO), with each mission having a different orbital environment [5]. LEO missions are flown at altitudes ranging from 300-500 km up to 2000 km. These orbits are characterized by low levels of radiation damage from trapped electrons and protons and 6000 thermal cycles encountered by satellites per year. Therefore, PV cells in LEO environment are required to have good beginning-of-life (BOL) efficiencies and good thermal cycle survivability. The GEO environment raises a

different concern and requirements on PV cells in which radiation damage, primarily from trapped electrons poses the biggest problem for PV devices. The temperature extremes encountered in GEO, although more extreme than in LEO, are of a lesser concern as they occur only 100 times per year and only over a short portion of the year. Hence, the most important characteristic of solar cells for these missions is a high end-of-life (EOL) efficiency, a characteristic that can be achieved by significantly improved resistance to radiation damage. The MEO environment is the most problematic of all three in that it resides in the environment with high radiation damage and many thermal cycles, combining the worst problems encountered in LEO and GEO.

In comparison to terrestrial PVs, solar cells in the space environment face a unique set of performance requirements, primarily having the highest possible power output with regard to mass and surface area while exhibiting as little degradation as possible due to space radiation during lifetimes of up to 15 years [6]. During the early 1990s, commercial satellite power requirements increased by 200 – 400%, with power systems capable of generating 5 – 15 kW at the end-of-life (EOL) [7]. Solely increasing the area of solar array is not an ideal solution to meet these new energy demands due to the impact on spacecraft operation, stowage volume, and weight. With estimated launch costs of \$11K/kg in LEO and \$66k/kg into GEO [5], weight is clearly important to the power system costs. Hence, efforts in reducing weight of solar arrays have a substantial impact on the launch costs. A more suitable alternative is the use of higher-efficiency solar cell design, that is both manufacturable and meets the requirements of operation in the space environment. Significant gains in spacecraft performance at lower costs can be achieved with successful development of ultra-lightweight, thin-film flexible solar arrays which

require high efficiency, flexible, thin-film solar cells that are easily integrated onto the arrays. Efforts have been made on both fronts within the PV community to create higher efficiency cells that are more radiation tolerant while reducing the weight of the modules and that of PV cells by creating thin-film cells. Some examples of thin-film, flexible, and high efficiency cells will be presented later.

Monocrystalline Si solar cells have been the cells of choice for space missions for a long time as they were the highest efficiency cells available. With device optimization such as rear-side point contacts, back surface reflectors, textured surfaces for increased light absorption and so on [8] the efficiency of such devices was increased up to 18%. It should be noted that all reported efficiencies measurement for space use are based on the air mass zero (AM0) sun spectrum, a reference spectrum of the solar irradiance without the effect of a filtering air [9]. However, Si cells EOL efficiency could not be improved past 13% following a 15-year radiation dose in the GEO environment. Si, being an indirect band gap material, requires sufficient material thickness for complete light absorption. Due to radiation, the diffusion length necessary to collect all minority carriers is not maintained.

A PV device is practically a  $p-n$  junction in which light gets absorbed in a region of the semiconductor material near the surface, where electron-hole pairs are generated as light quanta are absorbed. If their recombination is prevented the electron-hole pair can reach the junction where they can be separated by an electric field [10, 11]. This process is shown schematically in Fig. 1. Current is generated in a solar cell (light-generated current) firstly by the absorption of incident photons to create an electron-hole pair, and secondly by collecting these carriers while preventing their recombination. The

carriers are prevented from recombining by using the  $p-n$  junction to spatially separate them using the electric field that exists at the junction. As the light-generated minority carrier diffuse to the  $p-n$  junction they get swept away by the electric field becoming at this point majority

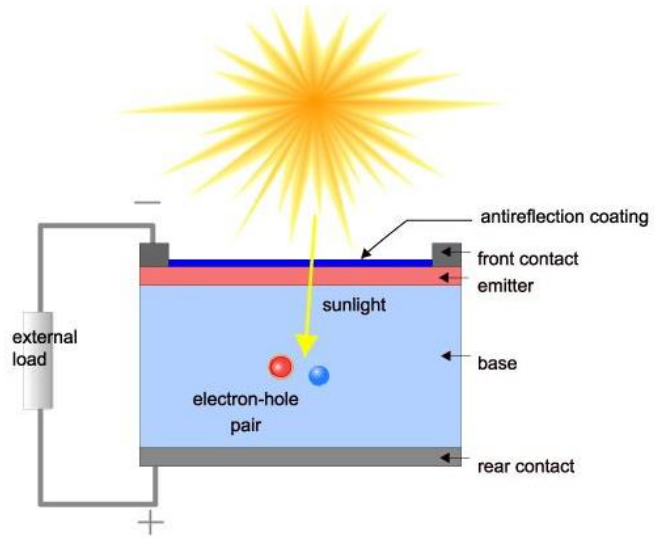


**Fig. 1.** Schematic of a photovoltaic solar cell showing emitter (n-type), base (p-type), front and rear contacts, and antireflection coating. Source PVEducation.org.

carriers. The light generated current is determined primarily by the minority-carrier transport, and depends on the minority-carrier lifetime ( $\tau$ ). Carriers generated within the diffusion length ( $L$ ) of the junction are collected, while the rest is lost by recombination ( $L = D \tau^{1/2}$ ), where  $D$  is the minority-carrier diffusion constant. Due to radiation, the diffusion length ( $L$ ) gets reduced. This reduction in  $L$  represents the most significant part of the damage due to radiation. The behavior of  $L$  due to radiation depends mostly on the material and the type of radiation.

### Multi-Junction Technology Overview

The use of III-V direct band gap semiconductor material has greatly overcome the efficiency limitation of non-direct band gap ones such as Si. In 1961 Shockley-Queisser (SQ) proposed a limit that predicted the theoretical efficiency of a solar cell using a single  $p-n$  junction to collect power from the cell. The limit calculates a solar conversion efficiency of 33.7 % [12], which corresponds to a single  $p-n$  junction with band gap 1.34

eV. To increase the cell efficiency past the SQ-limit the use of multijunction PV cells has been proposed, in which the solar spectrum is split using solar cells that are optimized to each section of the spectrum. The cells can either be individual cells or cells connected in series. As the number of bandgaps increases the efficiency of the stack also potentially increases [13].

Since 2000 [14], III-V multi-junction cells have been used almost exclusively for space operation. In brief the multi-junction technology involves combining cells with different bandgaps in series, almost doubling the cell efficiency. Electrically, these cells are serial connections of multiple subcells, which are separated by a tunnel junction. The materials chosen for these cells are GaInP<sub>2</sub>/GaAs/Ge, in which the GaInP<sub>2</sub> can be grown lattice-matched on GaAs minimizing dislocations which in turn impact the carrier-lifetime, along with single-crystalline Ge as the growth substrate [6]. Fig. 2 shows the splitting of AM0 spectrum achieved with this combination of bandgaps.

The GaInP/GaAs dual-junction (DJ) cells have reached efficiencies of 23% at AM0 for space applications [15]. DJ GaInP/GaAs/Ge cells are fabricated on low-cost, high-strength, Ge substrate making them suitable for large-volume production. DJ solar cell technology has advanced rapidly,

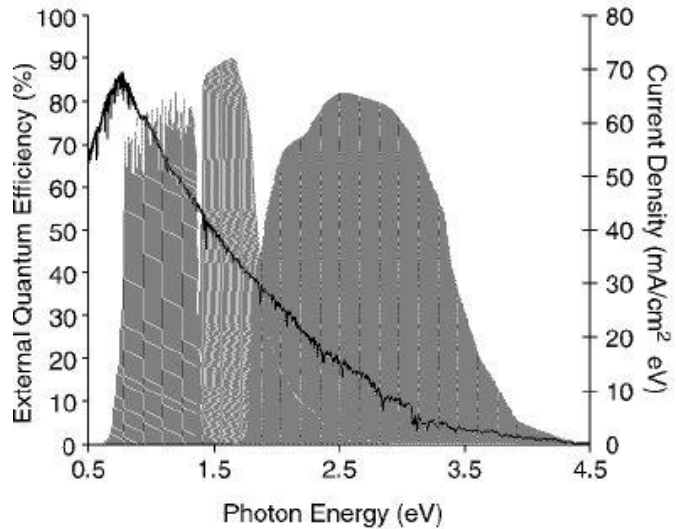


**Fig. 2.** AM0 spectrum along with current produced by each subcell. This current is obtained by integrating external quantum efficiency (EQE) curves with AM0 current density curve [6].

overtaking Si and GaAs single-junction cells reaching a level of 325kW/year at *Spectrolab* [7]. The success of this technology lies in the ability to grow these multi-junction solar cell structures in high volume by metal organic vapor phase

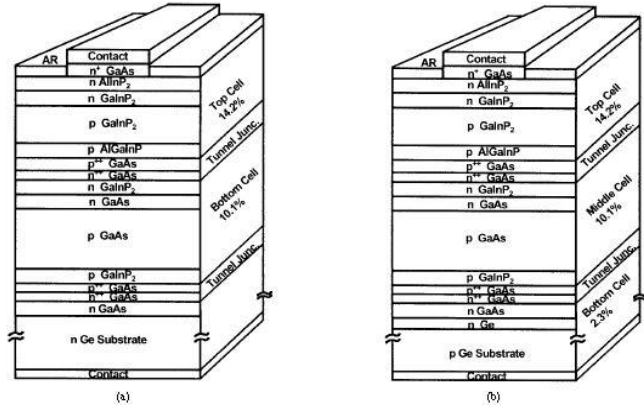


Fig. 3. Schematic cross-section of (a) DJ and (b) TJ cells [7].

epitaxy (MOVPE) [16, 17]. Triple junction (TJ) GaInP/GaAs/Ge cells with active Ge subcells were also fabricated at *Spectrolab* achieving efficiency of 26.7% (first generation) [7]. Fig. 3 shows DJ and TJ cell structures of GaInP/GaAs/Ge developed at *Spectrolab*.

The active germanium subcell in the triple-junction GaInP/GaAs/Ge solar cells increase the voltage of cell, since it is in series with the top two subcells. Top two layers of GaInP and GaAs absorb photons in the solar spectrum with energy greater

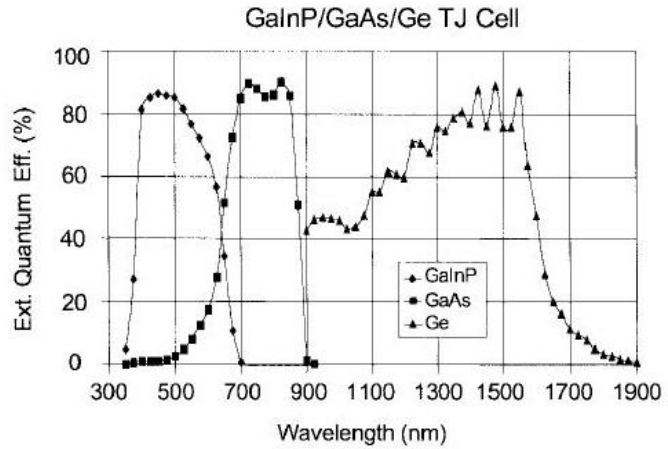


Fig. 4. External quantum efficiency for each component cell of GaInP/GaAs/Ge triple-junction [7].

than the 1.42 eV bandgap of GaAs, while a portion of the remaining spectrum gets absorbed by the 0.67-eV-bandgap Ge. Fig. 4 shows the external quantum efficiency (EQE) of each of the three subcells, in which absolute QE values for GaInP and GaAs are reported. The Ge cell QE is reported as a relative measurement since the Ge cell does not limit the current of multi-junction stack as effectively as the other two cells. The primary difference in

performance of a DJ and TJ cell arises from the increase in open circuit voltage ( $V_{oc}$ ), which is over 0.2 V higher for TJ cells due to Ge subcell contribution. The light  $I-V$  ( $LIV$ ) of TJ cell at 28 °C is shown in Fig. 5.

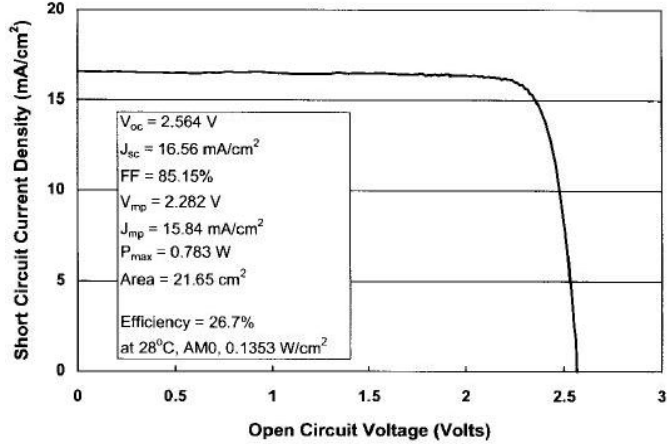


Fig. 5.  $LIV$  characteristics of GaIn/GaAs/Ge TJ cell with conversion of 26.7%, AM0 [7].

As can be seen in Fig. 1 and 6, the splitting of the spectrum in the GaInP/GaAs/Ge triple-junction cells is not ideal, where Ge bottom cell produces almost twice the current of remaining two cells. A more efficient photon energy conversion from solar spectrum using  $p-n$  junctions is possible with

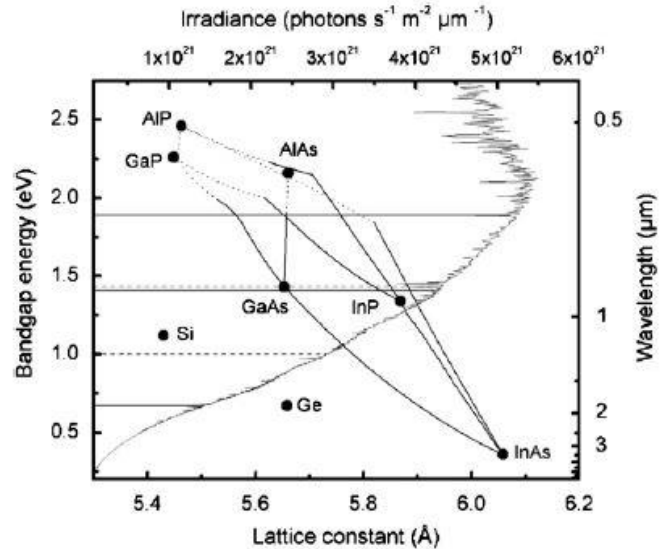


Fig. 6. Crystal growth chart with AM0 spectrum showing spectrum splitting with GaInP/GaInAs/Ge cell designated by solid horizontal lines [18].

the proper spectrum splitting (using the appropriate bandgap materials), and high quantum efficiency. Fig. 6 shows the spectrum utilization of TJ cells, where solid black lines designate the bandgap of each subcell. Through device optimization, current TJ technology is reaching its theoretical practical limit  $\sim 30\%$  efficiency under AM0 [15]. Device modeling done at *Emcore*, indicate that cell efficiency can be improved with further optimization of spectrum splitting [17, 18]. The model predicts the ideal set of TJ bandgaps for AM0 spectrum conversion to be 1.93 eV/ 1.37 eV/ 0.97 eV. The theoretical efficiency



of such an arrangement is ~39%. This set poses two problems, first III-V compounds required to achieve the optimum bandgap are not lattice matched to a commercially available substrate (refer to fig. 6), and second a 1.93 eV cell must contain Al. Lattice mismatch can be overcome with the use of metamorphic growth; however, this leads to higher dark current and shorter minority diffusion lengths. Using Al is problematic in the photoactive layer due to the presence of minority carrier traps.

### Inverted Metamorphic Multi-Junction Cells

A recent contender in addressing these challenges is the inverted metamorphic multi-junction (IMM) cells, which are identified as the best vehicle to-date to achieving increased solar efficiency [19-21]. Triple junction inverted metamorphic multi-junction (3J-IMM) cells proposed and demonstrated by Wanlass [22] reported a theoretical cell efficiency of 39.4%. Successful attempts have been reported in creating a thin, Ge-free III-V semiconductor triple-junction solar cell devices [19]. The cells are fabricated in an

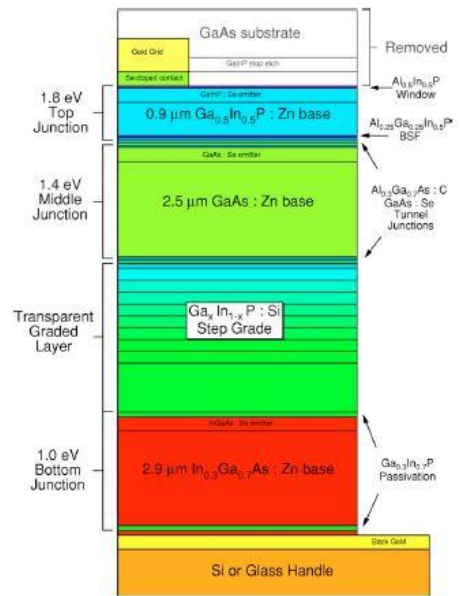


**Fig. 7.** Schematic of inverted triple-junction structure. The band gap energies decrease going up (red is the highest) [19].

inverted, monolithic triple-junction structure which achieved efficiencies of 33.8% and 30.6% under standard 1 sun global spectrum and space spectrum, respectively. The device consists of 1.85 eV  $\text{Ga}_{0.5}\text{In}_{0.5}\text{P}$ , 1.4 eV  $\text{GaAs}$ , and 1.0 eV  $\text{In}_{0.3}\text{Ga}_{0.7}\text{As}$   $p$ - $n$  junctions grown monolithically in an inverted configuration on  $\text{GaAs}$  substrate. The top  $\text{Ga}_{0.5}\text{In}_{0.5}\text{P}$  and

middle GaAs lattice-matched junctions were grown before any lattice-mismatched layers, preventing any threading dislocation that arise during mismatch growth from degrading their performance. Thus, the junctions that produce most of the power were grown with high crystal perfection for optimal solar cell performance. The three junctions are series connected with two tunnel junctions ( $\text{Al}_{0.3}\text{Ga}_{0.7}\text{As:C/GaAs}$ ). A schematic of the cell is show in Fig. 7.

*Emcore* has also successfully created inverted dual junction lattice matched cells with reported efficiencies of 26.4 % in conjunction with a 1eV filtered inverted-metamorphic cell with a 6% efficiency [20]. The individual component cells were combined into a 3J-IMM cells exhibiting efficiency of 32.0% under AM0. More recently, the focus of IMM performance advancement has shifted from 3J-IMM to 4J-IMM device architecture [21]. With material development through optimization of metamorphic grading layers (which can be a source of high levels

of material defects, specifically threading dislocations) along with improvements in optimization of the substrate removal process resulted in 4J-IMM cells with efficiencies of 34.5% (1-sun, AM0, 28°C) [23]. A schematic of 4J-IMM cells is presented in Fig. 8. With the removal of the epitaxial growth template, IMM cells present the potential for reducing costs by reusing the growth template and more importantly reducing the cell mass by the template removal during fabrication.

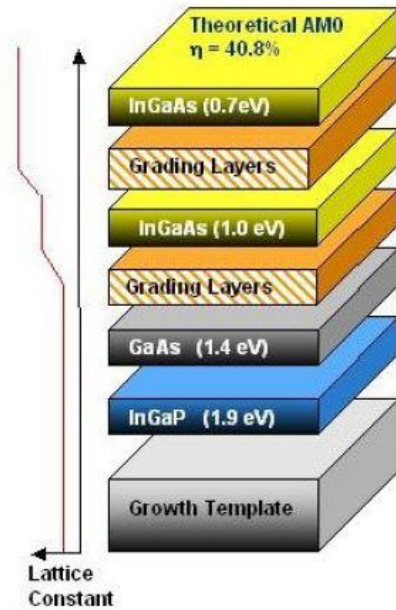
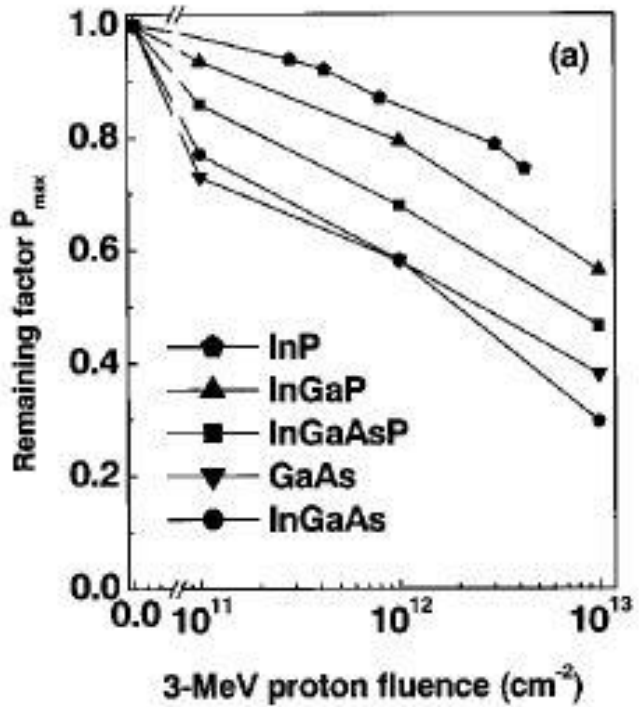


Fig. 8. Schematic of 4J-IMM cell [23].

## Radiation Resistance of III-V

When cells are exposed to radiation in space they are bombarded with wide spectra of protons and electrons. Both protons and high energy electrons excite electrons to higher energy states, potentially causing damage to the cell. Low wavelength charged particles transfer energy to the cell through ionization and other atomic displacement processes. Atomic displacement can cause blemishes



**Fig. 9.** Changes in the remaining factor of maximum output power as a function of 3 MeV photon fluence for InGaP, InGaAsP, and InGaAs solar cells in comparison with InP and GaAs cells [24].

and vacancies in the cell structure; such defects increases recombination rates which lowers the diffusion length. Dharmarasu *et al.* have shown that the radiation resistance of multi-junction cells increases with an increase in the fraction of In-P bonds in InGaP, InGaAsP, and InGaAs [24]. This increase in radiation resistance is attributed to the annealing of radiation-induced defects in the material with higher InP at lower temperatures, in which defects are annealed out at room temperatures. Hence, the high-radiation-resistant solar cells can greatly extend a space vehicle's lifetime in the space environment. Fig. 9 indicates the radiation resistance increase with increasing fraction of In-P bonds in InGaP, InGaAsP, and InGaAs. High efficiency 3J-IMM and 4J-IMM, fabricated at *Spectrolab* [25], reported a ratio of EOL to BOL efficiency ( $P/P_0$ ) of 84% and 80%, respectively, where

EOL efficiency is defined as the cell performance after exposure to 1-MeV electron radiation at  $1 \times 10^{15}$  e/cm<sup>2</sup> fluence. The radiation degradation factors presented in Ref. [25] indicate that IMM cell technology is approaching the tolerance levels of upright triple junction solar cells.

### **Effects of Microcracks on Solar Cells**

Microcracks develop in PV cells due to growth defects or due to external mechanical factors. These microcracks can lead to substantial power loss in both the terrestrial and space solar cells. On the terrestrial side, microcracks in Si wafers reduce mechanical stability [26] as well as the electrical quality of solar cells and modules [27]. Cracks in Si solar cells result in substantial power loss [28] in a standard PV modules with 60 cells. With prolonged operation cracks may expand, causing a power loss of up to 40% [29]. Cracks in a Si wafer critically degrade cell performance if they propagate from the Si bulk to the cell metallization which results in an electrical disconnection of the cell area [28], hence isolating cell parts from the busbar [30]. Substantial amount of research can be found in the literature that investigates the effects of microcracks on the Si solar cells, both at the cell and module level [26-34].

With their high efficiencies, good radiation resistance, and light weight, IMM cells demonstrate great potential for space application. However, IMM cells are potentially more prone to cracking than state-of-the-art TJ cells. In addition, advances in fabrication processes of TJ cells result in thinner Ge substrates (~80- $\mu$ m-thick). Due to the mechanical nature of thin films, however, these solar cells are more prone to fracturing during transportation, installation, and space operation, substantially adding to the installation cost

and potentially compromising the mission lifetime. Cracks generated in the semiconductor material have minimal effects on the performance of the cell, however, these cracks can propagate through the cell reaching the metal contacts

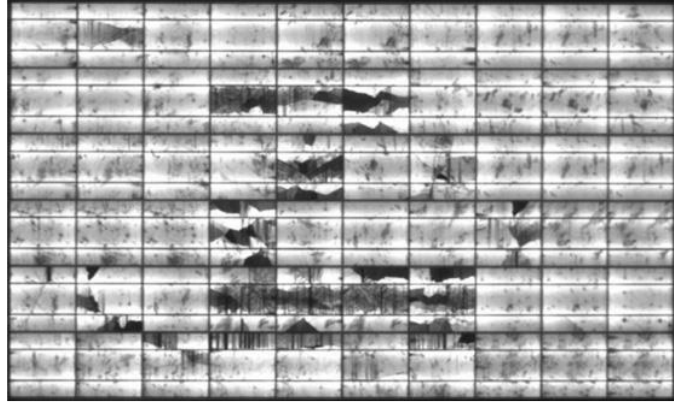


**Fig. 10.** Electroluminescence image of a micro-cracked PV module. Dark regions are electrically inactive areas [35].

resulting in electrically isolated areas. Kajari-Schröder *et al.* [35] have characterized microcracks in crystalline-silicon-based photovoltaic cells, using electroluminescence after artificial aging and snow damage (Fig. 10). These microcracks can electrically disconnect areas of the cells and lead to substantial power loss (~16%) [28].

Solar cells powering space vehicles must possess a long lifetime with strong durability despite fractures in the metal lines. Given the fragile nature of thin-film-solar cells and their high probability of cracking, it is likely that more solar cells must be replaced even before flight. This frequent replacement would significantly increase the costs of using thin-film-solar cells (e.g. IMM, TJ, etc.), therefore increasing the overall cost of flight mission. Pre-launch inspection are often costly and difficult to perform, in which individual cells and whole modules must be replaced, and often these micro-cracks may not be visible even with a thorough inspection. While these repairs are possible pre-launch and even in low-to-earth missions they are virtually impossible for deep space missions (e.g. NASA's MAVEN: Mars Atmosphere and Volatile Environment mission). Therefore, efforts to mitigate this power loss would have substantial impact on launch costs and the overall lifetime and success of the space mission.

To mitigate this power loss and increase the lifetime of IMM cells we propose the use of carbon nanotubes (CNTs) as mechanical enforcements to metal lines. Metal films embedded with CNTs, also known as metal matrix composites (MMC), possess reinforced mechanical strength against stress-induced fractures [36]. CNTs are promising nanostructure materials [37], which have been actively studied in recent years due to their unique mix of structural, electronic, thermal, and mechanical properties [38-41], making them suitable components in the MMC to reinforce the metal gridlines. The conductivity and high aspect ratio of CNTs are attractive characteristics for producing conductive composites using only minute amounts of CNTs. This feature can be used in coatings to get conductive and transparent networks [42-49]. In addition, individual CNTs can tolerate mechanical treatment, such as bending, buckling, or even certain degree of defect creation without loss of conductivity [50-52]. Possessing such a unique mixture of properties, CNTs demonstrate their potential in different scientific and technological areas, including transistors [53-56], diodes [57], sensors [58-60], and conductive pathways for electrochemical polymers coatings [61].

CNTs have the ability to toughen the matrix in which they are embedded in; i.e. the incorporation of CNTs will increase the ability to resist fracture within a material containing a crack. CNT toughening is exhibited in three mechanisms 1) crack deflection at fiber/matrix interface, 2) crack bridging, 3) fiber pullout on the fracture surface [62], as shown schematically in Fig. 11. In experimental work [63] CNTs were fabricated unidirectional within a ceramic matrix. After being subjected to lateral and transverse stresses using nanoindentation the CNTs exhibited all three toughening mechanisms (Fig. 11).

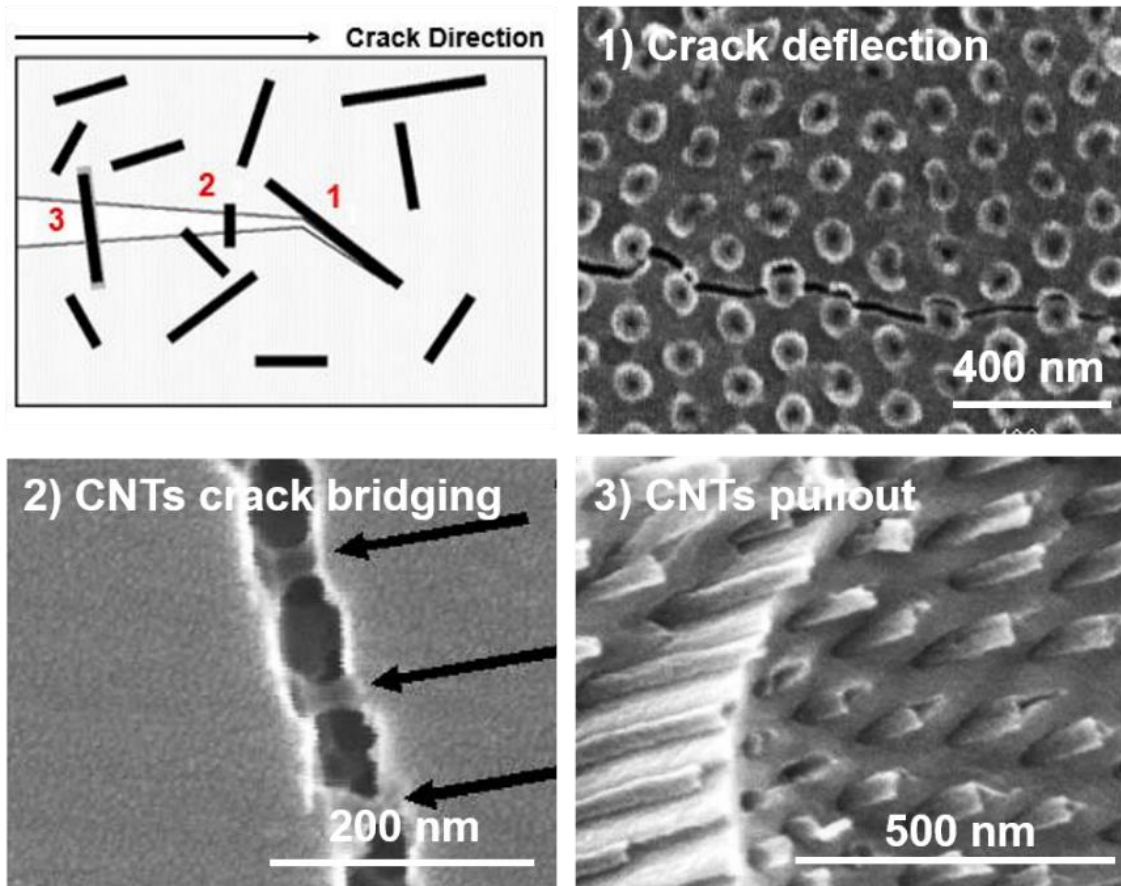


**Fig. 11.** Schematic diagram of CNTs toughening mechanism, Ref. [62]. (1) crack deflection around CNTs, (2) CNTs bridging a crack, (3) CNTs pullout. SEM Figures adapted from Ref. [63].

The addition of CNTs to different metal matrices affects the mechanical and electrical properties of the resulting composite. CNTs embedded within a silver (Ag) matrix via powder metallurgy showed an increase in the hardness and bend strength of the composite by 27% and 9%, respectively, upon addition of 8% by volume of CNTs [64]. However, the electrical resistivity increased significantly past the addition of 10% by volume of CNTs. In another study [65] multi-walled CNTs (MWCNTs) were mixed with copper (Cu) in electroless Cu deposition on CNTs. The electrical conductivity of the composite decreased with increased loading of CNTs, while the hardness, Young's modulus, and elastic modulus values increased.

In the work to be presented in the following chapters the details in creating the composites films will be discussed. The composite films are developed in a layer-by-layer microstructure composed of MWCNTs embedded within a silver metal matrix. Silver metal is deposited using electrochemical deposition (electroplating) using a cyanide-free electrolytic solution. The background and details of silver plating and the optimization of deposition will be discussed in chapter 2. Next, the various methods of deposition of CNTs will be discussed in chapter 3, presenting an overview of the different methods. In addition, details on the chemical functionalization of CNTs will be included in chapter 3. Finally, the development of the thin-film composites and gridlines will be discussed in chapter 4. The composite films are analyzed through a strain failure method to evaluate the impact of embedding the CNTs within the matrix on the overall electrical and mechanical properties of the film compared to bare Ag films. The integration process of composite lines on active PV cells will be discussed, in which standard gridlines (bare metal) are replaced with MMC gridlines. Composite-enhanced cells were intentionally cracked and the degradation in performance is compared to control cells with standard gridlines (Ag gridlines without CNTs).



## Chapter 2

### Cyanide-Free Silver Electroplating

#### Background

Metal electrochemical deposition, also known as plating remains till this day an art. There are countless industrial applications where various metals are plated onto different material in attempts to improve their physical and chemical properties. One such metal is silver which has been widely used for thin film coatings [66, 67]. Silver shows excellent physical, chemical and antibacterial properties [68-71], good corrosion resistance [72], high bulk conductivity and excellent features for decorative purposes. Thin homogenous layers of silver which can deposit onto less noble materials are of great importance for microelectronics, aerospace, and automotive industries [73-76]. Silver can be deposited through a variety of techniques including electro and electroless depositions, and vacuum deposition techniques (chemical/physical vapor deposition, ion sputtering), with the later techniques having several drawbacks, including difficulty controlling the product quality, slow deposition rates, and the use of expensive equipment. Electroplating remains the simplest and cheapest techniques to-date capable of producing homogenous, highly reflective, thin film silver deposits. Metal electroplating is a process that coats conductive or semi-conductive

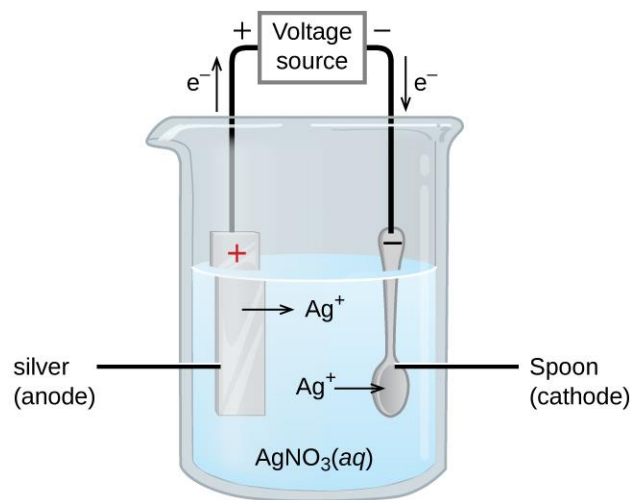


**Fig. 12.** Schematic of electrochemical cell, where anode is a pure silver electrode connected opposite from the working electrode (spoon). Both electrodes are immersed in a silver nitrate aqueous solution. As a steady current is passed through the solution, silver metal is removed from anode and deposited on cathode. [77]

objects with a thin metal film. The process uses an electrical current to reduce cations of a desired metal from a solution; this process is shown schematically in Fig. 12 [77]. Electroplating can be used to deposit various metals on targeted surfaces [78, 79]. The process is stable and suitable for growth of thin films and/or nanostructures with potentially enhanced thermoelectrical properties [80, 81].

Silver electroplating has been around for many years with the first patent issued in 1840 [82]. That bath is still one of the most used ones till this day in industry and it involves a double-cyanide silver complex  $[KAg(CN)_2]$ . Cyanide-based silver electroplating is widely used for industrial application as these processes produce smooth and compact deposits that are free of dendritic growth [83]. Numerous methods have been patented using electro/electroless silver plating [84-91], however, all such electroplating baths used industrially are extremely toxic due to their large cyanide content. In aqueous environments, cyanide is necessary in order to complex with  $Ag^+$  ions avoiding their spontaneous reduction. Besides the threat to the operator's health, the disposal of the exhausted plating bath and waste water treatment are becoming more and more expensive.

Due to the environmental concerns and the delicate manipulation required in the disposal of cyanides, few cyanide-free baths have been proposed [83, 92]. These cyanide-free silver electrolytes are based on nitrates, thiourea, and other compounds [78]. Such solutions, however, exhibit instability and the resulting deposits are of low quality in terms of adhesion and surface finish. Nitrate solutions, free of any organic or inorganic additives, often produce non-smooth, non-compact films regardless of plating conditions used. They consist of grains independently growing of each other and under given plating conditions may degenerate as dendrites [93-95]. More recently, other examples have been reported

in the literature with successful attempts of plating silver from nitrate solution upon using organic compounds such as tartaric and citric acid as growth inhibitors [96-99]. Smooth, coherent, and compact silver deposits were observed. Early experiments showed that, among organic compounds, hydroxyl acids, such as tartaric and citric acids, are most effective agents in the silver deposition [100, 101] and are widely used as additives in the electrodeposition of various other metals and alloys [102-115]. Using these organic additives, it was observed that the experimental weight of the deposits was significantly higher than theoretical weight required by Faraday's law. This behavior is attributed to the incorporation of organic additives into deposits [93, 96, 97]. In the case of using acetic acid ( $\text{H}_3\text{Ci}$ ) [99],  $\text{Ag}^+$  ions had a particular affinity to  $\text{HCi}^{2-}$  and it was suggested by the authors that this species ( $\text{HCi}^{2-}$ ) is the relevant parameter controlling the growth inhibition. Therefore, due to its electrical neutrality  $\text{Ag}_2\text{HCi}$  must be transported toward cathode by convection.

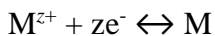
While the importance of charge transport in the plating solution is recognized, maintaining or adjusting the solution composition to consistently produce the film of sufficient quality and finish has been challenging in manufacturing. In this effort, we have primarily focused on silver (Ag) plating on gallium arsenide (GaAs) and indium phosphide (InP) substrates. The electrodeposition of Ag is first optimized using a commercially available plating solution. We use E-Brite 50/50 RTP from *Electrochemical Products, Inc.* [116, 117]. This commercial solution is cyanide-free, whereas traditional Ag plating solutions are cyanide-based typically with a trace amount of sulfur-based brightener (e.g., sodium thiosulfate). While the cyanide-based solutions may provide a superior metal

finish, we chose the cyanide-free commercial solution to avoid the toxic properties of cyanide.

Traditionally, cyanide Ag deposition is a two-step process requiring double bath. The first step is a cleaning/etching step in which a silver strike is added [78]. The explanation of this step is that most base metals are less noble than silver, therefore, such metals will precipitate upon immersion, causing silver deposits to poorly adhere. Consequently, silver-strike baths are used composed of low silver metal and high cyanide concentrations. This way the tendency for electrochemical displacement by the base metal is greatly lowered. Afterwards, sample is placed in plating bath with higher silver concentration and plating is carried out. Using 50/50 E-brite solution one bath is required without the use of a strike bath, given that the surface is a cathodically clean surfaces. One drawback of using such product is the challenge to plate over nickel surfaces, which in fact requires the striking step.

### **The Electrolyte Double-Layer**

When the metal electrode is brought into contact with a solution containing corresponding metal ions  $M^{z+}$ , then the following reaction



can take place at the surface, with either the forward or backward reaction being favored. As the forward reaction gets favored the electrons are stripped off from the electrode leaving a positive charge. This positive charge resides on the surface of the metal, since the high conductivity within the metal does not allow for the development of an internal space-charge region, and it will attract anions towards the neighborhood of the electrode

setting up a charged double layer [118]. As the surface charge builds up, a difference in potential arises between the interior of the metal and the solution phase near surface, where  $\phi_M \neq \phi_S$ . In the case of electrochemically active electrode, in addition to charging of the double layer, the passage of electrical current will produce an electrochemical reaction at the electrode.

If the electrolytic double layer is formed at an electrode, an excess of ions of charge opposite to that electrode will be formed. This can be

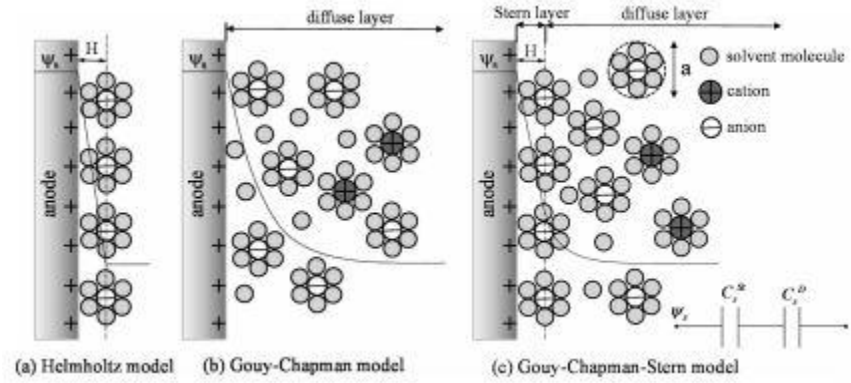


**Fig. 13.** Schematics of the electric double layer structure showing the arrangement of solvated anions and cations near the electrode/electrolyte interface in the Stern layer and the diffuse layer. (a) Helmholtz model, (b) Gouy-Chapman model, and (c) Gouy-Chapman-Stern model [119].

seen in Fig. 13a (Ref. [119]), where the ions approach the surface of the electrode as closely as possible resulting in a double layer that consists of two parallel layers of charge, one on the metal surface and the other on anions at a close proximity to the surface. This model is known as the compact double layer or the Helmholtz-layer model [120]. Using the Poisson equation, the potential can be calculated according to:

$$\frac{d^2\phi}{dx^2} = - \frac{\rho}{\epsilon_r \epsilon_0}$$

where  $\rho$  is the charge density and  $\epsilon_r$ ,  $\epsilon_0$  are the relative dielectric constant and dielectric constant in vacuum, respectively. Approximating the ions as point charges, we can assume that the charge density between the electrode surface and the Helmholtz plane is zero.

Hence, within the Helmholtz plane,

$$\frac{d^2\phi}{dx^2} = 0$$

double integration of the above expression yields

$$\phi = \phi_M - 2(\phi_M - \phi_S) x/a$$

where  $a$  is the diameter of the solvated ion.

One limitation of the Helmholtz model is that it does not consider the thermal motion of ions, which tends to loosen the ions from the compact layer. Gouy [121] and Chapman [122] proposed a model considering the effects of thermal motion of ions near the electrode surface (Fig. 13b), however, their model did not consider the possibility of an inner Helmholtz layer. Stern presented a model [123] that was a combination of the Helmholtz layer and the diffuse layer models (Fig. 13c). Due to the external field, tangential fluid flow develops along the charged surface. During this fluid motion a thin layer adheres to the surface, known as the hydrodynamically stagnant layer or Stern layer. An important point made by Stern, is that the position of the Helmholtz plane will vary with the type of ion attracted to the surface, where some ions may be able to lose their solvation sheath and approach the surface very closely, whereas others may approach the surface to a certain extent determined by their solvation sheaths [118]. This leads to the further subdivision of the Stern layer into the inner and outer Helmholtz layers. Specifically adsorbing ions exist in the inner Helmholtz layer, in which those ions possess a chemical affinity to the surface in addition to the Columbic interaction, while indifferent ions

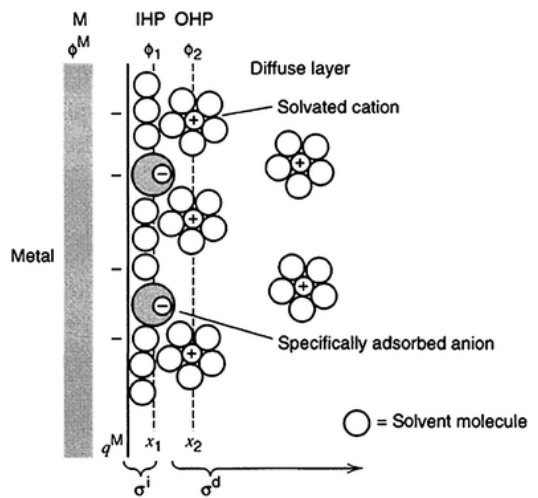


**Fig. 14.** Schematic view of the inner and outer Helmholtz layers showing specifically adsorbing ions and indifferent ions [124].

reside in the outer Helmholtz ion, which are attracted to the surface only through Columbic attractions (Fig. 14, Ref. [124]).

The Gouy-Chapman model can be quantified directly. If  $n_i^0$  is the number of ions  $i$  per unit volume in the bulk of the electrolyte at equilibrium, then

$$n_i = n_i^0 \exp\left[\frac{-z_i e_0 \phi(x)}{k_B T}\right]$$

where  $z_i$  is the charge number of species  $i$ ,  $k_B$  is Boltzmann's constant,  $e_0$  is the elementary charge, and  $T$  is temperature. Substituting the above expression in the following Poisson-Boltzmann's equation

$$\rho_e = e \sum_i z_i n_i$$

we can express the Poisson equation as follows

$$\nabla^2 \phi = \frac{-e}{\epsilon_r \epsilon_0} \sum_i z_i n_i^0 \exp\left[-\frac{z_i e \phi}{k_B T}\right]$$

at low potential  $\frac{z_i e \phi}{k_B T} \ll 1$ , Poisson equation can be written as  $\nabla^2 \phi = \kappa^2 \phi$ , in which  $\kappa$  is defined as the inverse of Debye length. The Debye length is a measure of a charge carrier's net electrostatic effect in solution and the extent to which those effects persist, and is defined as follows

$$\kappa = \left[\frac{e^2 \sum_i z_i^2 n_i^0}{\epsilon_r \epsilon_0 k_B T}\right]^{1/2}$$

From the above equation, it can be seen that the thickness of the double layer depends primarily on ionic strength of the solution. For higher ionic strengths, the diffuse double layer will become sufficiently small that it can be neglected and the entire potential drop is accommodated across the Helmholtz layer.

## Experimental Methods and Results

Many operating parameters (e.g., pH, ionic strength, temperature, and agitation) affect the outcome of plating. For E-Brite 50/50 RTP, the manufacturer's suggested *optimum* plating specifications are given in Table 1. While the tabulated parameters provide guidance, these parameters need to be further tuned for a specific plating bath. In our case, we vary the current density ( $J_c$ ) on the cathode as the main parameter, while keeping Ag metal ion concentration, pH, and bath temperature constant at 0.14 M, 9.2 and 20 °C room temperature, respectively. We use a magnetic stir bar to agitate the plating solution.

**Table 1**  
Manufacturer's suggested optimum plating parameters for E-Brite 50/50 RTP

<i>Category</i>	<i>Optimum</i>	<i>Range</i>
<i>Silver Metal Concentration(M)</i>	0.14	0.10 – 0.17
<i>pH</i>	9.2	9.0 – 9.6
<i>Temperature ( °C)</i>	20	16 – 24
<i>J<sub>c</sub> (mA/cm<sup>2</sup>)</i>	3.2 – 10.8	2.2 – 22.0
<i>J<sub>a</sub> (mA/cm<sup>2</sup>)</i>		2.2 – 10.8

Plating conditions are optimized in a series of experiments. The main variable is cathodic current density ( $J_c$ ), while Ag ion concentration, pH, and bath temperature are held constant. A custom made electroplating station is constructed in house, shown in Fig. 15, with fixtures to maintain a constant spacing between the electrodes for experiment repeatability. The electrochemical cell consists of: 99.997% pure Ag anode counter electrode, and Nickel (Ni) wire reference electrode. A Fluke Amp meter connected in



series with the working electrode is used to monitor the current/current density of the working electrode during deposition. A Fluke volt meter, connected in parallel with counter electrode and reference

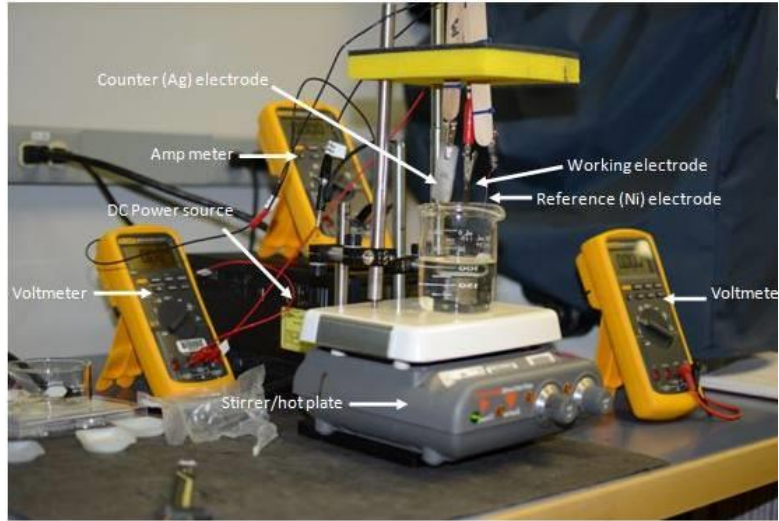
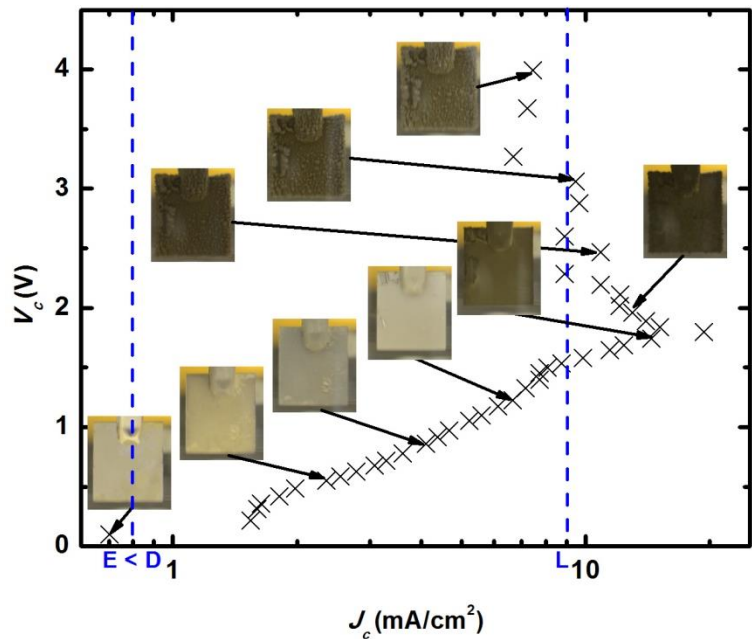


**Fig.15.** Electrochemical cell setup for Ag plating.

electrode is used to measure the reference voltage and monitor the solution resistivity. A *Corning* stirrer/hot plate and a Mono-Mold magnetic stir bar (length 1", diameter 3/8") are used to agitate the solution.

Fig. 16 [125, 126] shows the cathode potential ( $V_c$ ) vs. current density ( $J_c$ ) with corresponding images of Ag electroplated on GaAs substrates. Point E is below 0.6 mA/cm<sup>2</sup> in our case, where no current is flowing at the equilibrium potential.



Point D demarcates the decomposition potential

**Fig. 16.** Cathode potential ( $V_c$ ) vs. cathode current density ( $J_c$ ). The region between Point D and Point L defines the ideal operating window where the finish of plated Ag is bright [125, 126].

where the electrode reaction begins, and Ag starts to deposit. Point L defines the limiting

current density, above which Ag deposition is transport-limited,  $V_c$  becomes very unstable, and the plated Ag becomes “spongy”. The region between D and L define the ideal operating window where the plated Ag appears bright, which is associated with high-quality metal finish. The reader should note that the uppermost sample in Fig. 5, despite its location in the ideal window of operation, appears dark/ “spongy” where the control set point on current density is well above 10 mA/cm<sup>2</sup>, and the control over  $J_c$  becomes unstable.

A current density of 3mA/cm<sup>2</sup> consistently results in a bright finish; therefore, this current density is used in all subsequent Ag electrodepositions. In addition to precise control over the operating current density using a potentiostat

(*Princeton Applied Research*), we observe that

the initial seeding layer on the substrate significantly affects the final film quality. Various thin (~100 nm) seeding layers are explored, including sputter-coated Ti, sputter-coated Ag, and Ag deposited by physical vapor deposition (PVD). The PVD Ag seeding layer and subsequent electroplating of Ag result in a mirror finish (Fig. 17, insets [125]). That is,

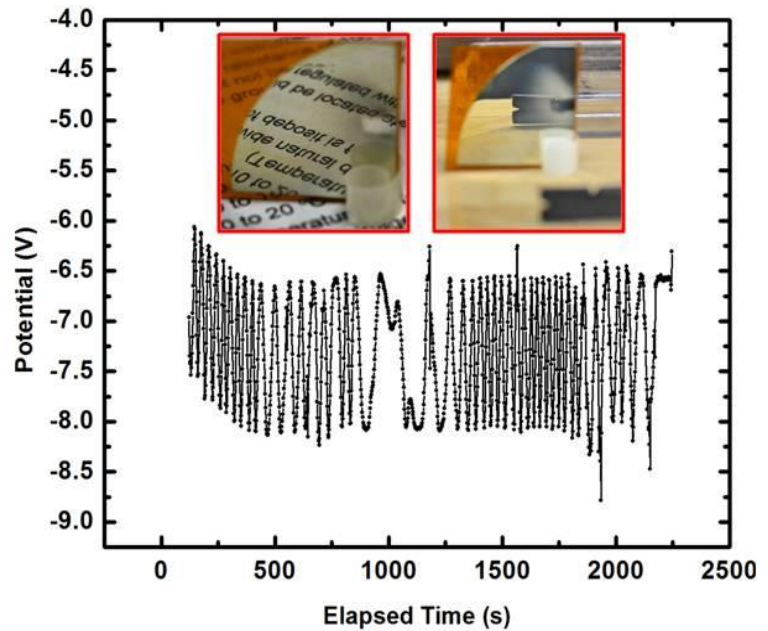


**Fig. 17.** Chronopotentiometry curve for Ag plating at 3mA/cm<sup>2</sup>. Image insets show the resulting samples with mirror finishes indicative of high quality Ag plating [125].

mirror finishes are obtained through the precise control of current density and the use of appropriate seeding layer.

Using the electroplating window (Fig. 16) we deposit silver film at different rates (current densities) and examine the resulting film quality under a scanning electron microscope (SEM). We are able to deposit smooth, coherent, and compact silver films at current densities ranging from 3 – 5 mA/cm<sup>2</sup>. Fig.

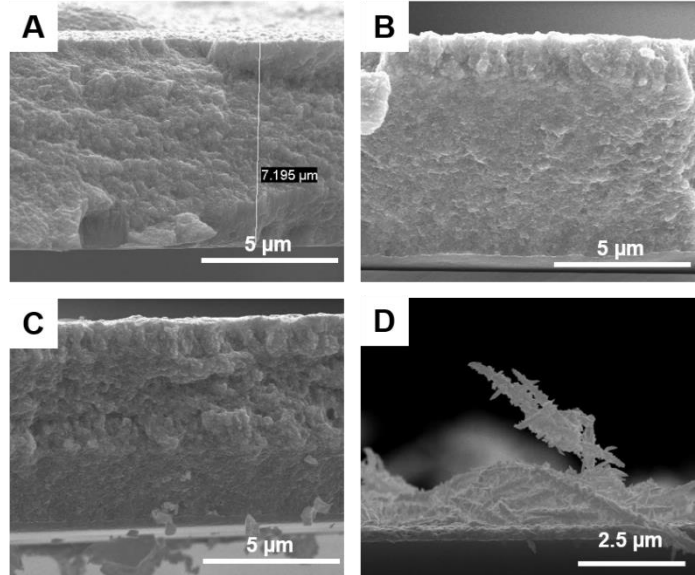


**Fig. 18.** Crosse-sectional SEM images of electroplated Ag at different growth rates. Smooth, coherent, and compact films are observed at current densities (A) 3, (B) 4, (C) 5 mA/cm<sup>2</sup>. Past 5 mA/cm<sup>2</sup> dendrite formation is induced (D, 6 mA/cm<sup>2</sup>). 18 shows the cross-sectional SEM

images at different rates of deposition, with thickness  $\sim 7 \mu\text{m}$ ; past 5 mA/cm<sup>2</sup> dendrites start to grow (Fig.18 D). The dendrites formed with a coarse surface morphology. The higher growth rate corresponds to faster reduction of Ag ions at the surface owing to higher charge density there. A similar behavior is reported in the literature [127-129]. In Ref. [127] silver nitrate solution was used to initially form dendrites under a strong direct current (DC) potential of 2 – 30 V. Following the growth of silver nanostructure, relaxation was carried out by removing the applied potential and maintaining the sample in electrolyte solution, resulting in the formation of nanowires. Yasnikov *et al.* [128] also reported the formation of various microstructures (pentagonal, regular shaped, planar, and dendritic) under various potentiostatic conditions. Dendrites were formed as the overpotential increased

from 160 to 200 mV. The formation of such dendrites occurred as a result of the severe depletion of the near-cathode solution with respect to silver ions, i.e. at the limiting flow of adatoms to be incorporated into the lattice, which was due to the high overpotential.

During electroplating from aqueous electrolytic solutions, electrolysis of water takes place [130-132] in which water decomposes into oxygen and hydrogen gas due to an electric current being passed through the medium [133]. Thus, hydrogen gets incorporated and trapped within the plated metal film. At higher applied potentials (higher current densities) we expect electrolysis rate to increase, consequently resulting in a higher rate of

incorporation of hydrogen.

To investigate this hypothesis, we deposit silver films (~7- $\mu\text{m}$ -thick) at various current densities.

Examining the cross-sectional of the as-deposited-films under SEM (Fig. 18 A, B, and C) the film appears to be smooth and coherent with no apparent voids forming due to hydrogen incorporation.

The samples are annealed in ambient air at 380°C for 5

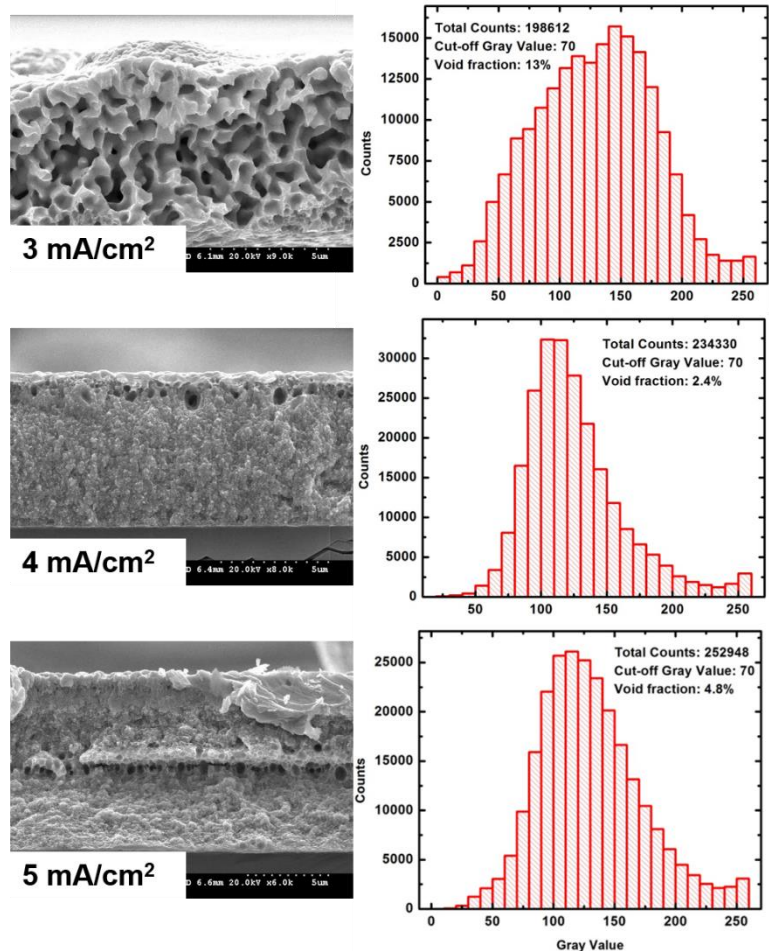


**Fig. 19.** Left: cross-sectional SEM images of electroplated silver at different deposition rates post annealing at 380°C for 5 min. Right: histogram plots of gray values vs. number of counts.

min to induce the formation of voids (Fig. 19). A short annealing time is used in order to promote the outgassing of hydrogen while trapping the voids within the film. We estimate the porosity of the films as a function of current densities through digitally analyzing the SEM images. Using ImageJ program, the SEM images are converted into a matrix of gray scale values with the corresponding  $xy$ -coordinates. The gray scale values are then plotted in a histogram (Fig. 19), and a cutoff gray value is assigned per image. This cutoff value represents the gray scale value of an open space; hence, all gray values less than this cutoff value are counted and divided by the total counts, giving the percentage void fraction. We note that this cutoff value is not a constant due to the variability in contrast and brightness settings from image to image. Contrary to our prediction, the highest porosity, after annealing, is associated with the lowest current density of deposition ( $3\text{mA}/\text{cm}^2$ ) where 13% void fraction is estimated, compared to 2.4% and 4.8 % at 4 and 5  $\text{mA}/\text{cm}^2$ , respectively.

The efficiency of the deposition process can be defined as the ratio of the current used for reduction of the ions for the intended deposit to the total current passed through the cell [134]. From a thermodynamical perspective it follows that only copper and more noble metals can be expected to deposit with 100% efficiency from a water-based electrolyte. For all other elements, part of the current will be consumed in the formation of hydrogen gas. It is desirable that this effect is minimized as much as possible, not only to increase the deposition efficiency and hence the deposition rate but also because the formed gas bubble can be difficult to remove from the sample surface and locally hinder further deposition. Most electroplating systems operate at an efficiency of 90% or higher although

it may be as low as 20%. The deposition rate in electroplating can be determined from Faraday's law

$$m = \alpha \frac{I t M}{n F}$$

where  $m$  being the mass of deposited material,  $\alpha$  the plating efficiency,  $I$  is the total current,  $t$  the time of deposition,  $n$  the charge of deposited ions, and  $F$  is Faraday's constant. For most metal depositions, the deposition rates are on the order of  $1 \mu\text{m}\cdot\text{min}^{-1}$ .

In this study, we demonstrate the ability to successfully plate coherent, compact, and continuous silver films from a cyanide-free silver nitrate aqueous solution. We identify the current density of deposition to be the key parameter in determining the film quality and its adhesion to the substrate. We also demonstrate the ability to obtain mirror finishes through using the appropriate seeding layer in conjunction with precise control over current density. We observe that under different current densities voids form within the film. We suspect this void formation, induced upon annealing, is attributed to hydrogen incorporation during electrolysis of water that is simultaneously occurring with silver plating.

### **Direct Electroplating on Small-Featured PV Gridlines**

Similar to other metal deposition techniques such as evaporation or sputtering, electroplating offers the ability to deposit a broad range of materials on various substrates (wafer, polymer, etc.) with or without the use of a seed layer directly on the semiconductor [135-137]. However, for microelectronics application, electrochemical deposition has some advantage over vacuum related techniques [134]. Electrochemical deposition can be carried out at room temperature, therefore reducing problems with thermal stresses, it does

not involve the use of expensive vacuum equipment, in addition, high rates of conformal deposition and high reliability depositions for high aspect ratios can be achieved using electroplating.

Through electrodeposition process it is possible to obtain properly filled features of only few tenths of micrometer across and aspect ratio of one or more. The electrodeposition process starts at the seed layer and through the use of special additives, the process can be adjusted to “super fill” the cavities [138], i.e. the growth at the bottom of the trenches and vias proceeds more rapidly than at the top or edges. Such controls are not possible in sputtering or evaporation where deposit start obstructing the feature making any further filing difficult, hence, resulting in voids within the interconnects. Through the application of

photoresist (PR) layer, only selected areas of the seed layer are exposed to plating solution. The thickness of the PR should be at least equal to the final thickness that has to be obtained for the conductors. The PR is then removed and the seed layer etched away. The process flow is shown schematically in Fig. 20.

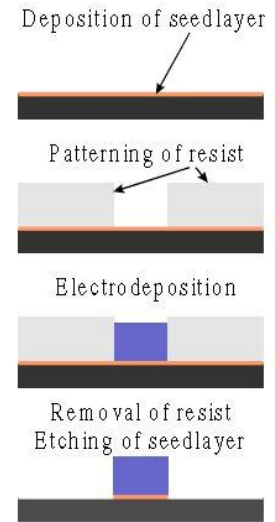


**Fig. 20.** Schematic of copper plating through a photoresist mask for interconnects [138].

### ***Initial optimization of Ag Deposition without use of Photoresist***

Electrodeposition of Ag is carried out on triple-junction (TJ) solar cells directly using the commercial plating solution E-brite 50/50 RTP. The plating is performed initially on TJ cells with fully metalized Ag gridlines, 5- $\mu\text{m}$ -thick and 22- $\mu\text{m}$ -wide. Fig. 21 shows a cross-sectional SEM views of gridlines prior to an electroplating of Ag. The gridlines

are deposited through electron-beam evaporation technique. These cells are used for initial tuning of silver deposition for the final integration on TJ cells with metal seed layer. Electrodeposition of Ag is tuned by varying the current densities of deposition while maintaining constant all other plating parameters. Four current densities are

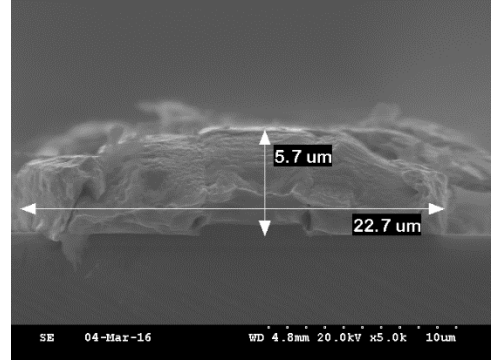


**Fig. 21.** Cross-sectional SEM image of Ag gridline of a TJ PV cell prior to electroplating of Ag.

explored  $-1.0$ ,  $-1.7$ ,  $-3.3$ , and  $-9 \text{ mA/cm}^2$ . The Ag gridlines are deposited for 20 min at the specified current densities and examined under SEM (Fig. 22). At the lower current densities ( $J_c < 9 \text{ mA/cm}^2$ ) the formation of silver flakes around the gridline edges is observed, however, at high current density ( $9 \text{ mA/cm}^2$ ) flakes are no longer present.

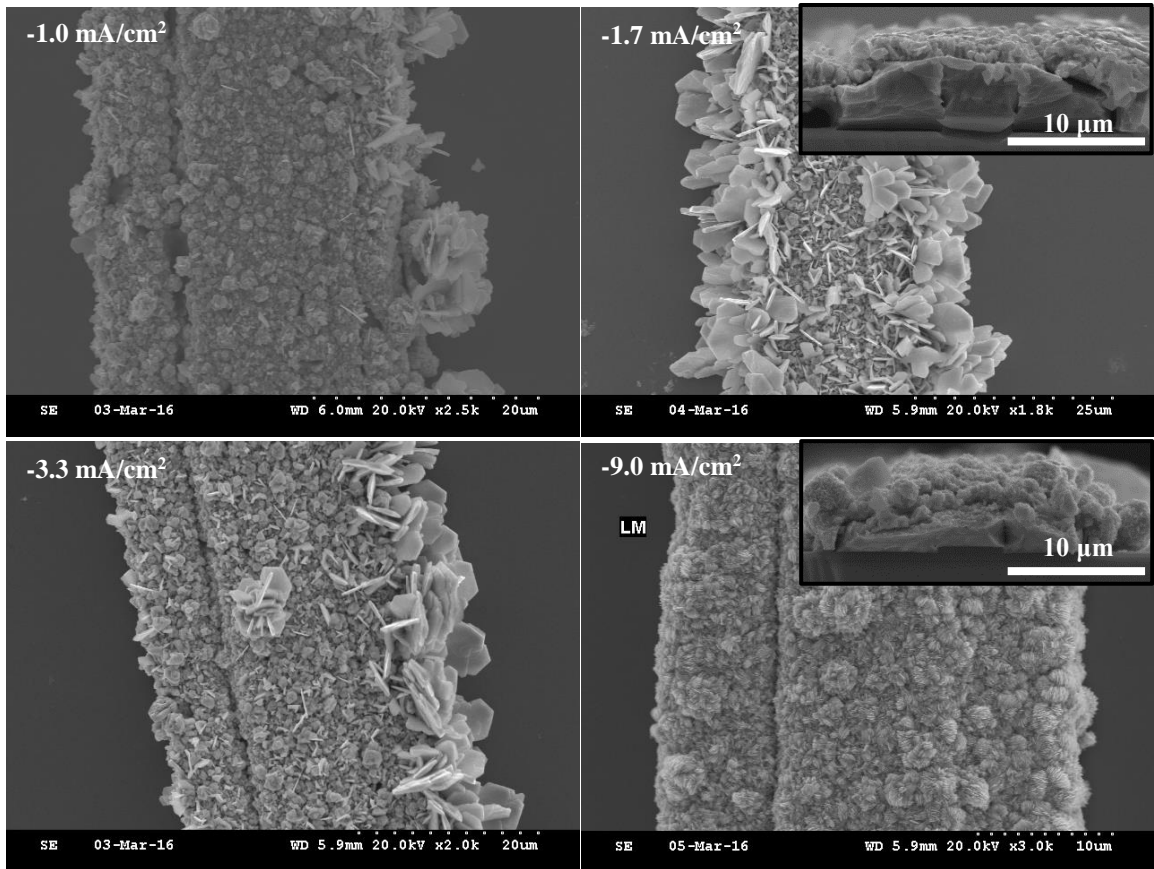


**Fig. 22.** SEM images of electroplated Ag on PV gridlines at different deposition rates.



Deposition at  $-9.0 \text{ mA/cm}^2$  shows a continuous layer of Ag growing more uniformly around the gridlines with significantly less flakiness (more compact layer).

The Ag deposition is repeated using two growth regimes, starting with a slow deposition rate ( $-1.0 \text{ mA/cm}^2$ ) for 300s followed by a high deposition rate at  $-9.0 \text{ mA/cm}^2$  for 500s (Fig. 23). The samples are examined under SEM (Fig. 24); results show a more compact layer of silver with a uniform thickness around the gridline. Initial deposition at the low current densities allows for the formation of Ag nucleation sites onto surface of the gridlines. The proper formation of these nucleation

sites allows for the successive formation of uniform Ag layers at the higher deposition rate, otherwise dendrites with coarse surface morphology start to form.

### ***Optimization of Ag Deposition on solar cells using Photoresist***

TJ solar cells with a Ag seed layer is electroplated with Ag using the two growth regime mentioned earlier. Two sets of  $2 \text{ cm} \times 2 \text{ cm}$  TJ cells with atypical metallization pattern are purchased from *Solaero Tech*. The first set has regular Ag-based front metallization and second included only a seed metal layer evaporated on the cells. The

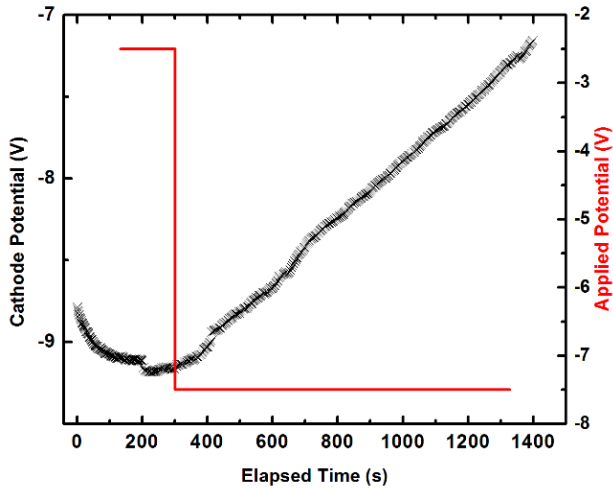


**Fig. 23.** Chronopotentiometry graph for Ag electrodeposition showing two growth regimes at  $-2.5 \text{ V}$  and  $-7.5 \text{ V}$ .

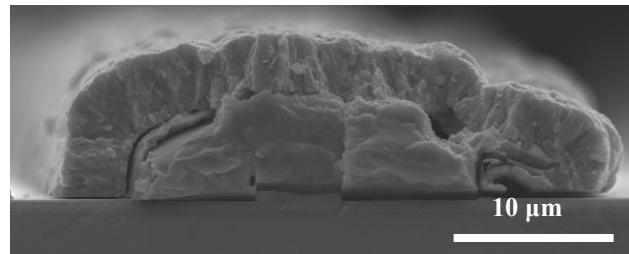


**Fig. 24.** SEM cross-sectional image of electroplated Ag on gridlines using two growth regimes.

gridline width on TJ cells was increased to 30  $\mu\text{m}$  and the front contact pad increased to 2800  $\mu\text{m}$  x 6000  $\mu\text{m}$ . Cells are fully fabricated with active semiconductor layers (GaInP<sub>2</sub>/(In)GaAs/Ge) and a back metal contact. The cells with the seed metal layer have an additional layer of PR spun on them, exposing only the metal gridlines for subsequent integration of our MMC lines on top. A custom made plexi glass holder is assembled in house in order to secure the fragile TJ cells during MMC integration. The holder consists of two complementary identical pieces, with open windows exposing the front and back side of the cell to allow contact with the Ag electrolytic solution. A schematic of the holder is shown in Fig. 25.

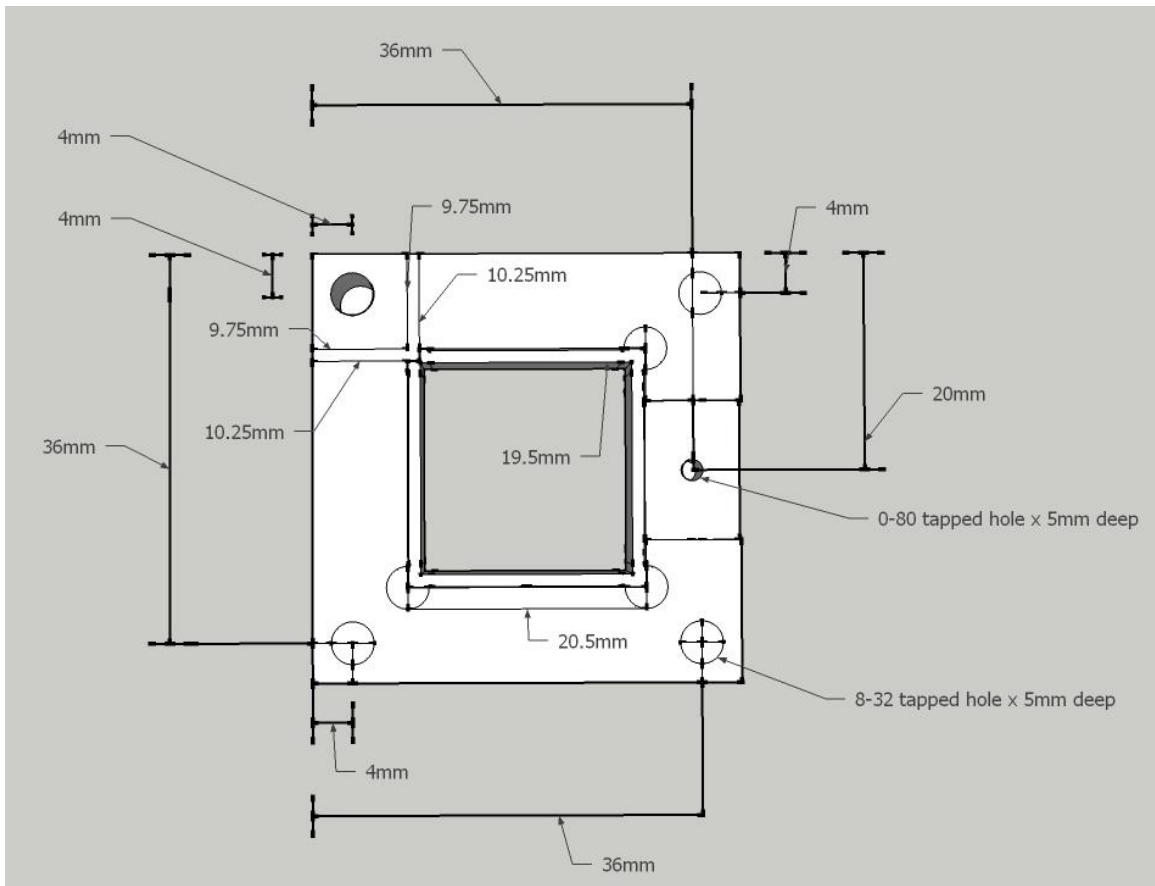


**Fig. 25.** Schematic of cell holder used to secure TJ cells during electroplating Ag. The holder design consists of a plexi glass with a hollow inside, allowing access for the electrolyte with exposed gridlines. The inside frame has a slight offset to accommodate the cell and secure it during deposition.

The first Ag deposition on TJ cells with seed layers is deposited using two growth regimes: at  $-1.0 \text{ mA/cm}^2$  for 200 s followed by  $-9.0 \text{ mA/cm}^2$  for 1200s. This Ag deposition is performed with the PR layer intact.

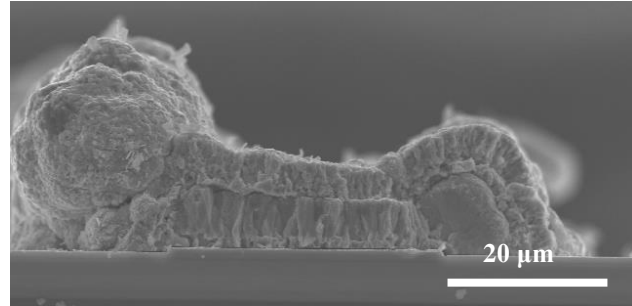


**Fig. 26.** SEM cross-sectional view of electroplated Ag gridlines, the initial layer is deposited using a two-growth regime, afterwards photoresist layer is stripped off and subsequent plating is carried out at  $-9.0 \text{ mA/cm}^2$ .

Afterwards, the PR is stripped off and subsequent Ag deposition is performed. The second layer of Ag is deposited at the high deposition rate ( $-9.0 \text{ mA/cm}^2$ ) for 800 s. Cross-sectional view of gridlines is shown in Fig. 26. The second deposition of Ag following the removal of the PR resulted in a non-uniform deposition of Ag, where a higher deposition is observed around the edges of the gridlines, resulting in the bulges seen in Fig. 26. This indicates that the removal of PR resulted in localizing the field at the edges of the gridlines and increasing the rate of Ag deposition there. In the absence of PR layer, the secondary layer of Ag grows around the gridline, resulting in an increase in its overall width (final width  $\sim 72 \mu\text{m}$ ). This in turn impacts the performance of PV cells as more of the semiconductor active area of the cell is obstructed by the gridlines increasing the shadowing losses of the cell and hence lowering its efficiency.

The Ag deposition is repeated on the cells where the PR layer is used through the entire Ag deposition process. The PR layer being intact during Ag deposition resulted in more vertical gridlines (Fig. 27). No bulging around the edges is observed and the gridline width is maintained at  $50 \mu\text{m}$  (the width defined by the PR layer) and a total thickness of  $\sim 10 \mu\text{m}$ . To obtain the proper thickness of gridlines ( $5 - 6\text{-}\mu\text{m}$ -thick) the deposition times

are adjusted as follows, nucleation step (-1.0 mA/cm<sup>2</sup>) increased to 400s, first electroplating step (-9.0 mA/cm<sup>2</sup>) decreased to 600s, and final electroplating step (-9.0 mA/cm<sup>2</sup>) adjusted to 400s. The modified recipe resulted in 5- $\mu$ m-thick gridlines (Fig. 28) which is a comparable gridline thickness to gridlines of commercial TJ

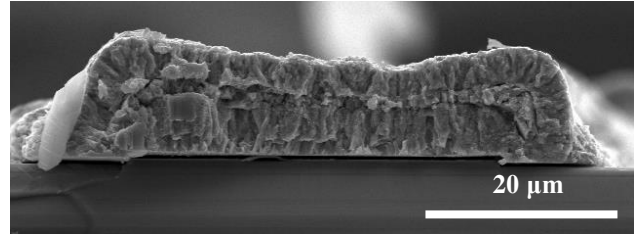


**Fig. 27.** SEM cross-sectional view of electroplated Ag gridline. Ag depositions are performed with the PR layer intact resulting in more vertical sides without any bulging.

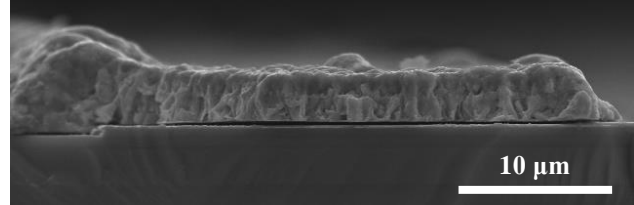


**Fig. 28.** SEM cross-section of Ag gridlines. Ag deposition times are adjusted to obtain thinner gridlines.

cells. It should be noted that the Ag deposition is not performed in a continuous deposition rather in a layer-by-layer (LBL) approach. The two distinct layers are seen in Fig. 26 – 28. Depositing Ag in a LBL method allows for the incorporation of CNTs within the metal to create the MMCs; this will be covered in more details in the chapters to follow.

## Conclusion

In this investigation, we demonstrate the ability to deposit homogenous compact layer of silver using a commercial plating solution. The deposition is optimized by adjusting plating parameters, primarily the deposition current density to obtain reflective thin films. The method is further investigated and optimized to deposit thin, compact, and homogenous layers of Ag directly on PV cells as gridlines. Although electrochemical deposition has been extensively studied there remains few problems to be addressed. For instance, the uniformity of depositions (i.e. the thickness) can be difficult to control as it is influenced by the electrolyte composition and the pattern of corrugation. In addition,

during the plating process the solution components get consumed and require replenishment to obtain reproducible results. However, electroplating remains one the simplest methods to deposit high quality metal at a relatively low cost, compared to other vacuum related techniques.

## Chapter 3

### Carbon Nanotubes Chemical Functionalization and Deposition

#### Introduction

Since the discovery of carbon nanotubes (CNT) by Iijima [37] in the early 1990s, CNTs have attracted much research interest throughout many different scientific and technological areas. A CNT consists of one or more graphene sheets rolled into long, thin, hollow cylinder. Typical lengths and internal diameter range from 1 to 100  $\mu\text{m}$  and from 1 to 25  $\mu\text{m}$ , respectively [37]. The unique combination of physical and chemical properties of CNTs, including high electrical conductivity, great chemical and mechanical stability, and large surface area [139, 140], has made them one of the most widely used engineered nanomaterials. Some of the current and proposed applications of CNTs include structural composites [141], microelectronic devices [142], and flat panel displays [143]. In addition CNTs have been investigated for catalytic membrane [144, 145], mechanical thin film applications [146], electrochemical energy conversion and storage devices such as fuel cells [147-149], batteries [150-152], and supercapacitors [153, 154], separation membranes [155], field emission devices [156], nanocomposites [125, 126, 157-159], gas storage materials [160], and chemical and biological sensors [161, 162].

Controlling the architecture of CNT thin films at the nanometer and micrometer-scale is critical to tailoring film properties and functionality. Various surface modifications of CNTs have been employed to disperse CNTs, including chemical functionalization using strong acids [163-165],  $\pi$ - $\pi$  stacking interactions between side wall and aromatic groups [166], and polymer wrapping of nanotubes [167]. Among the various surface functionalization techniques, oxidation is the most widely studied method [168].

Oxidation of CNTs has been used for purification purposes [169] and to open CNT ends for metal nanoparticle insertion [170]. The liquid-phase oxidation involves acidic etching with nitric acid and/or sulphuric acid. Compared to other oxidation methods (gas-phase oxidation), liquid-phase oxidation is mild and slow and can provide a high yield of oxidized CNTs [164]. For complete functionalization of CNTs the entire surface of CNTs need to be oxidized to achieve the desirable dispersions. The surface oxidation is achieved through using an acid reflux approach [149, 165] in which oxidative acids ( $\text{HNO}_3$ ,  $\text{H}_2\text{SO}_4$ ) are used with or without other oxidants. Even with prolonged treatment of CNTs, a non-uniform functionalization is achieved due to the impartial surface oxidation of CNTs [171]. Since CNTs have hydrophobic surfaces they tend to agglomerate in polar solvent. During acid refluxing, some CNTs inside these agglomerates may not be attacked by the oxidative agents and remain unmodified.

To achieve more uniform oxidation of CNTs sonication is used for the entire chemical treatment process to keep CNTs dispersed. In a study investigating the sonochemical effects on CNTs [168] it was found that the surface of CNTs became heterogeneous due to the attack of the oxidative acids with an increase in the surface roughness as function of treatment times. In addition, the settling speed (downward drift of CNTs in a burette), correlated with longer sonication time and hence higher functionalization, i.e. a higher settling speed is due to decreased interaction of the functional groups on the CNTs with the surrounding solvent. As the CNTs became more functionalized, the solvent-CNT interactions increased, leading to longer settling times.

## Experimental Methods and Results

### Chemical Functionalization

We make use of the sonochemical oxidation treatment to functionalize multi-walled CNTs (MWCNTs). Specialty MWCNTs (SMW200, purity 99% by TGA) purchased from *SWeNT* with the following specifications: outer diameter 10 nm, inner diameter 4.5 nm, length 3  $\mu\text{m}$ , bulk density 0.10  $\text{g}/\text{cm}^3$ . Two groups of

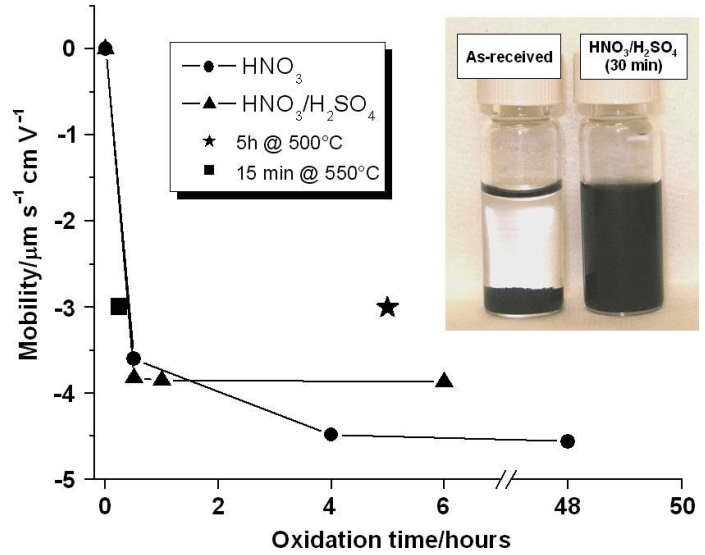


Fig. 29. Kinetic mobility of oxidized CNTs in water as a function of functionalization time, Ref. [173].

surface-functionalized CNTs are developed. The 1<sup>st</sup> group is functionalized with COOH for negative surface charge, following a standard acid reflux method [172]. The maximum electrokinetic mobility of CNTs is achieved through an acid treatment in a 1:3  $\text{HNO}_3:\text{H}_2\text{SO}_4$  mixture after sonochemical oxidation of two hours (Fig. 29) [173]. The 2<sup>nd</sup> group is functionalized with  $\text{NH}_2$  for positive surface charge by sonicating CNTs in 2.8 M  $\text{NH}_4\text{Cl}$  aqueous solution.

Carboxylation of CNTs involved refluxing CNTs in dry form in a 40 ml of 1:3 mixture of concentrated  $\text{HNO}_3:\text{H}_2\text{SO}_4$ . The mixture is sonicated for 3 h at 40°C. Mixture is then added drop-wise to 200 ml of DI water and left for few hours then vacuum filtered using 0.4  $\mu\text{m}$  pore filter paper (*Polypro filter paper, Millipore*). CNTs are thoroughly washed until all residual acid is removed and then re-suspended in DI water via sonication



for 30 mins, resulting in a neutral solution (pH 7). For the 2<sup>nd</sup> batch of CNTs we use carboxylated CNTs in dry form and further functionalize them by sonicating in 2.8 M NH<sub>4</sub>Cl solution, therefore targeting the surface hydroxyl groups for the successive attachment of amine groups. The CNTs are filtered and thoroughly washed, then resonicated in DI water.

Cyclic voltammetry tests are performed on the as-received, NH<sub>2</sub>-functionalized, and COOH-functionalized CNTs. Experiments are conducted using a three-electrode cell composed of Pt wire counter electrode, Ag/AgCl reference electrode, and a glassy carbon electrode as the working electrode. A phosphate buffer and

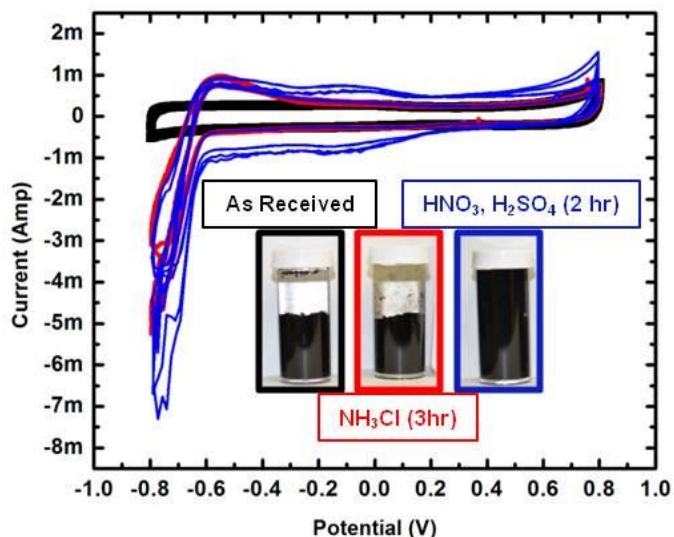


**Fig. 30.** Cyclic voltammetry measurements on the as received (black), amine-terminated (red), and carboxylated (blue) CNTs with corresponding images of the CNTs solutions, Ref. [125, 126].

KCl (0.1 M) solution is used as the electrolytic solution; a continuous N<sub>2</sub> flow purged the solution from any O<sub>2</sub> presence to eliminate any interference with the redox reactions. 2 mg each of non-of functionalized CNTs (control), carboxylated CNTs, and of amine-terminated CNTs, are individually prepared into solutions and drop casted on the glassy carbon electrode at room temperature. Cyclovoltammetry sweeps are performed with a vertex potential of 8V and a scan rate of 0.01 V/s for 3 cycles. We observe the highest overall integrated charge (Fig. 30, blue) associated with the carboxylated CNTs, which indicates that carboxylated CNTs assume the highest amount of surface charge and

presumably the highest electrokinetic mobility compared to neutral and amine-terminated CNTs. Carboxylation of CNTs produces stable, homogenous aqueous solutions of CNTs as seen in Fig. 30 (insets). The voltammograms show anodic peak at  $\sim 0.64$  V and cathodic peaks at  $\sim 0.58$  V for the treated CNTs that are associated with the oxidation and reduction of the surface oxide groups. The as received sample shows no evidence of oxidation and reduction of the surface oxides, indicating that the original CNTs had few surface oxide groups; the constant current in the potential region is attributed to the double layer charging. The capacitance of this double layer is estimated to be  $\sim 6.0$  F/g [168], comparable to that of graphitized carbon ( $\sim 5.6$  F/g) [174]. The height of redox peaks of the amine-terminated groups are reduced following the further functionalization in  $\text{NH}_4\text{Cl}$ , suggesting that some of the hydroxyl groups were indeed replaced with amine groups resulting in a reduced overall integrated charge. However, this functionalization method failed in producing stable suspensions of positively-terminated CNTs (Fig. 30 inset), indicating insufficient charge groups are produced.

To further investigate the amine termination method, we produce another batch of functionalized CNTs and examine the settling rate of the solution produced. We investigate the effects of sonication times and the variation of the recipes on the homogeneity of the aqueous solution of CNTs. We baseline our results relative to the

homogenous mixture of carboxylated CNTs. Firstly, CNTs are sonicated as received in 2.8 M  $\text{NH}_4\text{Cl}$  for three hours, without any prior treatment. Secondly, the as received CNTs

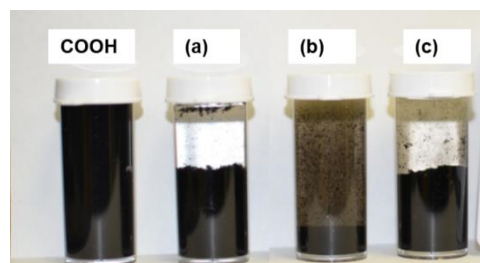


**Fig. 31.** Photographs of CNTs drifting downwards after 2 h of sonication (a) amine-functionalized for 3 h in  $\text{NH}_4\text{Cl}$ , (b) acid treatment followed by 3 h sonication in  $\text{NH}_4\text{Cl}$ , (c) acid treatment followed by 10 h sonication in  $\text{NH}_4\text{Cl}$ .

are first acid refluxed in 1:3 mixture of concentrated  $\text{HNO}_3:\text{H}_2\text{SO}_4$  for one hour, and further sonicated for an additional three hours and ten hours in  $\text{NH}_4\text{Cl}$  solution, respectively after thoroughly washing off any acids. The initial acid treatment is needed to introduce defect sites on the surface of CNTs for the successive attachment of amine groups. It has been shown that sonication in acid environment can fragment the CNTs [164, 170] and cause some mechanical damage to their surface. Therefore, we selected to use a low output power sonicator and a short acid sonication time to maintain the integrity of the CNTs. Photographs of CNTs settlings in containers were taken two hours after the final sonication in water, as shown in Fig. 31. None of the amine-terminated CNTs were successful in maintaining a homogenous dispersion (Fig. 3, a – c) regardless of the sonication treatment or recipe. On the other hand, the carboxylated CNTs maintained their dispersion in solution without crashing.

### **CNTs Deposition Methods**

Several methods exist today to obtain thin CNT networks, such as filtration [48, 175], spin coating [56], or Langmuir–Blodgett [176] method. In our work [125, 126] we have explored a variety of other CNT deposition techniques, including electrochemical deposition [61, 177], nanospreading [178], and drop casting. However, all the aforementioned methods were limited in either the speed of deposition or the surface uniformity or in some cases both. As an alternative, we make use of an air brush technique [49, 60, 159, 179-181] which is a simple and fast method that results in homogeneously continuous and thin layers of CNTs. For these different methods of deposition, we make use of the carboxylated MWCNT to create a layer-by-layer (LBL) Ag-MWCNT

composites. We optimize all the techniques and compare the surface uniformity and ease of deposition. In addition, we characterize the surface coverage of CNTs for certain deposition methods as a function of the different deposition parameters.

### *Electrodeposition of CNT-COO<sup>-</sup>*

For the microstructural comparison, COOH-terminated CNTs are used to create a LBL Ag composite microstructure. To make sure CNTs are negatively charged the factionalized CNTs are thoroughly washed and suspended in water through sonication without the use of any additives, resulting in a

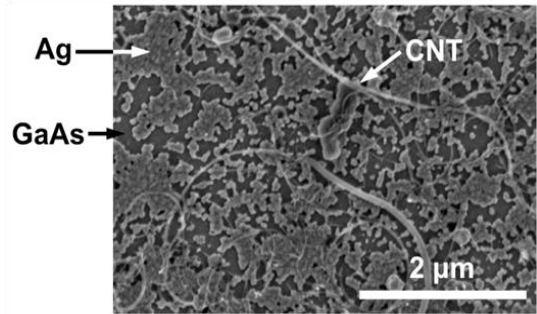


**Fig. 32.** SEM image of COOH-terminated CNTs deposited on 40-nm-thick, sputter-coated Ag to clearly show Ag dissolution during CNT deposition.

solution pH of 7. The isoelectric point (pKa) of carboxylic groups can range from 0.5 to 4.2 [182], hence, at pH = 7 carboxylated CNTs would be negatively charged as the water acts as a weak Lewis base stripping the proton from -COOH groups. Negatively charged CNTs are electroplated on GaAs sputter-coated with thin Ag layer (~40-nm-thick). Due to the negative surface charge on carboxylated CNTs, a positive bias must be applied to the working electrode (i.e., anode) to deposit CNTs. Consequently, the plated Ag dissolves back into the solution during CNT deposition exposing the underlying GaAs, this is shown in Fig. 32.

To determine the optimum condition for the electrodeposition of carboxylated CNTs current-voltage ( $I$ - $V$ ) characterization is performed. A standard analytical electrochemical cell kit (*Bio-Logic Science Instruments*) is used consisting of a platinum (Pt) counter electrode and a reference electrode (RE-2B calomel, outer diameter = 6 mm). A Fluke precision multimeter (8845A), connected in series with the working electrode, is used to monitor current/current density, and a standard Fluke digital multimeter is used to monitor the reference electrode voltage via a parallel connection between the counter and reference electrodes. Fig. 33 shows the response in current density (log scale) as a function of the applied voltage. It can be seen that the deposition is optimized around 1 – 3 mA/cm<sup>2</sup> (shaded vertical box, Fig. 33). Beyond 3 mA/cm<sup>2</sup> there appears to be a sharp increase in the current density vs. voltage applied. Therefore, this current

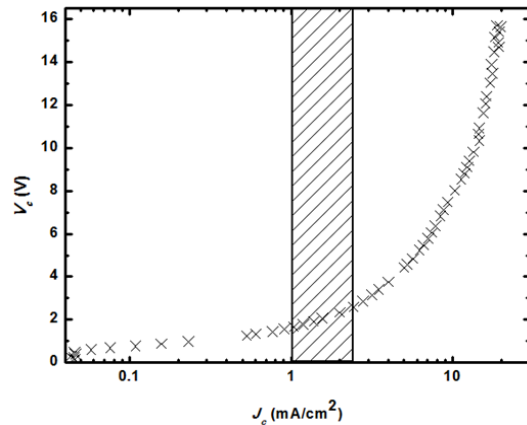


**Fig. 33.**  $I$ - $V$  characteristic curve. Shaded region indicates the optimum operating range above which  $V_c$  rapidly rises with increasing  $J_c$ . From Ref. [125].

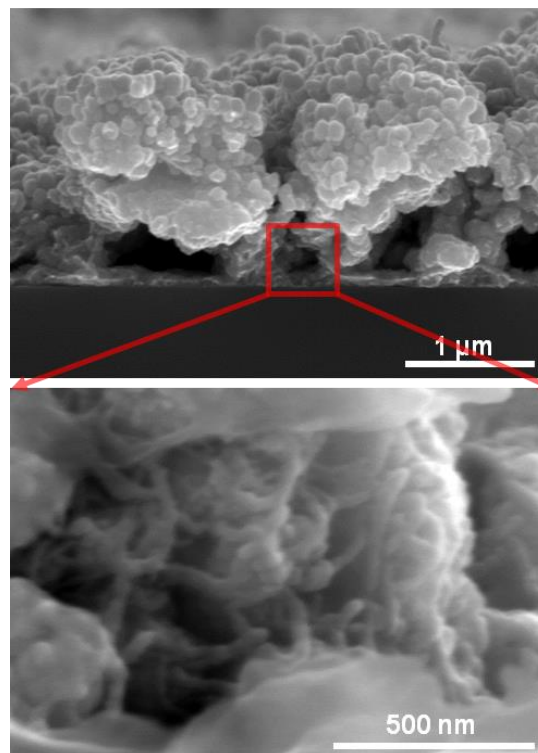


**Fig. 34.** Cross-sectional SEM image of MMC sample in a LBL deposition method though electrodepositing carboxylated CNTs on top of electroplated Ag. CNTs deposited at a slower rate than the Ag dissolution rate creating big voids within the composite. Bottom SEM image shows the existence of CNTs within the composite localized in specific locations within the structure.

density is chosen for the further electrodepositions of carboxylated CNTs.

We make use of the Ag electroplating in conjugation with electrodeposition of CNTs to create a LBL microstructure composite. First, a 2- $\mu\text{m}$ -thick Ag film is electroplated on GaAs followed by electrochemical deposition of CNT-COOH at 0.5  $\text{mA}/\text{cm}^2$  for 15 min. The sample is then electroplated with another 2- $\mu\text{m}$ -thick Ag layer. Fig. 34 shows the complete MMC structure after the final Ag layer is deposited. As seen in the cross-sectional SEM image we observe large voids within the composite due to the dissolving of large quantities of Ag during CNT-COO<sup>-</sup> deposition. This is to be expected given the opposite polarities of the depositing species as well as the difference in the electrokinetic mobility ( $v$ ) of deposited species ( $v_{\text{Ag}^+} \gg v_{\text{CNT-COO}^-}$ ).

### *Nanospreading Technique*

As an alternate method to electrochemical deposition, functionalized CNTs are deposited using a nanospreader technique. The nanospreader technique [178, 183] is used to deposit a thin layer of CNTs by dragging at a constant velocity the meniscus of microliter suspension droplets of CNTs trapped between the substrate and a moving Teflon blade. A droplet of CNTs

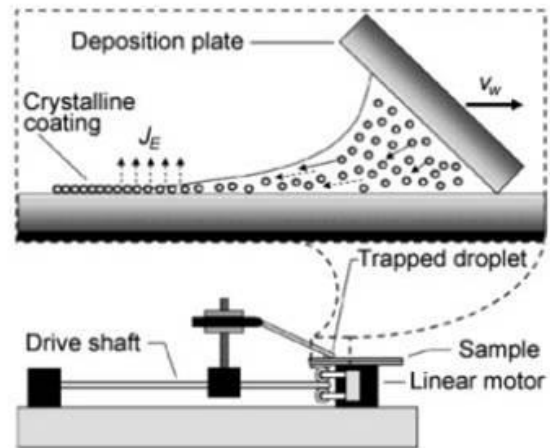


**Fig. 35.** Schematic of apparatus used in nanospreader technique. Figure adapted from Ref. [178].

liquid suspension is injected between two slides, a sample substrate and a deposition plate meeting at an angle of  $\sim\theta = 23^\circ$ . Capillarity holds the bulk of the droplet in the wedge

while the droplet meniscus stretches out behind as the linear motor pushes the deposition plate and drags the droplet across the substrate. A schematic of the apparatus used is shown in Fig. 35. The governing mechanism of this deposition method is convective assembly at high volumes fractions. The two major process parameters that allow control over the coating thickness and structure are the deposition speed and particle volume fraction. This technique offers precise control and reduced material consumption relative to standard dip coating methods [184, 185]. In addition, the integrity of the underlying surface (electroplated Ag) is unaffected as with the case of CNT electrodeposition.

The mechanism by which the dispersed particles are brought together and crystallized in the thin wetting films is convective assembly. The particles are transported to the edge of growing crystal by the flux of the liquid compensating for the evaporation from the crystal surface. The mass transport of this drying film region can be analyzed at steady state conditions in which the volumetric fluxes of the solvent and the accumulation of particles in the drying region are balanced. This relation has been proposed by Dimitrov and Nagayama [186]

$$v_c = \frac{\beta j_e l \varphi}{h(1 - \epsilon)(1 - \varphi)}$$

where  $\epsilon$  and  $h$  are the porosity and the height of the deposited colloidal crystals,  $\varphi$  is the volume fraction of the particle suspension, and  $\beta$  is the interaction parameter that relates the mean solvent velocity to the mean particle speed before entering the drying region ( $\beta \approx 1$  for small particle sizes). This equation has been applied to colloidal suspensions of particles similar to dip-coating method.

In a study investigating the deposition of latex crystals and gold nanoparticles [178] using nanospreader technique three controlling parameters (deposition speed, particle

concentration, and solvent evaporation flux) were investigated. It was found that the deposition speed ( $v_c$ ) is the most effective and easily varied parameter. In another study [183], the nanospreader technique was used to deposit ordered fibers of tobacco mosaic virus (TMV). TMV is a rod-shaped virus (300 nm in length and 18 nm in diameter). When the droplets of this TMV virus were allowed to evaporate on a surface they exhibited alignment of linear virus aggregates. As the meniscus receded, these aggregates were deposited as fibers and strands onto the substrate. Investigating the correlation between the substrate wettability and the meniscus withdrawal speed ( $v_c$ ) it was found that receding meniscus orients the virus aggregates in the solution and that the hydrophobic surface promotes further organization of the fibers.

In this effort, we investigate a range of deposition rates ( $v_c$ ) using the nanospreader technique with pull speeds ranging from 2 to 30  $\mu\text{m/s}$  and droplet volumes ranging from 10 to 50  $\mu\text{l}$ . Through the manipulation of pull speed, we are able to obtain CNT surface coverage ranging from 12% to 86% (Fig. 36). Here, we define the surface coverage as the

percentage of substrate surface covered by CNTs, ignoring any CNT overlap. The corresponding surface coverage is quantified through digital image processing of SEM images. Using ImageJ program, the SEM images are converted into a matrix of gray scale values with the corresponding  $xy$ -

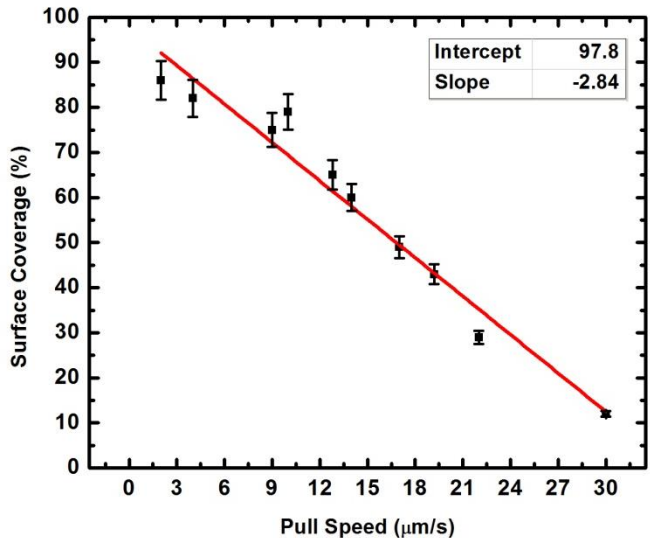


**Fig. 36.** Linear relation between the pull speed and corresponding surface coverage of CNTs using nanospreader method. Graph adapted from Ref. [125].



coordinates. The gray scale values are then plotted in a histogram, and a cutoff gray value is assigned per image. This cutoff value represents the gray scale value of an open space; hence, all gray values less than this cutoff value are counted and divided by the total counts, giving the percentage surface coverage. We note that this cutoff value is not a constant due to the variability in contrast and

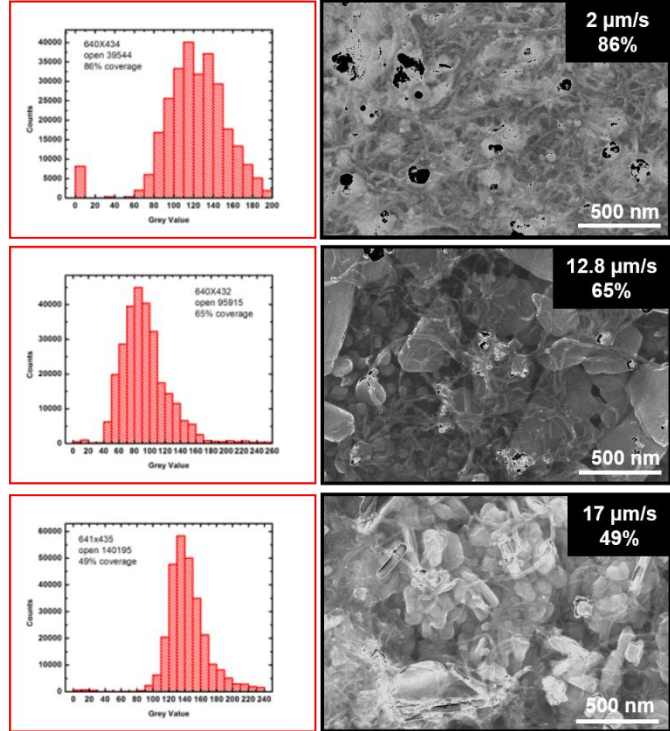


**Fig. 37.** Right: SEM micrographs of CNTs deposited on silver using nanospreader technique at various meniscus pull speeds ( $v_c$ ). Left: histogram of gray values of analyzed SEM images used to estimate the surface coverage of CNTs.

brightness settings from image to image. Fig. 37 presents SEM images at selected meniscus pull speeds (2, 12.8, and 17  $\mu\text{m/s}$ ) with the associated histogram plots. At higher pull speeds a lower surface coverage is achieved. The high withdrawal speed effectively spreads thin film onto the substrate producing higher shear force resulting in incomplete surface coverages.

Five layers of carboxylated CNTs are successively deposited at a blade pull speed of 10  $\mu\text{m/s}$  on an electroplated Ag layer. The sample is then plated with another 2- $\mu\text{m}$ -thick Ag layer, creating a MMC film with a total thickness of  $\sim 4\mu\text{m}$ . Fig. 38 shows the sample before the 2<sup>nd</sup> Ag layer is deposited (top SEM images) and a cross sectional view after the 2<sup>nd</sup> Ag layer is deposited (bottom SEM images). Top SEM view shows a well dispersed homogenous layer of CNTs deposited using the nanospreader technique. No

agglomeration of CNTs into bundles is seen indicating sufficient functionalization of CNTs. The cross-sectional SEM images show CNTs intercalating the Ag matrix. These images suggest that surface functionalized CNTs adhere well to Ag.

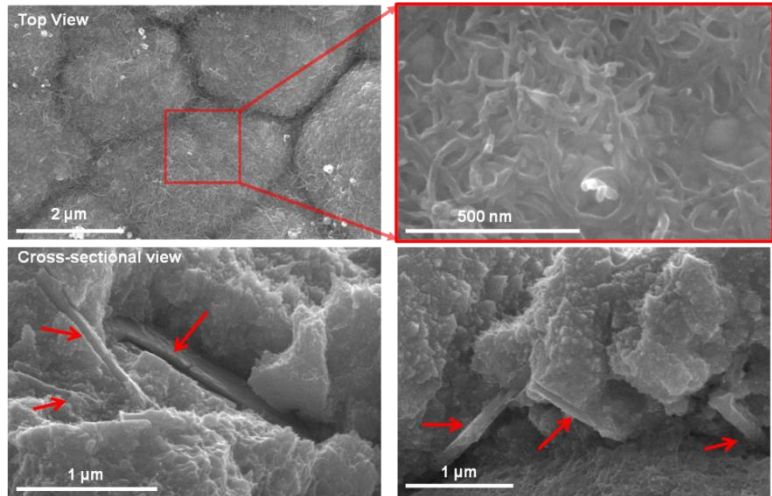


**Fig. 38.** Top: SEM images of COOH-terminated CNTs deposited on electroplated Ag, using the nanospreader technique. Five successive layers of CNTs are deposited at a blade pull speed of 10  $\mu\text{m/s}$ . Bottom: cross-sectional SEM images of Ag-CNT-Ag composite structure. The CNTs, indicated by red arrows, exhibit good adhesion to the surrounding Ag matrix. Fig. adapted from Ref. [125].

### *Drop Casting*

While the nanospreader technique offers precise control over the CNT surface coverage, the slow throughput limits its manufacturability. As an

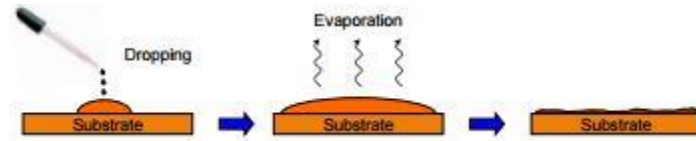


**Fig. 39.** Schematic of drop-casting method. A drop of solution is transferred onto substrate, following spontaneous evaporation of the solvent leaving behind the particles to be deposited; adapted from Ref [187].

alternative method of deposition, we have applied a simple drop casting method, using a solution of carboxylated CNTs. Drop casting method is a very simple, low-cost method with minimal to no waste of material. The process involves dropping solution onto a substrate allowing for spontaneous solvent evaporation, in which heating may be applied to the substrate to speed up the evaporation process and improve film uniformity [187]. This is shown schematically in Fig. 39. However, some associated drawbacks to this

technique is the difficulty in controlling the thickness, poor uniformity compared to other deposition methods, and the limitations to large area coverage.

An aqueous solution of carboxylated CNTs (1.3 g/L) is prepared via suspending CNTs in DI water using a sonic bath. A micropipette is used to transfer specific volumes of the CNT solution on electroplated Ag. The sample are then air dried at room temperature and the resulting surface coverage is digitally

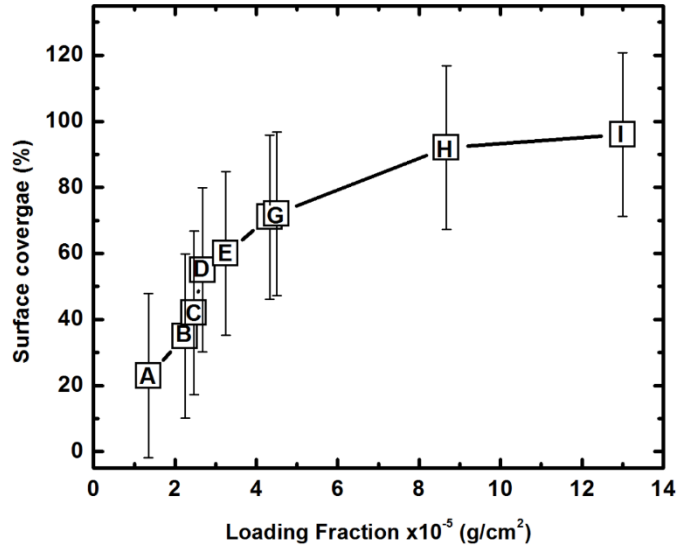
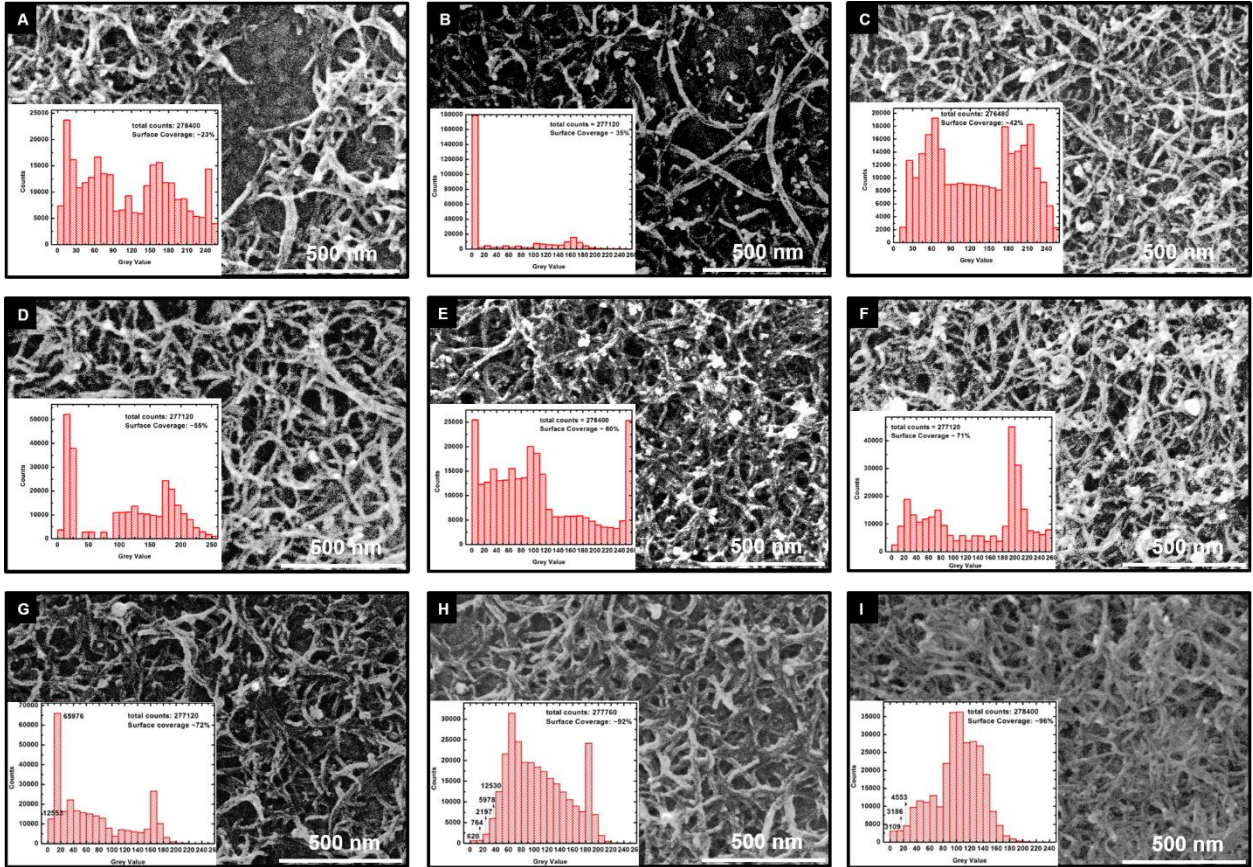


Fig. 40. CNTs loading fraction vs. surface coverage with standard deviation bars. Past point H ( $> 9 \text{ g/cm}^2$ ), the surface coverage plateaus, asymptotically approaching 100%. Fig. adapted from Ref. [125].

analyzed using ImageJ program mentioned earlier. We are able to obtain a range of different CNT loading fractions and correlate this to the surface coverage, as shown in Fig. 40. As to be expected the higher CNT loading results in higher surface coverage creating more dense networks of CNTs. Using this method, we observe that the surface coverage plateaus as the loading fraction is increased, asymptotically approaching complete (100%) coverage. Hence, using the graph in Fig. 40 we can control the surface coverage in such a way to allow for sufficient penetration of Ag through the CNT network to create more continuous composites. For example, examining the resulting SEM images at high loading fraction (Fig. 41, image I) we observe very dense networks of CNTs on surface with low porosity, this may be unfavorable for the proper intercalation of Ag within CNT network. On the other hand, at low loading fractions (Fig. 41, image A) there is a non-continuous

CNT network on the surface, which would result in weak reinforcement to the metal matrix.



**Fig. 41.** SEM micrographs of CNTs drop-casted on electroplated Ag at various loading fractions. Letters (A – I) correspond to the loading fraction and associated surface coverage from Fig. 12. Histograms show the gray value distribution after image analysis used to quantify the surface coverage.

### *Spray-Coating*

Although drop casting method is a quick alternative to nanospreader technique, it requires careful manipulation of the CNT aqueous suspension as well as a good temperature control to obtain homogenous CNT coverage. To readily control this deposition, we further develop the drop casting method through using a spray coating technique. Spray deposition is an integrated process which consists of three consecutive steps, namely (1) atomization of a liquid into droplets, (2) droplets travel on the atomization gas, and (3) the deposition

of the droplets into three-dimensional platform [188, 189]. This process is shown schematically in Fig. 42. This technique has gained wide acceptance as a cost-effective manufacturing process that is easily scalable. Of the three steps involved in spray deposition, atomization is the most critical step because it is linked to the mechanisms governing droplet generation.

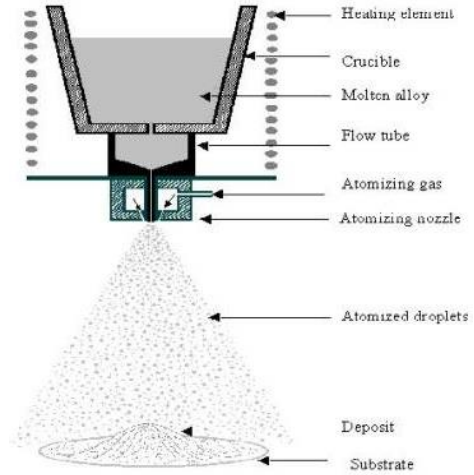


**Fig. 42.** Principle of spray atomization and deposition process, adapted from Ref. [189].

Atomization of liquid into droplets is achieved in three modes: twin fluid atomization, vacuum atomization, and centrifugal atomization. Twin fluid atomization [190] involves the use of a secondary liquid accelerated through a stream injector. The jets are focused onto a stream of liquid to be disintegrated, resulting in atomization. Vacuum atomization [191] involves the use of a liquid containing dissolved gases which is then injected into a low pressure (vacuum) environment. In the low pressure chamber the trapped gasses expand and are released into the low-pressure atmosphere causing deformation and disintegration of the liquid. Finally, in centrifugal atomization [192] the liquid is directly deposited onto a rotating disk at high speed. Under combined frictional

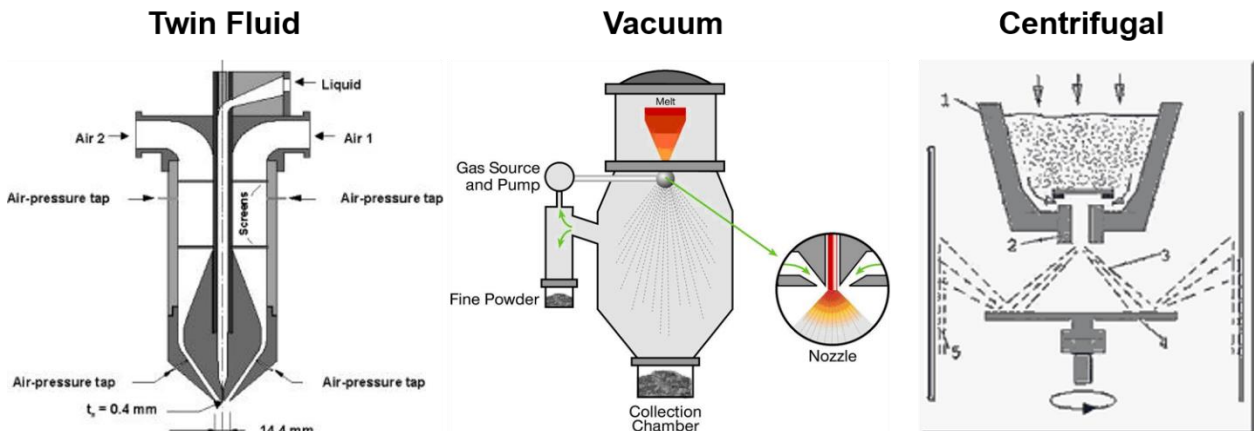


**Fig. 43.** Different modes of atomization: twin fluid, vacuum, and centrifugal, diagrams adapted from Refs. [190 – 192].

forces that develop at the liquid-rotor interface and the centrifugal forces, the liquid gets stretched into sheets that escape from the fringe of the rotor and become unstable resulting in breakup into droplets. The three modes of atomization are shown in Fig. 43.

Twin fluid atomization is further classified according to the atomization fluid used, i.e. water, oil, and gas (subsonic, supersonic and ultrasonic) atomization.

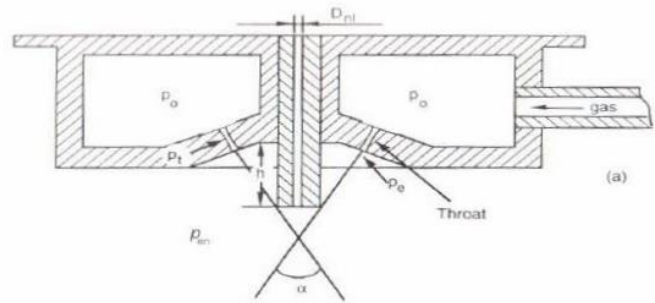


**Fig. 44.** Schematic of a twin fluid subsonic atomizer, Ref. [188].

Subsonic gas atomization is the

most frequently used, in which the produced droplets form a conical or linear spray allowing for most flexibility for a variety of processes. The gas nozzles in subsonic gas atomizers are designed to be inclined conically and focused in front of the orifice of the delivery tube at an apex angle ( $\alpha$ ), where  $\frac{1}{2}\alpha$  is known as the attack angle or impingement angle (Fig. 44). During atomization, high pressure gas is discharged from reservoir at pressure  $P_0$  into a chamber maintained at lower pressure ( $P_{en}$ ). Atomization gas expands and accelerates to high velocity. During this process the liquid disintegrates into fine droplets by the energetic impingement of high velocity fluid.

Atomizers can also be classified according to the relative position between gas jets and liquid streams into two categories: open type (free fall) and close-type (confined). In open type (free-fall) atomizer the liquid falls under gravitational force prior to interacting

with gas. While in close type atomizers the liquid travels a short distance, and is pre-filmed prior to gas interaction. The aspiration pressure (due to high velocity gas jets) causes the liquid to be

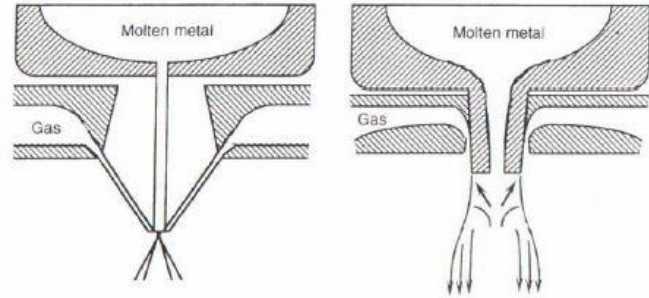


**Fig. 45.** Atomizer types (left) open type/free-fall atomizer, (right) closed/confined atomizer, Ref. [188].

stretched into thin films in low pressure region, creating the pre-filming effect under the action of aerodynamic forces. This type of atomizers has a higher efficiency compared to free-fall type. The two atomizer types are shown schematically in Fig. 45.

In addition, there are three types of gas orifices that play a role in the atomization process, and they include: converging orifice, converging-diverging orifice, and constant cross-sectional orifice. In converging nozzles, the cross-sectional diameter decreases gradually along the orifice and the velocity is confined to subsonic speeds; while in converging-diverging orifice, also known as the De Laval nozzle (Fig. 46), the diameter decrease initially reaching a minimum (nozzle throat) and then increases toward nozzle allowing for subsonic and supersonic gas velocities; and lastly the constant cross-sectional orifice consist of a constant diameter along the length of the nozzle. Atomization in the converging-diverging nozzle type (De Laval) involves gas jets that impinge tangentially at the delivery tube before merging at a focal point in front of the orifice. Due to the high velocity gas flow, a low-pressure

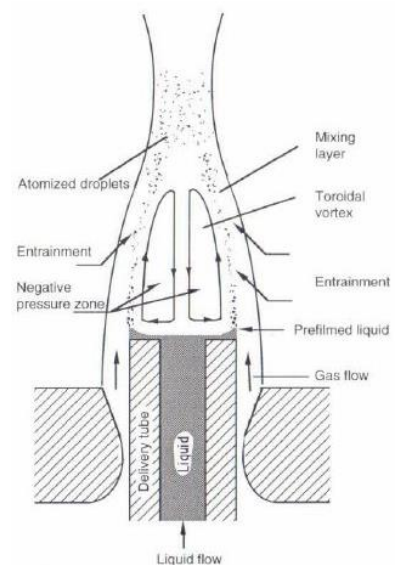
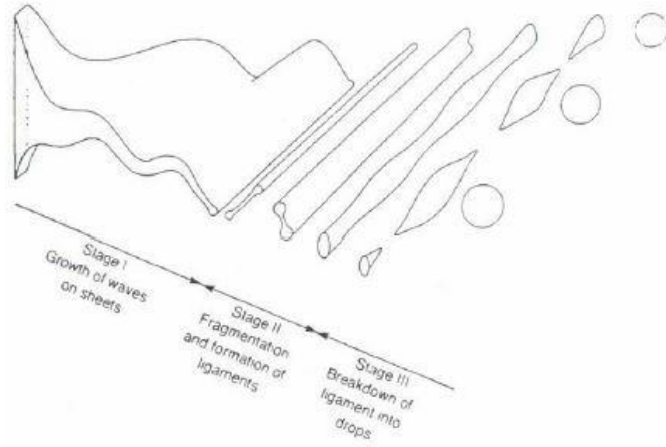


**Fig. 46.** Schematic of the De Laval (converging-diverging) nozzle, Ref. [188].

region develops where the liquid expands forming an envelope of mist, known as pre-filming. Liquid being atomized therefore is a film rather cylindrical jet.

Atomization relies on the mechanical disturbance imposed on the liquid. Two fundamental process must exist, first the formation of an initial disturbance wave in the liquid with an increasing amplitude, and secondly



the break-down of ligaments from disturbed liquid as wave amplitude reaches a certain critical value. Mechanism of atomization considers how the liquid becomes unstable under some initial disturbance. Dombrowski and Johns [193] considered the instability growth within a sheet of liquid moving at a relative velocity to the gas. They identified three major stages (Fig. 47): (I) the formation and growth of a disturbance wave in liquid, (II) disruption of liquid sheet into fragments, and (III) the formation of droplets by further fragment breakup. In stage I the first wave initiate on the liquid sheet due to disturbance from the ambient atmosphere. The variation of air pressure and shear forces generated by relative velocities at the gas-liquid interface causes the waves to grow in amplitude as a function of distance from nozzle exit. When most rapidly growing waves reach a critical amplitude (stage II) the sheet ripples and protuberances become unstable. Fragments are then broken/torn off at the crests and troughs. Finally, in stage III the fragments become unstable under aerodynamic and surface tension forces and further

**Fig. 47.** Three stages of droplet formation as proposed by Dombrowski and Johns.



breakdown into ligaments. The droplets form by spherodization of ligaments under the surface tension pressure.

For twin fluid atomization Klar and Fesko [194] suggested additional steps in the mechanism of the droplet formation resulting in a five stage mechanism as shown in Fig. 48. In stage I (wave formation), the waves form due to initial disturbances (due to flow separation at sharp corners and wall roughness) on the surface of the liquid. In stage II (wave fragments and ligament formation), the amplitude of growing wave reaches

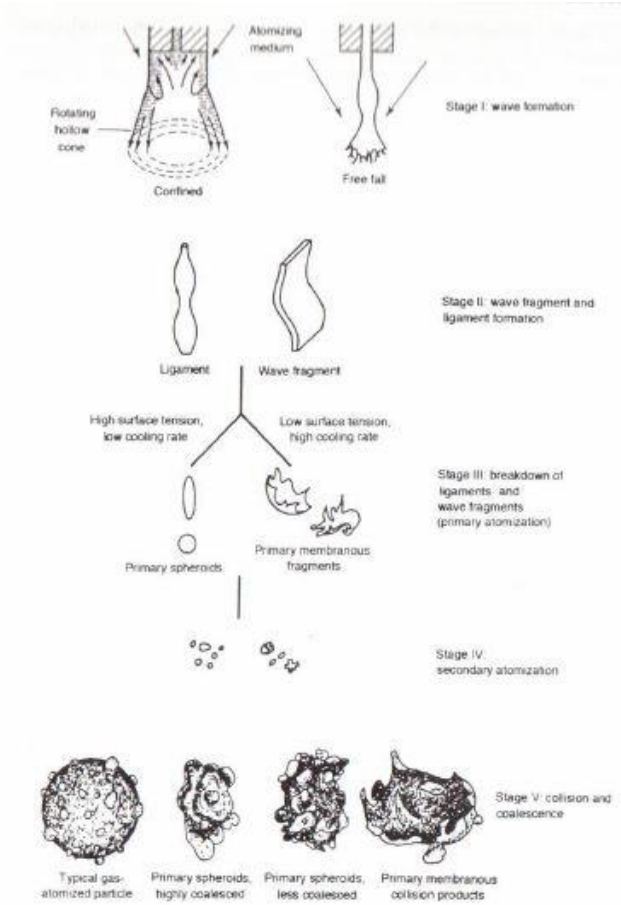


**Fig. 48.** Mechanism of droplet formation as proposed by Klar and Fesko, Fig. adapted from Ref [188].

a critical value where fragments with large aspect ratio are torn off

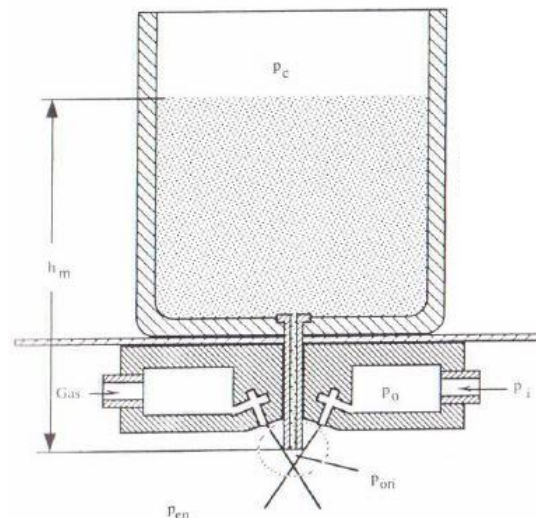
from liquid. Torn off ligaments become unstable and droplets are formed from subsequent breakup and spherodization of liquid ligaments (stage III, primary atomization). Following, a secondary atomization (stage IV) takes place in which droplets larger than a critical size will have aerodynamic forces acting upon them greater than restoring forces arising from the surface tension. These droplets experience further deformation, first becoming flat and then bowl shaped. Ones that are bowl-shaped in geometry burst into

droplets of smaller size. Finally, in the last stage collision occurs between droplets during flight leading to droplet coalescence.

There are two general categories that control the droplet size: (a) factors related to atomization conditions and atomizer types and these factor include atomization geometry, liquid stream dimensions, outer diameter of the crucible, diameter of delivery tube, protrusion length, and atomization gas pressure and velocity; (b) factors related to physical properties of liquid and atomization media including surface tension, viscosity, temperature of liquid, density of liquid, atomization gas properties (density, viscosity, sonic velocity, thermal characteristics). Among those parameters most important ones affecting the droplet size are the liquid flow rate, gas flow rate, gas velocity, and the liquid viscosity and temperature. Considering the liquid flow rate more closely there are three governing factors that affect the flow rate directly, and they are gravitational force (related to the liquid height  $h_m$  in the crucible), the crucible over pressure ( $P_c$ ), and the orifice pressure at the exit of delivery tube ( $P_{ori}$ ). The  $P_{ori}$  is generated due to the tangential fluid flow of high pressure atomization gas. In general  $P_{ori} <$

$P_{en}$  inside the atomization chamber, therefore, an aspiration effect is produced. The aspiration pressure is defined as the pressure field at the exit of the delivery tube and is related to orifice pressure and the environmental pressure as

$$P_a = P_{ori} - P_{en}$$



Assuming no new material is being added,  $h_m$  will decrease with time. Performing a simple material balance right at the exit nozzle where the decrease in the mass within the crucible equals mass flowing out of the tube, we get the following mass balance expression

$$A_c \dot{h}_m + A_n V_n = 0$$

where,  $A_c$  and  $A_n$  are the areas of the crucible and nozzle, respectively,  $V_n$  is the velocity of the liquid at exit, and  $\dot{h}_m$  is the rate change of the liquid height in crucible ( $h_m$ ) with respect to time. Taking the ratio of the area of the nozzle and area of crucible as  $\beta$ , where  $\beta = A_n/A_c$ , the above equation can be rearranged as follows

$$-\dot{h}_m = \frac{A_n V_n}{A_c} = \beta V_n$$

Performing conservation of momentum, using Bernoulli's equation, we obtain the following general relation

$$\frac{1}{2} \rho_1 V_1^2 + P_{ori} = \frac{1}{2} \rho_1 \dot{h}_m^2 + P_c + \rho_1 g h_m$$

Substituting for  $\dot{h}_m$  using the earlier expression and solving for  $V_1$  we get

$$V_1 = \sqrt{\frac{2(P_c - P_{ori} + \rho_1 g h_m)}{\rho_1(1 - \beta^2)}}$$

Calculating the mass flow rate ( $\dot{m} = \rho A_n V_1$ )

$$\dot{m} = A_n C_d \sqrt{\frac{2(P_c - P_{ori} + \rho_1 g h_m)}{\rho_1(1 - \beta^2)}}$$

Where  $C_d$  is the discharge coefficient and can be calculated according to the following equation

$$C_d = \left( \frac{1}{\alpha} + e_f \right)^{-1/2}$$

$\alpha$  and  $e_f$  are factors that depend on the Reynolds number at the exit of the delivery tube and the geometry of the nozzle.

Considering the effect of processing variables (liquid flow rate, atomization pressure, liquid, gas velocity, liquid viscosity) on droplet size the atomization pressure is considered the most critical parameter that affects size distribution of droplets. Generally, as the atomization pressure increases the droplet size decreases while other variables are held constant.

The pressure affects size

indirectly through changes in mass flow rate of liquid, gas flow rate, gas velocity...etc.

Fig. 49 shows the effect of pressure on the particle size, in which smaller droplets were obtained at higher pressures [195]. The smallest droplets obtained was through the combination of high pressure and high gas velocity ( $P = 2.46$  MP,  $V_g = 218$  m/s).

Conversely, examining the effect of liquid flow rate, Kim and Marshal [196] reported bigger size droplets at higher liquid flow rates (Fig. 50). In addition, they report finer droplet size as the velocity of gas increase, this is related to the relative velocity between gas and liquid that governs the breakup process. Other relevant parameters on droplet size is the liquid viscosity. In general, as the viscosity decreases the droplet size

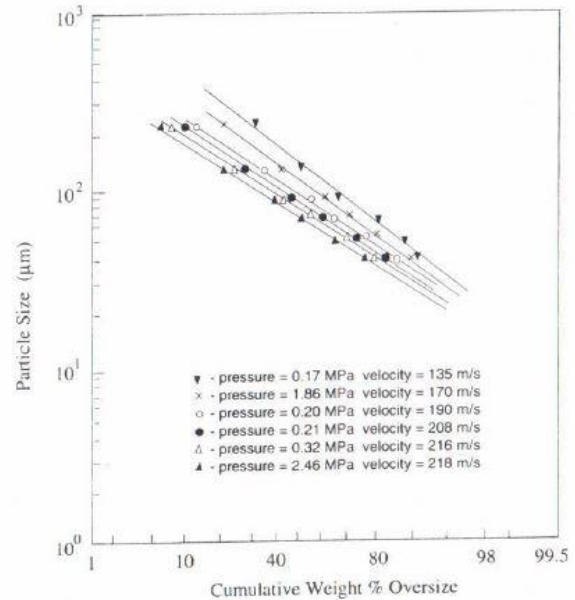


**Fig. 49.** Particle size distribution as a function of outlet pressure and gas velocity, Fig. adapted from Ref. [195].

decreases. A decrease in the liquid viscosity promotes a decrease in sheet thickness at the atomization edge which results in finer droplet development. The low liquid viscosity facilitates development and growth of instabilities in liquid sheet, leading to finer droplets

In our work, we make use of an air brush technique [49, 60, 159, 179-181, 197] which is a simple and quick method that

results in uniformly homogenous and thin layers of CNTs. Air brushes can be considered as an open-type, twin-fluid, subsonic gas atomizer, in which the liquid suspensions of CNTs are atomized using compressed air. Therefore, our focus will be directed to the subsonic gas atomization process. During atomization, high pressure air enters a chamber that is typically maintained at a low environmental pressure. The air accelerates to a high velocity as it expands in the low-pressure chamber. As a result, the liquid is deformed into fine droplets due to the impingent of the high velocity gas [188].

The liquid suspension (1.3 g/L CNTs<sub>(aq)</sub>) is directly spray coated with an air brush pistol (Badger, USA) onto the substrate, Fig. 51 shows a schematic of the gravity fed air brush. Spray deposition is performed with the aid of a heated movable stage to assist in the drying of the fine

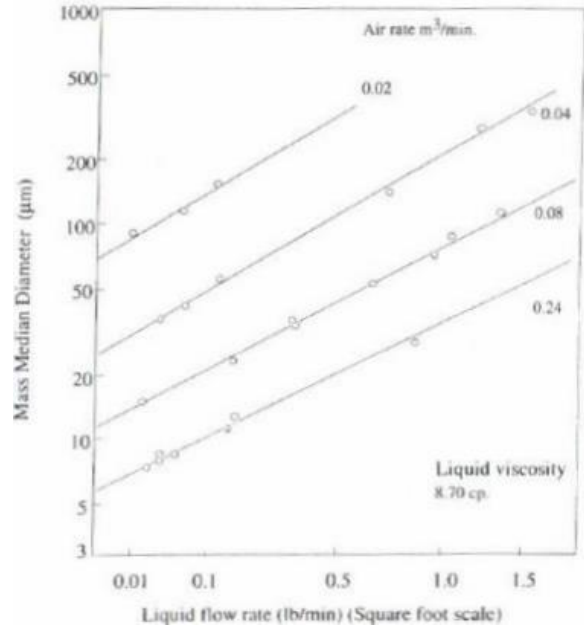


**Fig. 50.** Droplet diameter as a function of liquid flow rates at different air flow rates, Fig. adapted from Ref. [196].

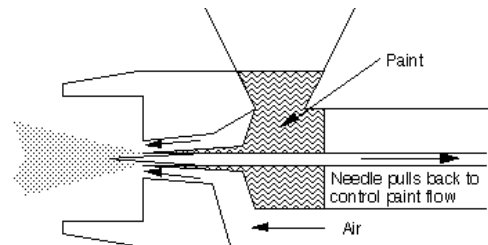


**Fig. 51.** A schematic of a gravity fed air brush. Air is injected around a tip which contains a sharp needle valve. As the air flows past the tip the pressure drops drawing liquid from the tip. The flow rate is regulated by the needle valve and the flow rate of air.

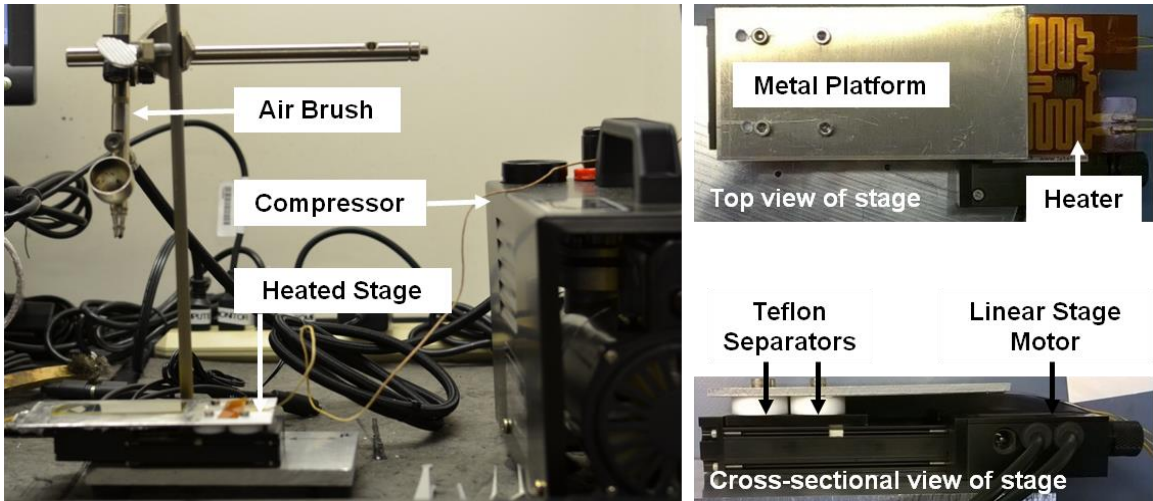


**Fig. 52.** Left: complete assembled apparatus for spray coating. Top right: top view of heated stage where sample is placed on the metal platform. Bottom right: cross-sectional view of stage showing the linear motor.

droplets on the surface. The stage temperature and speed are controlled up to 150°C and 3.6 mm/s respectively. Our deposition apparatus consisting of an air brush (Badger, gravity feed series, model 100G), an air compressor (Badger, TC910 Aspire Pro), and a custom built heated stage composed of a linear stage motor with a heater attached. Fig. 52 shows the assembled apparatus.

Our spray process involves a number of parameters such as stage-scan speed ( $s$ ), airbrush height ( $h$ ), flow rate ( $v_o$ ), nozzle outlet pressure ( $p_o$ ), and substrate temperature ( $T_s$ ) [188, 197-199]. Substrate temperature is critical for the drying dynamics of droplets, in which higher substrate temperatures allow for faster drying of the droplets and prevent coalescence into a larger droplet before drying [200]. In our case, our stage operating temperature is ~130°C. This temperature is high enough to allow for faster evaporation rates, yet low enough to be compatible with PV devices.

Nozzle outlet pressure and height are other critical parameters in the deposition process. High pressure results in a higher pressure drop across the nozzle resulting in high fluid velocity through the air brush nozzle. Consequently, liquid dispersion breaks into

smaller/finer ligaments and droplets [188, 198]. Although nozzle pressure affects the mass flow rate of CNTs, the nozzle height controls the mass of CNTs being deposited per unit area of substrate. In our depositions, we found a nozzle pressure and height of 20 psi and 10 cm respectively to be the optimum conditions allowing for fast droplet drying and uniform coats of CNTs. Under these conditions, we are able to spray continuous multiple layers of CNTs that are coalescence-free to the naked eye.

While substrate temperature, nozzle pressure and height, and flow rate all affect the spray deposition, the scan speed is the most critical parameter in our process. Under the operating conditions mentioned earlier, we can deposit CNTs at different surface coverages through altering the substrate scan speeds. The

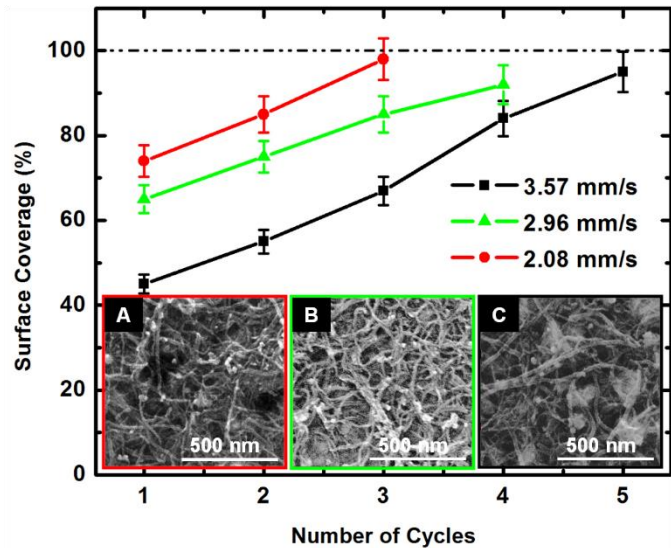


**Fig. 53.** CNTs surface coverage as a function of number of cycles of depositions at three scan speeds. Operating nozzle pressure and height are 20 psi and 10 cm respectively. Image insets A, B, C are SEM images after three cycles of depositions at 2.08, 2.96, and 3.57 mm/s scan speeds respectively; Ref. [159].

surface coverage is quantified through a digital image analysis (ImageJ processing) [125, 126]. Fig. 53 shows the percentage surface coverage of CNTs at three scan speeds with corresponding SEM images (Fig. 53 insets). Higher scan speeds result in shorter dwell times under the liquid flow. At a fast scan speed ( $s = 3.57$  mm/s), 95% CNT surface coverage is achieved after 5 cycles (Fig. 53), while slower scan speeds required a less number of cycles to achieve close-to-complete coverage.

Spray coating technique is a fast, cost-effective, and easily scalable method of depositing CNTs. In the work presented here we demonstrate the use of this deposition method in a single and multiple pass fashion for depositing multiple layers of CNTs. The film morphology and surface coverage can be controlled through several variables including air pressure, solution viscosity, solvent properties, air-brush geometry, distance between nozzle and stage, and stage scan speed. We identify the stage scan speed as the most critical parameter in our process that is easily controlled to obtain the desired surface coverages. Using a movable stage, we are able to perform single and multiple pass controllably while holding constant all the other spray deposition parameters. Hence, this allows for an adjustable layer thickness over a large area independent of the substrate morphology.

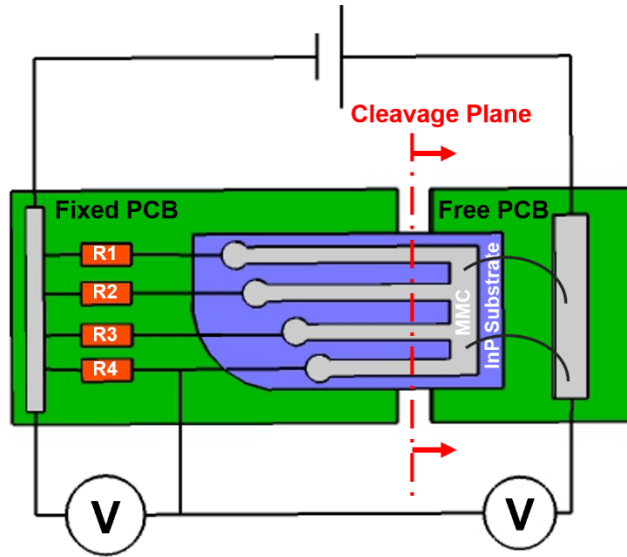


## Chapter 4

### Device Integration and Characterization

#### Electromechanical Characterization

To evaluate the ability of CNT to bridge microcracks in the semiconductor a strain failure test is developed at the Air Force Research Laboratory (Kirtland AFB, NM). Fig. 54 shows schematically the experimental platform for the strain failure test.



The test is designed to monitor the electrical performance of MMC grid fingers upon fracture through

**Fig. 54.** Strain failure (**RACK**) test for the electromechanical evaluation of MMC gridlines. The MMC gridlines are deposited on InP substrate and then attached on two PCBs, the entire setup is then mounted to a stage controlled by a linear stepper motor. Electrical resistance across each gridline is monitored as the gridlines are pulled apart through the stepper motor.

measuring the resistance across each line in the presence of cracks (**RACK** – **R**esistance **A**cross **C**leaves and **cracK**s). A set of four parallel MMC gridlines, deposited on an InP substrate, are first mounted on two printed circuit boards (PCB) using an adhesive. Upon curing the adhesive, the substrate is scribed with a diamond tip to generate a crack that propagates across the substrate backside, orthogonal in direction to the MMC gridlines. The cracked substrate is then attached to a linear stage controlled by a stepper motor (Fig. 55). The resistance across each of the MMC gridlines is continuously recorded as the gridlines are pulled apart at micron increments until the electrical resistivity approaches infinity upon plastic failure. Load resistors (R1 – R4, 200 $\Omega$ ) are each soldered to the

respective gridline, along with the leads at the end of each gridlines and the bus bar, completing the circuit. The setup is connected to 6V DC power supply and the resistance is continuously monitored through a data acquisition system. Optical microscope is used to confirm the gap distance created after every pull.

For the initial **RACK** measurements, we deposit a set of four MMC gridlines on InP. The MMC gridlines (1-mm wide, 5- $\mu\text{m}$ -thick) are deposited at different CNT loading fractions

through using the drop casting method mentioned previously, to create a layer-by-layer (LBL) microstructure. First, a 2- $\mu\text{m}$ -thick Ag film is electroplated on a 100-nm-thick PVD Ag seeding layer on an InP substrate. The solution of CNT-COOH is then drop-cast at room temperature. Another  $\sim 3\text{-}\mu\text{m}$ -thick Ag layer is finally electroplated on top. Cross-

sectional SEM view of this LBL arrangement is shown in Fig. 56, the loading fraction of this sample is  $\sim 5 \times 10^{-5} \text{ g}_{\text{CNT}}/\text{cm}^2$  corresponding to  $\sim 70\%$  CNT surface coverage. The CNTs are localized at  $\sim 2 \mu\text{m}$

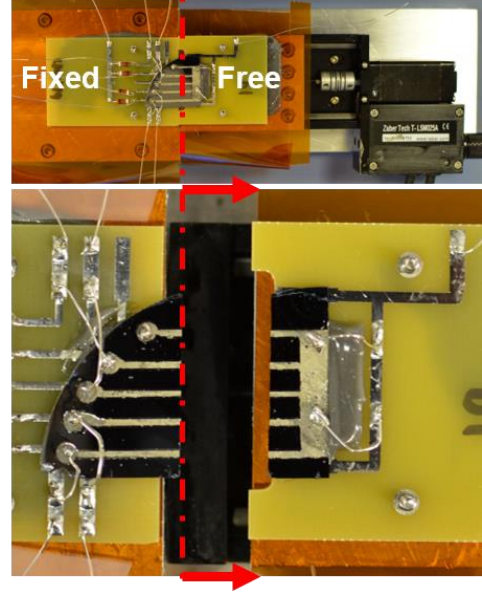


**Fig.55.** **RACK** test setup showing MMC gridlines on InP attached to PCB. The PCBs are mounted on a stage controlled by a linear stepper motor that pulls the MMC gridlines at micron increments. Dashed lines show the cleavage plane and arrows show the pull direction of the gridlines.

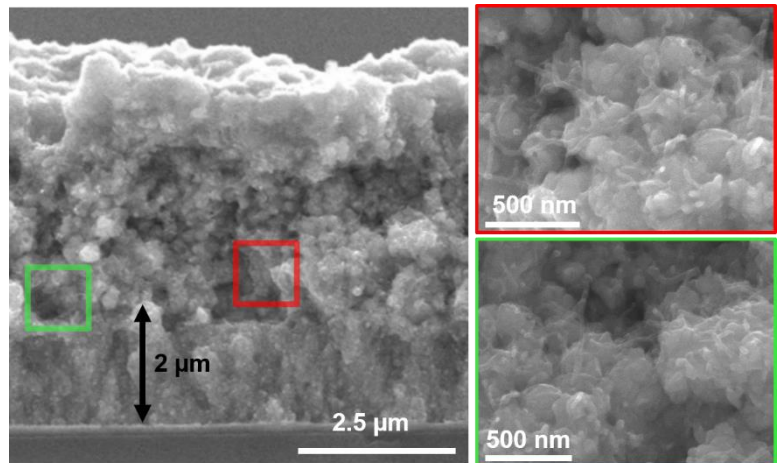


**Fig. 56.** SEM cross-sectional view of a MMC gridline deposited in LBL microstructure using Ag electrodeposition and CNT drop casting. The loading fraction of CNTs  $\sim 5 \times 10^{-5} \text{ g}_{\text{CNT}}/\text{cm}^2$  corresponding to  $\sim 70\%$  CNT surface coverage. Red and green boxes show the position of CNTs within the composite.

from the bottom (green and red boxed in Fig. 56) and appear to adhere strongly to the surrounding Ag matrix.

After depositing the MMC lines, the substrate is cleaved along the direction (red dashed line in Fig. 55) transverse to the applied mechanical strain, and the substrate is mechanically pulled apart while their electrical resistivity is monitored along the MMC lines.

When the MMC lines fail, the electrical resistivity rapidly rises, reaching infinity upon complete

failure, as indicated by the rapid rise in the log scale on y-axis of Fig. 55 [125]. Following the first electrical disconnect, the gap is incrementally closed in reverse until the electrical connection is reestablished across the gridlines (Fig. 55); the substrate is then pulled apart again. This process is repeated until no further change is seen in the gap width at which the connection is lost. Fig. 56 shows a pull test of a MMC gridline with 96% CNT coverage. After the second pull test, the maximum gap, at which the electrical connection is lost, is reduced by ~34% but subsequently remained constant with additional pull tests. Using the drop casting method, a set of MMC samples are prepared with different CNT surface coverage. The MMC gridlines are assessed, using the strain failure test. Four gridlines with the same CNT loading are tested, and the maximum and average gaps before

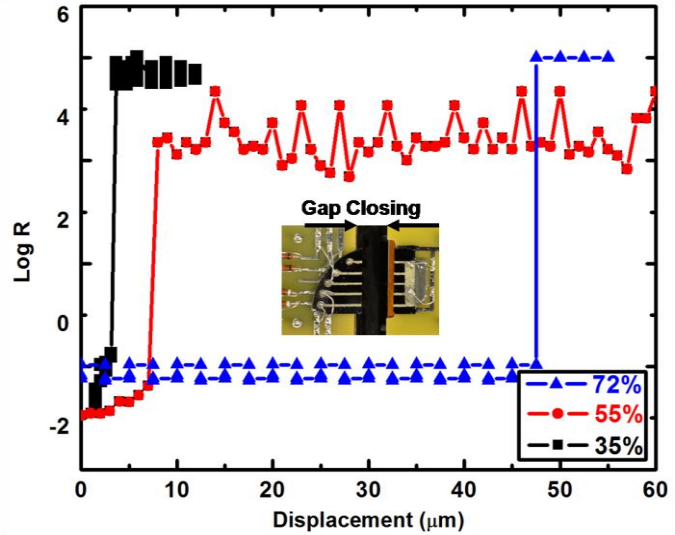


**Fig. 55.** Log plot of resistance vs. gap across fractured MMC gridlines with three different CNT surface coverages. The connection is reestablished at 49  $\mu\text{m}$ , 9  $\mu\text{m}$ , and 5  $\mu\text{m}$  for samples with CNT surface coverage of 72%, 55%, and 35%, respectively. Fig. adapted from Ref. [135].

the loss of electrical connection are recorded in Fig. 57. The pull tests reveal that the electrical connection is maintained across larger gaps with higher CNT surface coverage, reaching a maximum of 42- $\mu\text{m}$ -wide gap. As the CNT surface coverage increases from 35% to 96%, we observe a monotonic increase in the average gap.

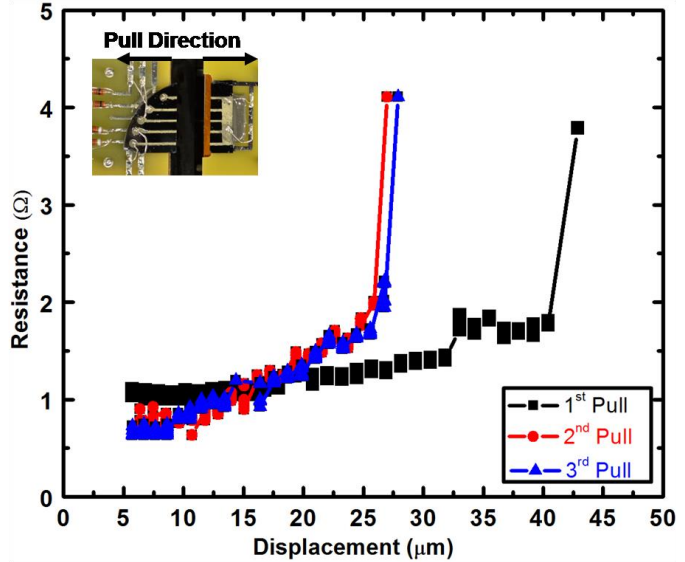


**Fig. 56.** Strain failure test of a MMC gridline (96% CNT surface coverage using drop cast method). The maximum gap, at which the electrical connection is lost, is reduced by ~34% after the 2<sup>nd</sup> pull test but remained constant after subsequent pull tests. Fig. adapted from Ref. [125].

Electroplated Ag lines without CNTs are also analyzed as control, using the strain failure test. Unlike MMC films, the Ag gridlines did not withstand the initial crack generated on the substrate (~4- $\mu\text{m}$ -wide), and the electrical connection is immediately and irreversibly lost.

It is clearly evident that the incorporation of CNTs within the Ag matrix enhances the electrical conductivity of metal lines upon fracture. To visualize this capability, we intentionally fracture a MMC film and examine the cracks under SEM. We observe CNTs of various lengths bridging gaps

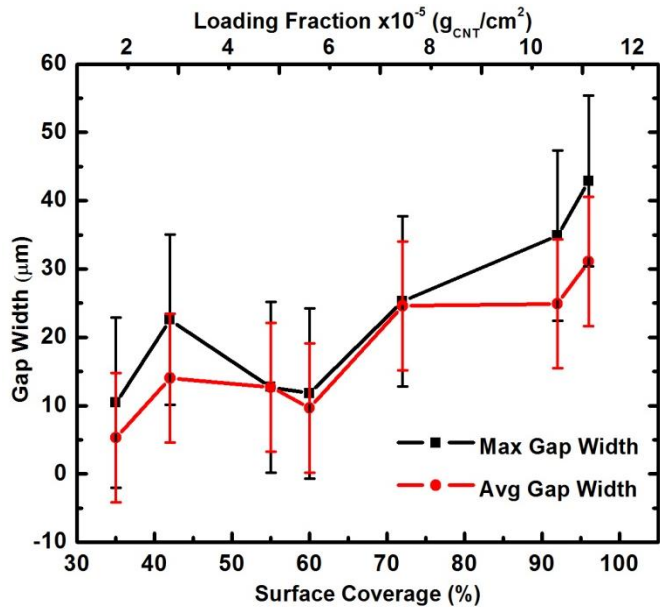


**Fig. 57.** Maximum and average gap widths achieved before lost connection as a function of CNT surface coverage and loading fraction. Fig. adapted from Ref. [125].

ranging from 0.2 to 9  $\mu\text{m}$ . The CNTs are anchored in the Ag matrix, indicating a good adhesion between the functionalized CNTs and the Ag matrix (Fig. 58). A typical current density through a MMC gridline under our testing is approximately  $750 \text{ A/cm}^2$  before

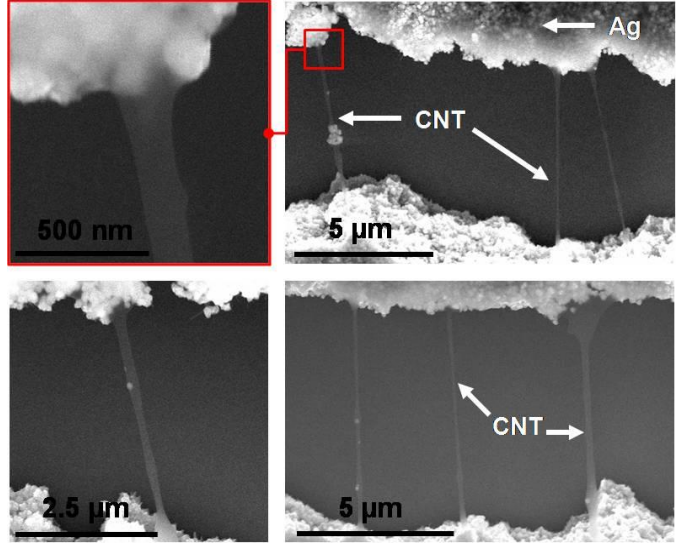


**Fig. 58.** Maximum and average gap widths achieved before lost connection as a function of CNT surface coverage and loading fraction. Fig. adapted from Ref. [125].

fracture. Once the crack is generated, the total current (30 mA) is conducted through only a limited number of CNTs at the fracture point, as shown in Fig. 58.

Using a four-point probe, we measure the sheet resistance (thus conductivity) of 2- $\mu\text{m}$ -thick Ag and then of the complete MMC composite layer after drop casting 600  $\mu\text{L}$  of CNT solution ( $2.2 \times 10^{-4} \text{ g}_{\text{CNT}}/\text{cm}^2$ ) and plating the final 2- $\mu\text{m}$ -thick Ag layer. Nine measurements are taken for each layer. The initial Ag layer shows  $1.2 \times 10^5/\Omega\text{-cm}$  conductivity. After applying the CNT layer and growing the 2<sup>nd</sup> Ag layer, the complete stack shows  $3.0 \times 10^5/\Omega\text{-cm}$  conductivity. Despite using low-purity, multi-walled CNTs, a higher conductivity ( $3.0 \times 10^5/\Omega\text{-cm}$ ) is observed for the complete MMC compared to pure silver ( $1.2 \times 10^5/\Omega\text{-cm}$ ), emphasizing the excellent electrical properties of CNTs and their good adhesion to the Ag matrix.

In this study [125, 126], we have developed and characterized Ag-CNT metal matrix composite (MMC) films that maintain electrical conductivity upon mechanical fracture of the substrate. Our composite lines are capable of bridging cracks in the

underlying semiconductor substrates up to 42  $\mu\text{m}$ . That is, the incorporation of CNTs within the Ag matrix renders the metal lines more resilient against mechanical failures, compared to the 100% Ag lines. In addition to maintaining the electrical conductivity over the stress-induced cracks, the composite films can reestablish the electrical connection when the cracks close up. This “self-healing” behavior of MMC gridlines is an important characteristic in light of the extreme temperature fluctuations encountered in space operations, in which the PV cells undergo constant expansion and contraction.

We replicated our efforts in depositing MMC gridlines using the different deposition methods of CNTs, i.e. spray-coating of CNTs [159]. To assess the success of this CNT deposition method in producing crack-tolerant gridlines we perform additional electromechanical **RACK** tests on MMC gridlines deposited using the

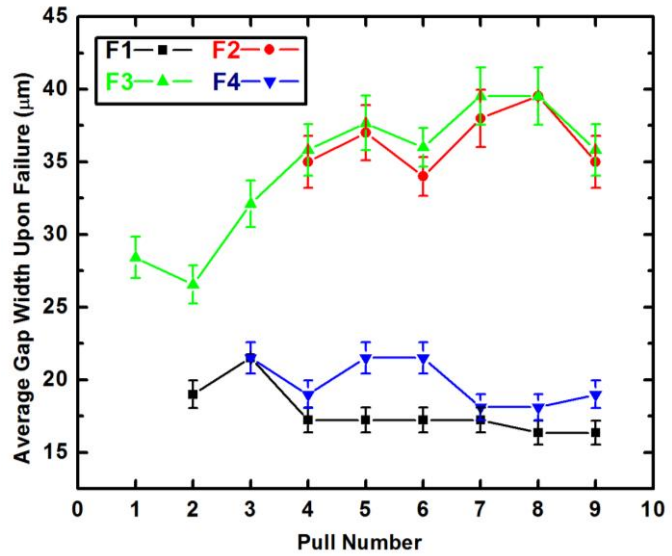


**Fig. 59.** Strain failure test of MMC gridlines. Fingers 1, 4 sustained an electrical connection across ~20- $\mu\text{m}$ -wide gaps while fingers 2, 3 maintained connection up to ~35- $\mu\text{m}$ -wide gaps. Fig. adapted from Ref. [159].

spray-coating technique. We deposit 1-mm-wide and 6- $\mu\text{m}$ -thick MMC gridlines in a LBL structure. First, a 3- $\mu\text{m}$ -thick Ag layer is plated on the substrate followed by spray-coating 15 layers of CNTs ( $p_o = 20$  psi,  $h = 10$  cm,  $s = 3.6$  mm/s). A final 3- $\mu\text{m}$ -thick Ag layer is plated on top of the CNT network. Pull tests are first performed at 6V and 30 mA. When the first complete failure of all gridlines occurs, and the electrical connection is completely lost, the stage is reset, and the pull test is repeated. A total of 9 pull tests and 8 resets are

performed. Fig. 59 shows the average gap width, at which each of the gridlines maintains electrical connection with successively additional pulls. This clearly shows that the incorporation of CNTs within the Ag matrix enhances the electrical conductivity of metal lines upon fracture. These results are consistent with our strain failure data of other MMC lines prepared using drop casting method [125, 126], indicating that spray-coating is a suitable alternative method of CNT deposition with high-throughput. As seen in Fig. 59, two out of the four gridlines maintained electrical conductivity across 35- $\mu\text{m}$ -wide gaps (F2, and F3), while the remaining two lines (F1 and F4) lost connection at  $\sim 20$ - $\mu\text{m}$ -wide gaps. The discrepancy in the pull data between the four gridlines could be explained by the arrangement of the gridlines on the test structure. Gridlines F2 and F3 are the middle finger on the test sample while F1 and F4 are the outer gridlines. Given the Gaussian distribution surface profile in spray deposition, middle grid fingers (F2, and F3) get a higher CNT surface coverage compared to outermost fingers (F1, and F4), hence can maintain electrical connection across wider gaps. These results correlate with the CNT drop casting method of deposition (Fig. 57), in which electrical connection is maintained across wider gaps at the higher CNT loading.

In order to evaluate the current carrying capability of MMCs, the gridlines are pulled apart gridlines at three gap widths (5, 10, and 15  $\mu\text{m}$ ), and a current-voltage ( $I$ - $V$ )

sweep is performed up to 30V [159]. We observe a linear behavior between current measured and voltage applied independent of the gap width (Fig. 60), which further highlights the excellent electrical properties of CNTs [47, 51]. MMC gridlines (1-mm-wide

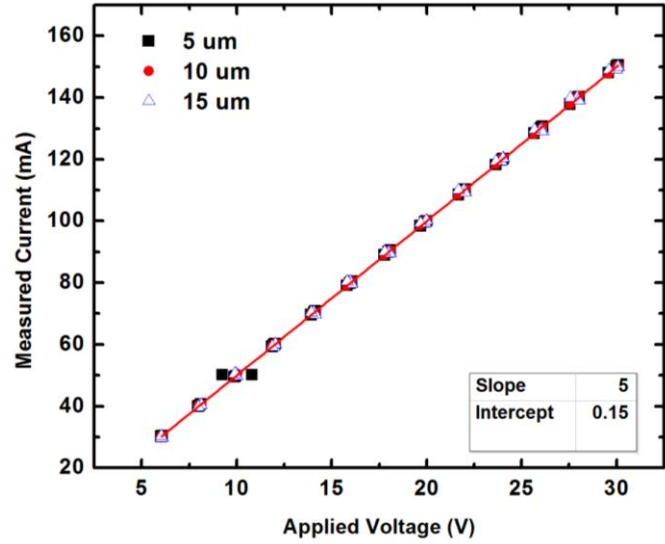


**Fig. 60.** Voltage current sweeps of fractured MMC gridlines at 5, 10 and 15  $\mu\text{m}$  displacements. Fig. adapted from Ref [159].

and 6- $\mu\text{m}$ -thick) are capable of maintaining current densities ranging from 500 to 2500  $\text{A}/\text{cm}^2$ , even after the microcracks form. Due to the voltage and current limits of our power supply, we are able to perform  $I$ - $V$  sweeps up to 30V and 150 mA only; therefore, we expect the maximum achievable current density to be much greater than 2500  $\text{A}/\text{cm}^2$ . These current densities well exceed the requirements for PV cells; Boeing-Spectrolab recorded a current density of 52.7  $\text{mA}/\text{cm}^2$  for a 1  $\text{cm}^2$  inverted metamorphic triple junction (IMM3J) cell under AM1.5D [201, 202].

In this work presented here, we demonstrate the use of a fast, cost-effective, and easily scalable method of depositing CNTs using a spray-coating technique. We develop MMC gridlines in a LBL microstructure that are capable of withstanding fractures up to 35- $\mu\text{m}$ -wide. MMC lines can reestablish and maintain electrical connection once gridlines are reset to their starting position. Therefore, spray-coated CNTs provide an electrical bridge support, should the microcracks propagate through the metal gridlines, preserving the power generation of the cell. In addition, MMC gridlines have measured current



densities ranging from 500 to 2500 A/cm<sup>2</sup>, which far exceeds the typical current densities of space PV cells.

### **MMC integration on PV cells**

Given the success of MMC gridlines in bridging gaps in the underlying semiconductor we advance our research efforts into integrating MMC onto active photovoltaic (PV) solar cells and evaluate the performance of MMC-enhanced cells vs. traditional cells with metal gridlines. In this effort, we first optimize the MMC deposition on active cells. Two sets of 2 cm x 2 cm TJ cells with atypical metallization pattern are purchased from *SolAero Tech*. The first set has conventional front metallization and second included only a seed metal layer evaporated on the semiconductor. The gridline width on TJ and the front contact pad was made larger for all cells in order to aide in MMC integration and testing. The cells with the seed metal layer have an additional layer of photoresist (PR) spun on them, exposing only the metal gridlines for subsequent integration of the MMC lines on top. A custom made plexi glass holder is developed to secure the fragile TJ cells during MMC integration. The holder consists of two complementary identical pieces, with open windows exposing the front and back side of the cell to allow contact with the Ag electrolytic solution. Non-cyanide alkaline silver plating solution (E-Brite 50/50 RTP, *Electrochemical Products Inc.*) is used as the Ag source. Low-cost dry MWCNTs (*SWeNT*) are functionalized and suspended in water. For a more detailed description on CNT solution preparation and Ag plating optimization refer to Ref. [125] and Ch. [2 – 3]. The CNTs are deposited through spray coating the CNT aqueous

suspension using an air brush technique. The full description of the CNT deposition method can be found at Ref. [159] and Ch. 3.

Following the first electroplated Ag layer on TJ cells the entire cell is spray coated with an aqueous CNT solution (1.3g/L). The cells are sprayed 15 times resulting in complete surface coverage of CNTs on Ag. Through controlling the stage scan speed (substrate pull rate under the spray nozzle) and the substrate temperature we are able to deposit thin, uniform layers of CNTs across the entire surface of the cell. The solvent dried upon impact, leaving behind functionalized MWCNTs. The cells are then transferred back into the electrolytic solution for a final deposition of Ag. A cap layer of Ag is electroplated at  $-6.7\text{mA/cm}^2$  for 500 s, depositing  $\sim 1\text{-}\mu\text{m}$ -thick Ag. A short secondary plating time is chosen in order to deposit Ag non-conformally on the cell, mainly plating over the gridline

pattern, otherwise Ag electrodeposits over the PR regions covered with conductive CNTs. Samples are then rinsed with water to remove residual plating solution and soaked in acetone for liftoff.

To verify integration of CNTs within the metal matrix and their homogenous dispersion, the MMC gridlines are examined through a scanning electron microscopy (SEM) using a *Hitachi*

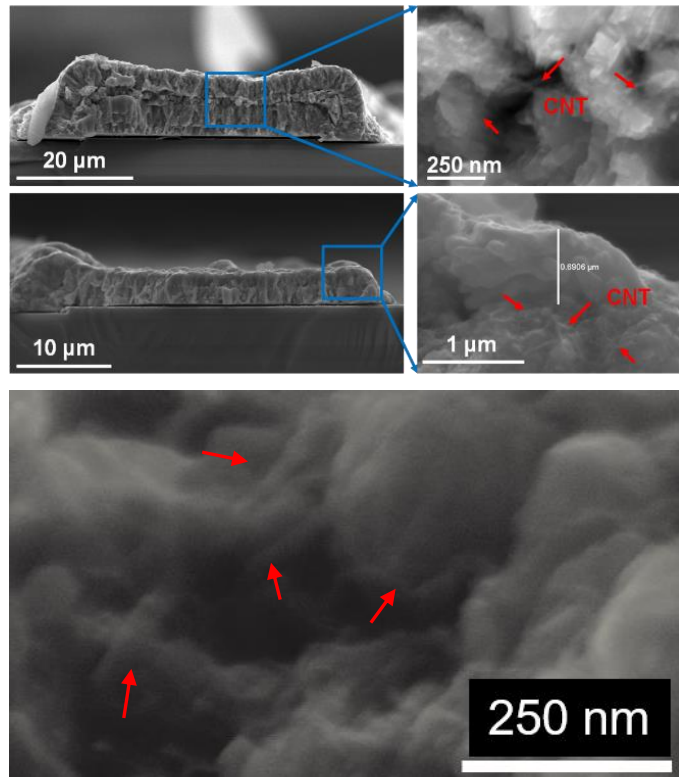


**Fig. 61.** Cross-sectional SEM micrographs of MMC gridlines on TJ cells. CNTs indicated by red arrows, Ref. [203].

*S-4300* at 20 KeV. Fig. 61 [203] shows a cross sectional-view of two cells with MMC gridlines. Initial deposition attempts result in thick (~15- $\mu\text{m}$ -thick) MMC stack; the recipe is later adjusted to a shorter Ag deposition times to obtain ~6- $\mu\text{m}$ -thick gridlines. CNTs can be seen in the enlarged SEM view (Fig. 61, red arrows). The CNTs are localized within the stack at a specified depth and appear to adhere well to the surrounding metal matrix. No agglomeration of CNTs into bundles is observed within the stack, suggesting well dispersion of CNTs due to adequate functionalization.

The cells are characterized through *LIV* and *DIV* sweeps and EL. An X-25 solar simulator (Mark II, *Spectrolab Inc.*) is used to perform the *LIV* sweeps. The beam is first calibrated using a standard TJ cell, and values are reported under AM0 spectrum. For the *DIV* sweeps a Kiethly 2400 series source meter is used. The solar cells are measured under black cloth to get the most accurate readings. The *DIV* sweeps are performed from 0 – 2.6 V. EL measurements [34, 204-207] are performed by forward biasing the cells at 30 mA. The top subcell (GaInP) strongly emits in the visible region ( $\lambda = 683\text{nm}$ ) [206] when forward biased and can be easily examined with the naked eye. The EL responses of the other subcells are not examined in this study because we are primarily interested in examining the effects of metal gridlines failure due to microcracks on the cell performance. These characterization results are included in the later results section.

MMC gridlines are integrated on TJ cells in a LBL microstructure. *LIV* is performed in conjugation with EL measurements of top subcell to monitor the cells' performance. For EL the cells are forward biased at 30 mA thus carriers are injected into the cell through electrical means rather than light generated current. We baseline cells with MMC gridlines against a TJ control sample with standard metallization. Fig. 62 [203]

shows the summary of *LIV* data for the cells. Initial attempts of integration resulted in less than ideal performance of the cells (Fig. 62, MMC 1 – 3), however, with further optimization of the deposition method the cell performance is significantly improved (Fig. 62, MMC 4 & 5). The most significant improvement is seen

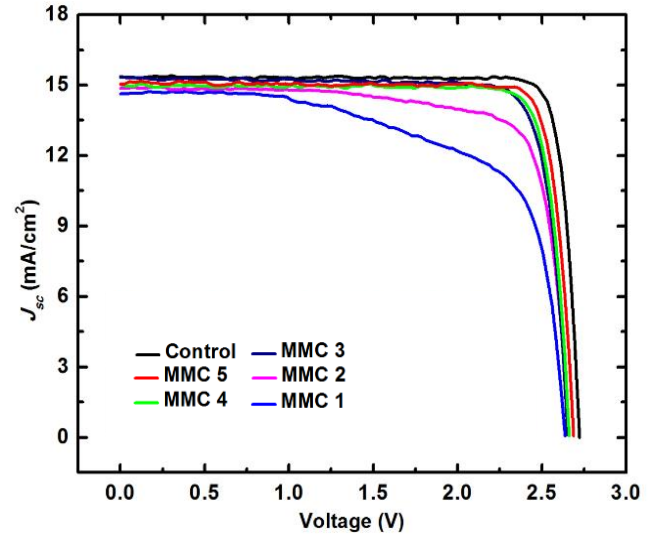


**Fig. 62.** LIV characteristics of TJ cells after depositing MMC gridlines, Ref. [203].

in the fill factor (*FF*) and efficiency ( $\eta$ ) reaching 86% and 26%, respectively, Table 2 summarizes the percentage change in MMC-enhanced cell parameters ( $V_{oc}$ ,  $J_{sc}$ , *FF*, and  $\eta$ ) relative to control sample. The deposition process is optimized by properly sealing the cell edges during

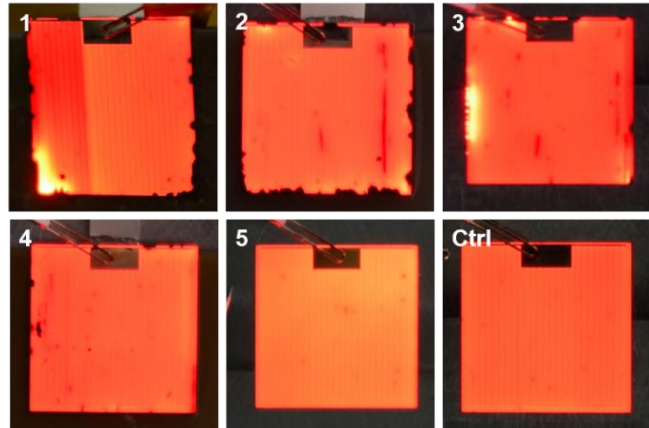


**Fig. 63.** EL response following the integration of MMC gridlines. Samples 1 – 5 are compared to a control TJ cell with standard metallization, Ref. [203].

Ag electroplating. The electrolyte solution used is alkaline based with trace amount of KOH, which is a known etchant for most III-V materials [208, 209]. This can be seen in the EL image of MMC 1 – 3 (Fig. 63) where a non-uniform EL response is observed particularly around the cell edges. The dark spots observed are due to KOH etching of the exposed semiconductor material. On the other hand, cell 5 (Fig. 63) shows a TJ cell with

full MMC gridlines that was properly sealed during Ag deposition. A uniform EL response is obtained for cell 5, without any dark spots which is a comparable EL response to the control sample.

**Table 2**  
Summary Results of Percentage Change in Cell Performance upon MMC Integration

<i>Sample</i>	$\% \Delta V_{oc}$ (V)	$\% \Delta J_{sc}$ (mA/cm <sup>2</sup> )	$\% \Delta FF$ (%)	$\% \Delta \eta$ (%)
<i>MMC 1</i>	3.0	4.0	38	43
<i>MMC 2</i>	1.9	3.3	17	22
<i>MMC 3</i>	1.4	1.4	11	14
<i>MMC 4</i>	1.1	2.8	3.8	7.5
<i>MMC 5</i>	1.2	1.8	1.8	4.8

To confirm successful integration of MMC gridlines we examine the diode properties through *DIV* measurements. Fig. 64 shows the typical diode characteristics at the linear scale and at the log scale (Fig. 64 inset). The diode characteristics improve going from MMC cell 1 to MMC cell 5. Past 1.5V, cells 4 & 5

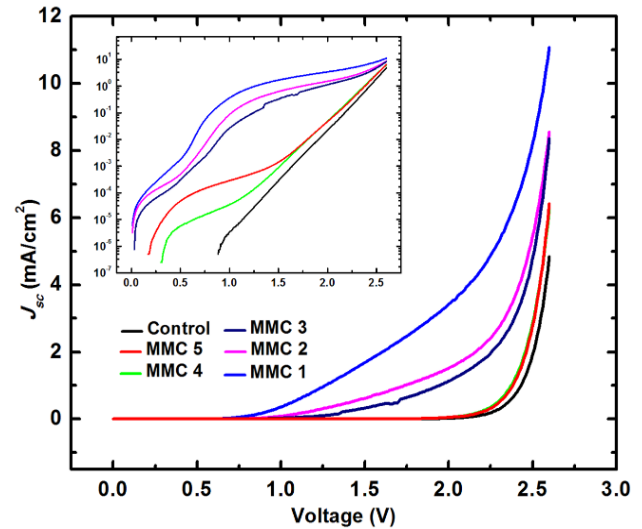


**Fig. 64.** *DIV* scans on linear scale and log scale (figure inset) of TJ cells after depositing MMC gridlines, Ref [203].

shows similar diode ideality factor as the control sample. For applied voltage < 1.5 V there appears to be a deviation in the performance of cells 4 and 5 from the control, this may be attributed to an increase in the shunt resistance of the cells. In contrast, cells 1 – 3 exhibit poor diode characteristics with a pronounced deviation from the control. The non-ideal diode characteristic of cells 1 – 3 is consistent with the poor *LIV* performance, which is

largely due to the non-radiative recombination on the exposed areas of the cells that are etched away during Ag deposition.

### Solar Cell Characterization Methods

An important aspect of our MMC work is the ability to properly evaluate the gridlines upon integration on active PV cells through the proper characterization of the cell parameters. In this section, different key characterization methods will be discussed, including light current-voltage sweeps (*LIV*), dark current-voltage sweeps (*DIV*), and electroluminescence (EL) measurements. Key cell parameters will also be discussed including, open circuit voltage ( $V_{oc}$ ), short circuit current density ( $J_{sc}$ ), fill factor (*FF*), and efficiency ( $\eta$ ).

The most fundamental characterization technique of a solar cell is the measurement of cell efficiency. Standardized testing allows for comparison of different PV devices from different manufacturers to be tested and compared under the same conditions. These

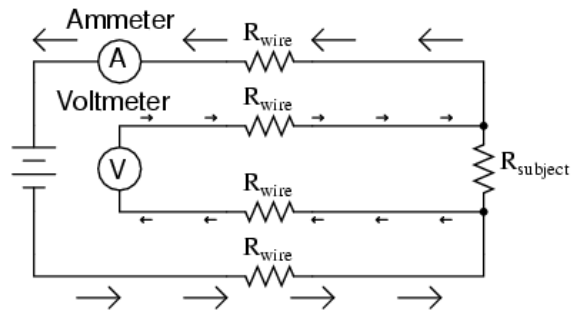


**Fig. 65.** Four-wire measurement circuit setup. This four-point measurement is used to eliminate probe/cell contact resistance to get accurate measurements during PV characterization.

standards include [210] Air Mass 1.5 spectrum (AM1.5) for terrestrial cell and Air Mass 0 (AM0) for space cells, an intensity of  $100 \text{ W/cm}^2$ , equivalent to one-sun illumination, and a fixed temperature of  $25^\circ\text{C}$ . A four-point wire measurement is used to remove the effect of probe/cell contact resistance. Fig. 65 shows the circuit diagram for the four-wire measurement, in which the flow test current passes through one set of wires (force) while

the voltage is measured from the second pair of wires (sense), hence eliminating the resistance of wires/leads. A basic setup of a simple  $IV$  tester is shown in Fig. 66. The current and voltage can be measured separately from

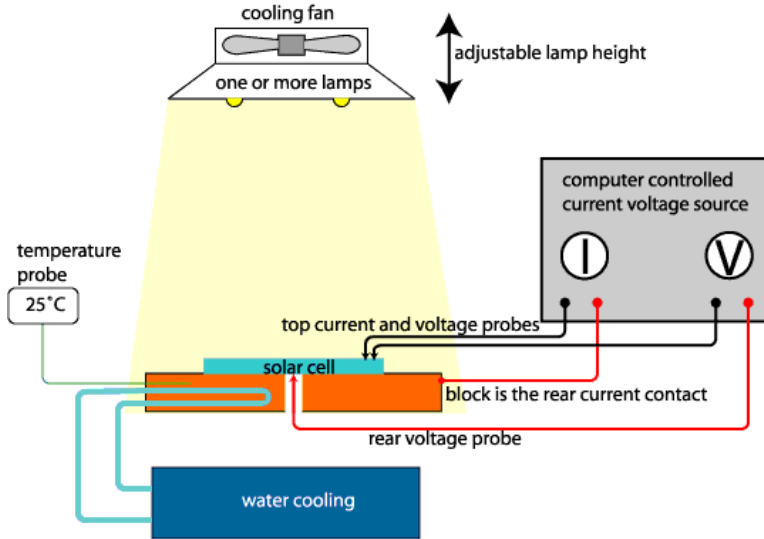


**Fig. 66.** Basic structure of an  $IV$  tester used for LIV characterization of solar cells, Ref. [210].

the power source. The height of the lamp is adjusted rather than power to keep the lamp spectrum constant during calibration of the system. Calibration is typically carried out using a standard cell with known parameters, the standard cell is usually of the same type of the cells being testes (Si terrestrial cell, single-junction GaAs, full TJ cell...etc.).

Without illumination, a solar cell has the same electric characteristics as a large diode and the normal “dark” current is expressed as follows

$$I = I_0 \left[ \exp\left(\frac{qV}{nkT}\right) - 1 \right] - I_L$$

where  $I_0$  is the dark saturation current,  $q$  is elementary charge,  $V$  is voltage applied,  $n$

is the ideality factor,  $k$  is the Boltzmann’s constant, and  $T$  is the temperature.  $I_L$  is the light generated current, which equals to zero in the dark. As the cell gets illuminated the  $IV$  curve gets shifted down into the fourth quadrant where power can be extracted from diode.

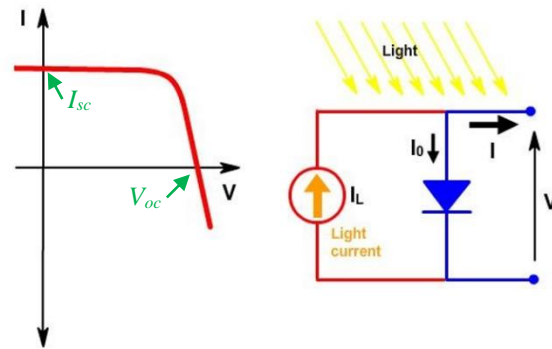


**Fig. 67.**  $IV$  curve of a solar cell showing the short-circuit current ( $I_{sc}$ ) and open circuit voltage ( $V_{oc}$ ), Ref. [211].

Since the cell is generating power, the convention is to invert the current axis (Fig. 67). Another important cell parameter directly relating to the  $I_L$  is the short circuit current ( $I_{sc}$ ), shown in Fig. 67 [211], which is defined as the current through the solar cell when the voltage across it is zero. For an ideal cell  $I_{sc}$  and  $I_L$  are identical. Hence, the short-circuit current is the largest current which may be drawn from the solar cell, and is often expressed in terms of the cell's area as the short circuit current density ( $J_{sc}$ ) to remove the dependence of the solar cell area.

While the short circuit current is defined as the current through the cell at zero voltage, similarly the open circuit voltage ( $V_{oc}$ ) is defined as the voltage available from the solar cell when the net current is zero. The open circuit voltage corresponds to the amount of forward bias of a solar cell due to the bias of the cell junction with the light-generated current, shown in Fig. 67.  $V_{oc}$  can be directly calculated from the above solar cell equation by setting the net current equal to zero to give:

$$V_{oc} = \frac{nkT}{q} \ln \left( \frac{I_L}{I_0} + 1 \right)$$

Therefore, the  $I_{sc}$  and  $V_{oc}$  are the maximum current and voltage respectively from a solar cell. However, at either one of these points, the power obtained from the cell is zero. To determine the maximum power derived from a solar cell, the fill factor ( $FF$ ) parameter is used instead. Fill factor is defined as the ratio of maximum power from solar cell to the product of  $V_{oc}$  and  $I_{sc}$ . Graphically, the  $FF$  is a measure of the “squareness” of the IV curve. Hence, a solar cell with a higher voltage has a larger possible  $FF$  since the “rounded” portion of IV curve takes up less area.  $FF$  is determined from measurements of IV curve and is defined as the maximum power divided by the product of  $I_{sc}$  and  $V_{oc}$  as follows:

$$FF = \frac{V_{MP}I_{MP}}{V_{oc}I_{sc}}$$



Finally, the last relevant parameter to be addressed is the solar cell efficiency ( $\eta$ ). Efficiency is the most commonly used parameter to compare performance of one cell to another, and it is defined as the ratio of energy output from the solar cell to input energy from the sun. Efficiency depends on intensity of incident light and temperature of the solar cell, therefore, conditions under which efficiency is measured must be controlled, as mentioned earlier, to accurately compare one device performance to another. The efficiency of a solar cell is determined as a function of incident power which is converted to electricity and is defined as follows:

$$\eta = \frac{P_{max}}{P_{in}}$$

where maximum power ( $P_{max}$ ) is defined as the product of  $V_{oc}$ ,  $I_{sc}$ , and  $FF$

$$P_{max} = V_{oc}I_{sc}FF$$

An important characterization tool for evaluating the performance of PV devices is dark  $I$ - $V$  ( $DIV$ ) measurements. The diode properties of the solar cells are examined in the dark through injecting carriers into the circuit electrically. Using this diagnostic tool, the diode properties could be examined more closely giving

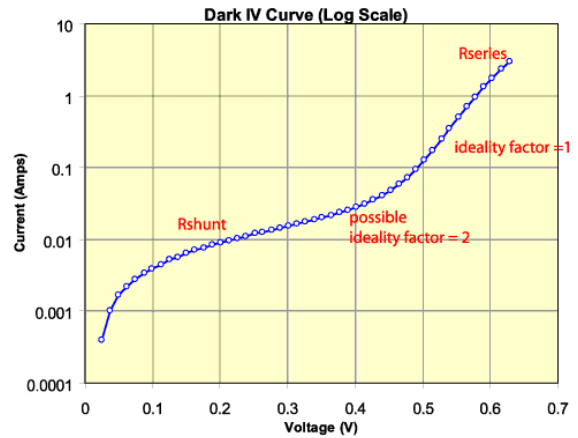


**Fig. 68.** Example of an  $IV$  curve of a solar cell plotted on a semi-log plot, Ref. [212].

insight into the different regions of the  $IV$  curve. A traditional  $IV$  curve on the linear scale does not usually reveal much information, however, a semi-log plot of the same  $IV$  curve reveals much more information about the diode, in particular the different loss

mechanisms. For example, Fig. 68 [212] is semi-log plot of an  $IV$  curve of a solar cell, showing the dominated loss mechanism at different part of the  $IV$  curve.

Among the characterization methods electroluminescence (EL) is a non-destructive and fast method of characterizing solar cell. The cells are forward biased behaving as a light emitting diode (LED). As current is fed into the solar cell and radiative recombination of carriers causes the light emission. This is shown in the band diagram in Fig. 69. Under forward bias of the homojunction the  $p$ -side is made more positive, hence reducing

the energy barrier for the electron to cross the junction. Therefore, an electron can move more readily across the junction and recombine with a hole, emitting light photons. In indirect band gap materials, such as Si, most of the recombination occurs due to Auger recombination, producing relatively low radiative emission. This technique requires electrical contacts and can only be performed when metallization has been applied to the cell. The intensity of the light given off is proportional to the voltage, therefore, poorly contacted and inactive regions show up as dark spot/areas which would not be visible under visual inspection otherwise.

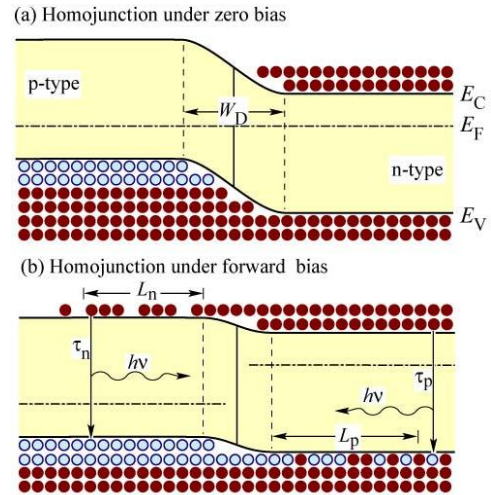


**Fig. 69.** Band diagram of a homojunction (a) under zero bias, and (b) under forward bias.

### Effects of Microcracks on Performance of TJ Solar Cells

In the work presented in this section we investigate the effects of microcracks on the cell performance of commercial triple-junction (TJ) cells. Cracks are introduced on the

TJ cells using two approaches, firstly introducing single cracks at specified location on the cells using a mechanical fixture, and secondly generating multiple cracks in a random fashion through mounting the TJ cells on a thermally mismatched substrate. The cell performance is analyzed before and after introducing cracks through performing *LIV*, *DIV*, and EL of top subcell. The cells are further examined under a scanning electron microscope (SEM) evaluating the size the direction of cracks.

### **Experiment Methods**

We use a one line bending setup [see Fig. 70] to stress the TJ cell from the top surface in order to create single cracks. The setup consists of a metal rod that is fed through circular metal bearings mounted on a movable stage. The rod is 3.30 mm in diameter and can rotate freely around its axis. The stage is controlled in the *z*-direction through an attached micrometer (*Starrett* micrometer no. 263) to precisely control the height of the movable stage/rod relative to the sample. Our test cells consist of 27 cm<sup>2</sup> ITJ cells (GaInP<sub>2</sub>/GaAs/Ge) purchased from *Spectrolab, Inc.* The cells are diced into 2 cm x 2 cm squares using a diamond scribe. The 2x2 cm<sup>2</sup> cells are then mounted on a 5-mil-thick adhesive kapton tape (45° angle relative to tape edge) and a silver-plated kovar tab (*American Etching & Manufacturing*) is soldered on the cell back contact in order to probe the back surface. The cell attached to kapton tape is fed through a groove on an adjacent fixed stage protruding ~5 mm of the cell from the stage edge. The cell is held in place by resting a glass slide on the top surface and metal rod is brought into contact with the cells using the micrometer. Once in contact with the cell the metal rod is further lowered 2.8 – 3.3 mm ( $\delta$ , Fig. 70) creating a single crack.

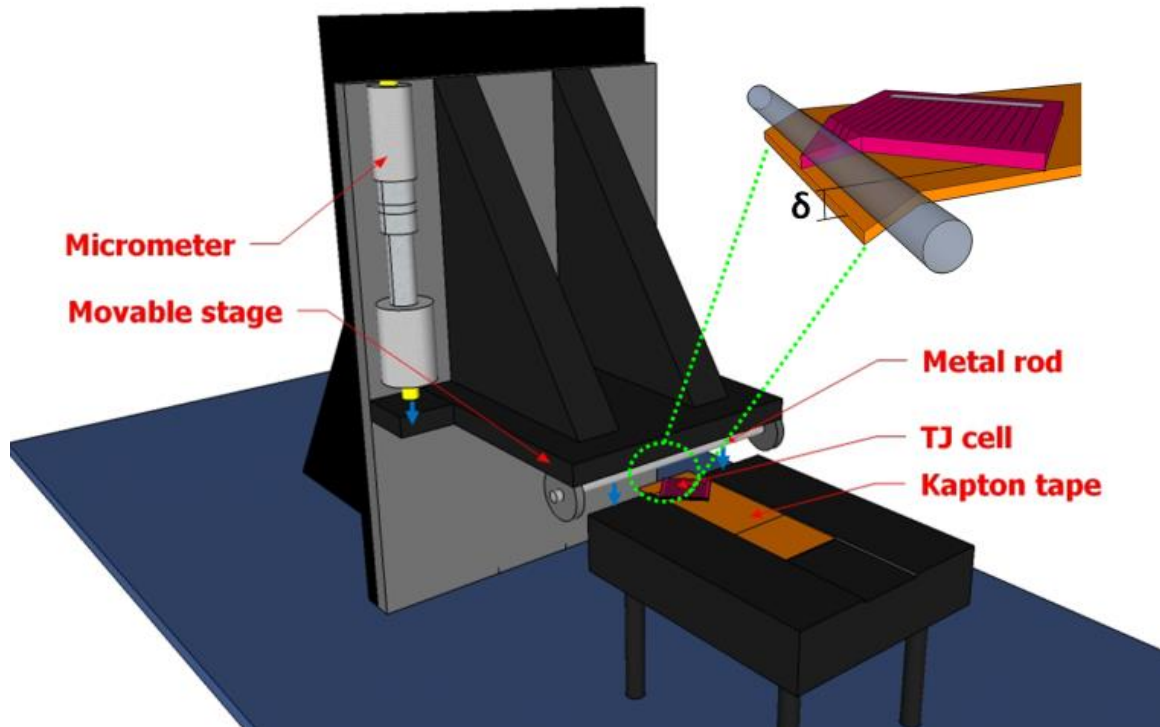


**Fig. 70.** Test setup structure of the on-line bending technique used to introduce single cracks on ITJ cells. The micrometer is used to lower metal rod a known distance ( $\delta$ ). The ITJ solar cells are attached to kapton tape and held on a fixed plate, protruding the sample edge by  $\sim 5$ mm.

In order to produce multiple cracks on the cells we subject TJ cells to thermally induced stress using a thermally mismatched substrate. For this method, we make use of low-cost microscope glass slides (*ThermoScientific* cat. # 2950-4-001). A 20-mil-thick layer of epoxy (*Resinlab* EP11HTFS) is used as the adhesive. The epoxy is first spread on the glass slide covering the entire width of the underlying slide and about 30 mm in length. TJ cell, with

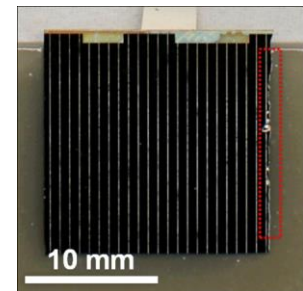


**Fig. 71.** A 2cm x 2cm diced sample of an ITJ solar cell mounted on glass slide using an epoxy. The red box shows the stress points created during the dicing process.

metal tab soldered on the back contact, is carefully laid on top of epoxy with a slight offset from the glass slide edge [see Fig. 71]. We intentionally offset the cells for two reasons; first we want to preserve the busbar region for further testing and characterization. This offset would minimize the cracks that could potentially reach the busbar region. Second, due to soldering on the tab on the back contact, the surface thickness is no longer uniform.

Therefore, to accommodate for the new thickness the cells are offset from the edge, resulting in a flat cell in contact with epoxy. The entire setup (glass slide, epoxy, TJ cell) is then cured at 180°C for 15 min (*Fischer Scientific* isotemp oven) in ambient air and then cooled to room temperature. The samples are then immersed in liquid nitrogen (-196°C) for 15 s to induce cell fracturing. It should be noted that the mechanical stability of the cell is lowered during the dicing process of the original cells. As indicated in the red box on Fig. 71 the presence of stress points along the sample edge from the diamond scribe can be seen. These stress points are key factors in propagating the cracks upon thermal shocking of the cell.

The cells are initially characterized through *LIV*, *DIV*, and EL measurements to observe any effect curing or soldering may have on the cell properties. An X-25 solar simulator (*Spectrolab Inc.* Mark II) is used to perform the *LIV* sweeps. The beam is first calibrated using a standard TJ cell, and values are reported under AM0 spectrum. For the *DIV* sweeps a Kiethly 2400 series source meter is used. The solar cells are measured under black cloth to get the most accurate readings. The *I-V* sweeps are initially performed from 0 – 3.0V; however, the upper limit is later adjusted to 2.6 V (close to  $V_{oc}$  of the cell) due to observing a negative impact on cell properties past 2.6V. EL measurements [34, 204-207] are performed through forward biasing the cells at 30 mA. The top subcell (GaInP) strongly emits in the visible region ( $\lambda = 683\text{nm}$ ) [206] when forward biased and can be easily examined with the naked eye. The EL responses of the other subcells were not examined in this study because we are primarily interested in examining the effects of metal gridlines failure due to microcracks, on the cell performance. These characterization results are included in the following results section.

## Results and Discussion

### Single Crack

We examine the effect of single microcracks on cells performance by cracking 7-TJ cells. The results are reported in two separate groups. First group (cells A – D) represents samples in which *DIV* is performed up to 3.0 V. As mentioned earlier, this voltage range caused damage to the cell performance, prior to introducing cracks; hence the further evaluation of the impact of cracks on the cell performance is clouded due to the test artifacts introduced. The damage is observed with further inspection using *LIV* measurements, in which cells parameters ( $FF$ ,  $\eta$ ) are affected. The *LIV* and *DIV* results prior to cracking the cells are shown in Fig. 72. The average  $V_{oc}$  and  $J_{sc}$  of the four cells are 2.56 V and 16.3 mA/cm<sup>2</sup>, respectively. Prior to introducing any cracks, we observe dark spots/blemishes during EL measurements (Fig.72(a) insets, green dashed boxes). Dark spots are indicative of growth defects in the epitaxially grown layers [204]. In cell D, we observe a bright line surrounded by a dark region (Fig. 72(a) inset, yellow dashed circle) which is attributed to a microcrack in the cell resulting in broken fingers [206]. This

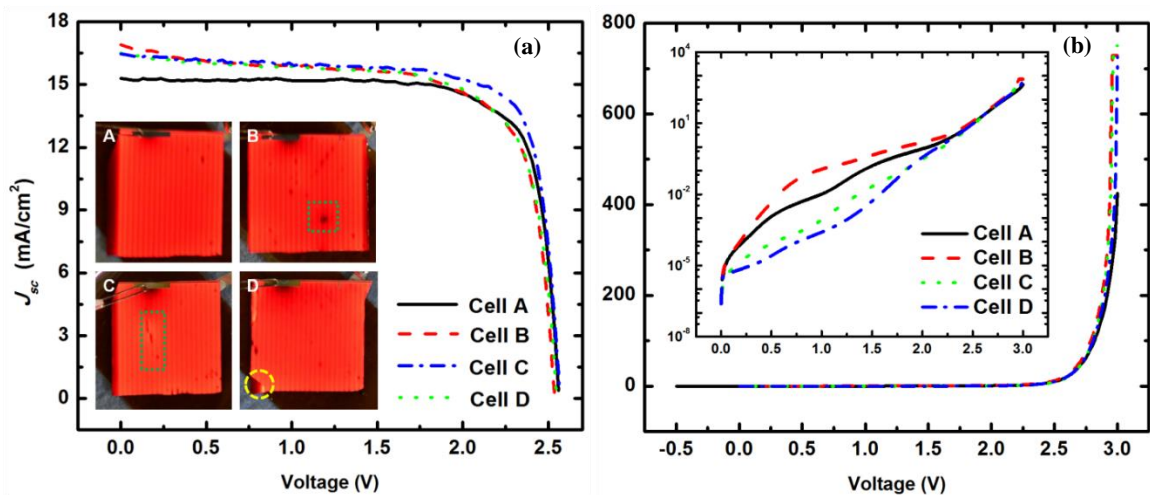


**Fig 72.** *LIV* (a) and *DIV* (b) measurements of group 1 of ITJ cells, in which the *DIV* measurements were performed up to 3.0V, causing damage to the cells.

crack may have been introduced during handling of the cell. The EL imaging technique is a non-destructive method of detecting broken fingers [213]; in the presence of a severed gridline the light intensity in the surrounding vicinity decreases, meaning that a broken finger not only affects the area underneath it but also nearby regions [206]. Fig. 72(b) shows *DIV* of the four cells, the graph is plotted on the semi-log scale (graph inset) to highlight the ideality factors of the cells.

Using the mechanical fixture (Fig. 70), cells A – D are cracked at specified location. Cell A is first cracked in the lower corner (cell A1, Fig. 73), and later additional cracks are introduced at multiple locations (cell A2, Fig. 73). The short circuit current density ( $J_{sc}$ ) for cell A is not affected, even upon introducing multiple cracks.

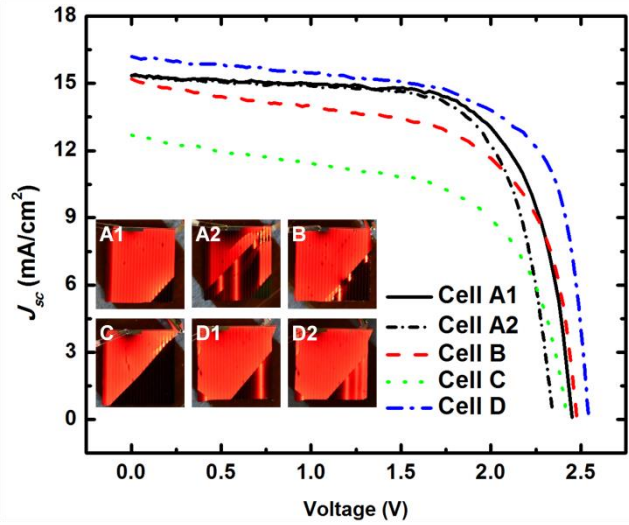


**Fig. 73.** *LIV* and EL measurements of group 1 of ITJ cell after introducing cracks on the cells.

However, open circuit voltage ( $V_{oc}$ ) is reduced from 2.55 V (pre-cracking) to 2.46 V (single crack) and 2.35 V (multiple cracks) which in turn reduced *FF* to 70% in both cases. The behavior of  $V_{oc}$  may be associated with introducing cracks in addition to passing high amounts of current during *DIV* measurements. In the second cracking attempt (cell A2) gridlines are not all completely disconnected. As seen in the EL response of the cell, some gridlines remain connected and appear brighter.

Cells B and D are cracked at approximately the same location but at different  $\delta$ -values. Cell B is cracked at  $\delta = 3.8$  mm, while cell D is cracked at  $\delta = 2.8$  mm. As can be

seen from the EL response of the two cells, the gridlines are more severely disconnected in cell B compared to cell D. Gridlines on cells D in the cracked regions briefly reconnect (cells D1 and D2), indicating that cracks did not propagate completely through the gridlines. Examining the *LIV* graph, cell B suffered a greater loss in  $J_{sc}$  (10%) compared to cell D (1.6%), which is to be expected if more gridlines are disconnected completely, i.e. electrically isolating a larger portion of the cell. *FF* of both cells are also reduced to 62% and 68% for cells B and D, respectively.

In cell C, almost half of the cell is cracked. Compared to the other cells, cell C suffered the biggest loss in  $J_{sc}$ , as to be expected. Considering that almost half the cell appeared inactive we expected that  $J_{sc}$  would scale accordingly, however, that was not the case. After introducing the crack on cell C,  $J_{sc}$  is only reduced by 23%. This smaller reduction in  $J_{sc}$  indicates that cracks did not propagate completely through all the gridlines in that region, where a fraction of the gridlines remained connected. The faint luminescence from that region may have not been captured due to the imaging camera limitations, which would correlate with the smaller than expected reduction in  $J_{sc}$ .

In the second group of samples (cells E – G) the *DIV* sweep is reduced to 2.6 V. We performed additional *LIV* scans following *DIV* ones to confirm that this range did not affect the cell performance. Hence, from this set of samples a clearer and more reliable conclusion can be drawn on the effects of single cracks on the cell performance. Fig. 74 shows the *LIV* results of the three cells before and after introducing cracks along with the associated EL images. Cell E is initially cracked at  $\delta = 3.8$  mm (E1) and then at  $\delta = 5.8$  mm (E2) in the same region. The initial crack did not seem to impact the  $J_{sc}$  or  $V_{oc}$  of cell E, however following the additional bending ( $\delta = 5.8$  mm) a more pronounced reduction



(11%) in  $J_{sc}$  is observed (Fig. 74a). EL images (E1, E2 Fig. 74a) confirm the behavior in  $J_{sc}$  where gridlines are partially disconnected at  $\delta = 3.8$  mm (E1), but lose connection at  $\delta \geq 5.8$  mm (E2). Cell F is cracked at  $\delta = 5.8$  mm only once. The cell's  $J_{sc}$  and  $V_{oc}$  are not affected (Fig. 74b), however, the most significant reduction is observed in  $FF$  (87% pre-crack to 77% post-crack) and  $\eta$  (26% pre-crack to 22% post-crack). Examining Fig. 74(b), the downward slope of the upper portion of the curve suggests a decrease in the shunt resistance of the cell upon introducing the crack. Typically, shunt resistance in solar cells arise due to manufacturing defects in which the cell suffers power loss as an alternate path for the light-generated current is

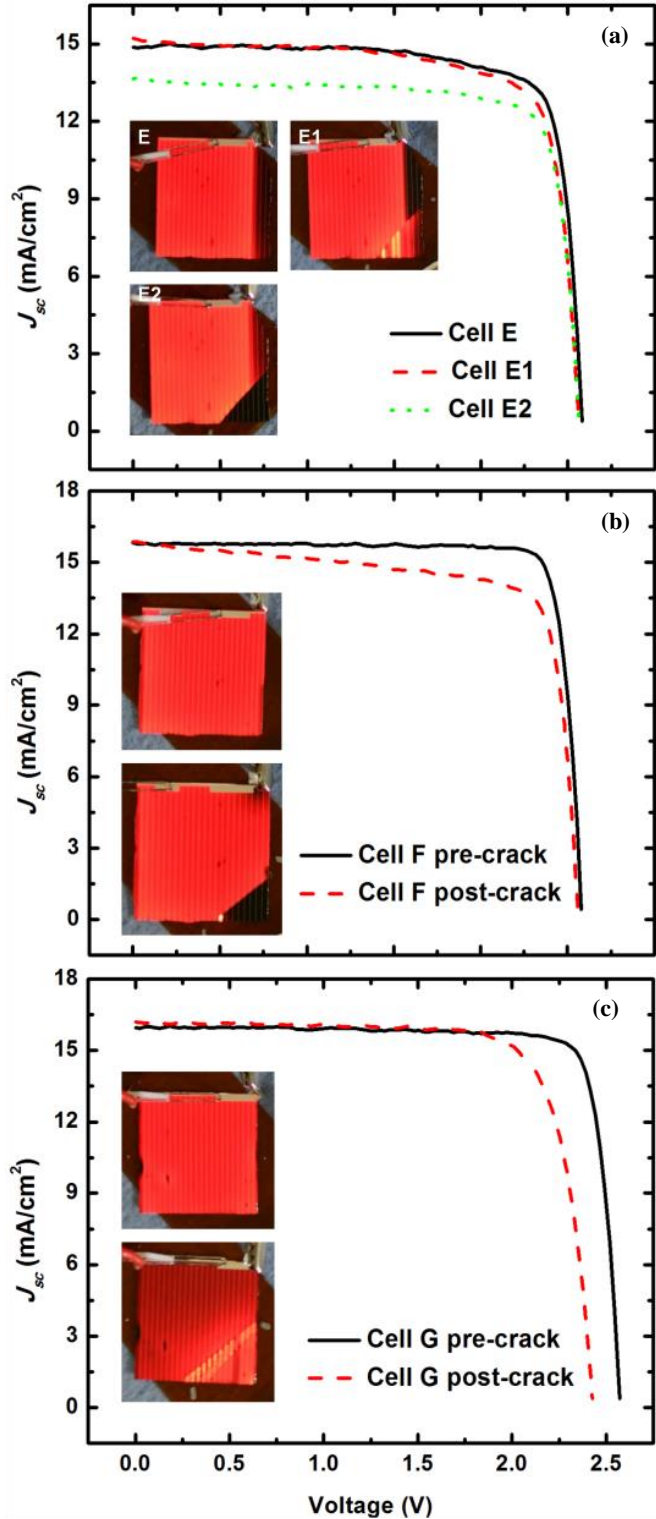


Fig. 74. LIV and EL measurements of second group of ITJ cells before and after introducing cracks.

provided. Clearly, however, the microcrack had an impact on the cell performance through a decrease in the shunt resistance of the cell. Finally, cell G is cracked at  $\delta = 3.8$  mm, as to be expected this did not result in complete failure of gridlines, as can be seen in the EL image of the cell post cracking. At the location of the crack (Fig. 74(c) inset) the EL intensity is brighter at the crack location and in the surrounding vicinity, while it is reduced for the further portions of the cell. The increased brightness indicates that more recombination sites for minority carriers are introduced at this location. A similar behavior is observed in [206], in which a bright region is observed in the top cell (GaInP) due to a microcrack that originated in the underlying subcell (GaInAs).

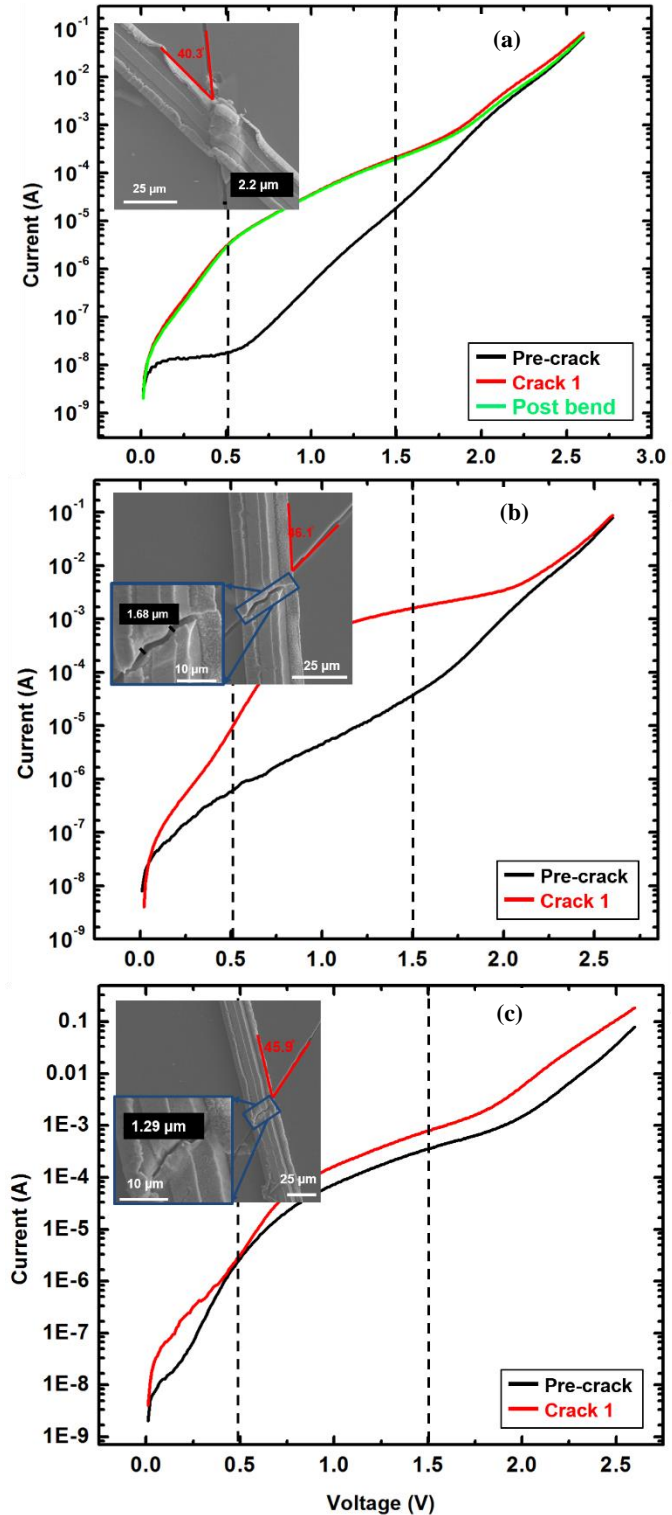


Fig. 75. *DIV*, plotted on semi-log scale, before and after introducing cracks and SEM micrographs of cracked gridlines of (a) cell E, (b) cell F, and (c) cell G.

*DIV* scans of cells E – G are shown in Fig. 75 along with SEM micrographs of the broken gridlines. In all three samples the most pronounced deviation in the diode characteristic is seen in the range from 0.5V to 1.5V (dashed lines in Fig. 75) after introducing microcracks. Sample G however, is not significantly affected. The cell performance is slightly affected, as seen in Fig. 74(c) (decrease in  $V_{oc}$ ), in which the generated crack is  $< 2 \mu\text{m}$  (Fig. 75(c), inset). These results correlate with *DIV* scan for sample G.

Using the one-line bending setup we can produce cracks  $\leq 2\text{-}\mu\text{m}$ -wide at  $\sim 45^\circ$  relative to the gridlines. The SEM analysis reveals that only a  $2\text{-}\mu\text{m}$ -wide crack is sufficient for the gridlines to lose electrical conductivity, hence resulting in power loss of the cell and the dark regions seen in the earlier EL images. These microcracks caused a reduction in either  $J_{sc}$  or  $V_{oc}$ , which in turn impacted the *FF* and  $\eta$  of the cells. In addition, we observe a decrease in the shunt resistance of the cell due to microcracks consequently causing a decrease in *FF* and  $\eta$ .

### ***Thermal Mismatch Multi-Cracking***

We are able to produce multi-cracks on ITJ cells simultaneously through mounting the sample on glass slide using epoxy technique. Two ITJ samples are analyzed and the performance is evaluated before and after cracking. Fig. 76. shows the *LIV* data with EL measurements. As can be seen clearly from Fig. 76, there is a significant difference in the performance of the two samples after introducing cracks. Given the stochastic method of creating the cracks, it is challenging to replicate the same frequency and location of cracks

from sample to sample. Hence, for sample (A) a more deleterious effect is observed, where the  $J_{sc}$  and  $V_{oc}$  were reduced by 64% and 16%, respectively, while sample (B) exhibited a less dramatic performance impact in which the  $J_{sc}$  and  $V_{oc}$  are reduced by 3% and 5%, respectively. This difference in performance after introducing cracks is confirmed through EL measurements (Fig. 76, image insets). A larger area of cell (A) becomes inactive due to cracking, corresponding to the larger dark areas. In comparison cell (B) had

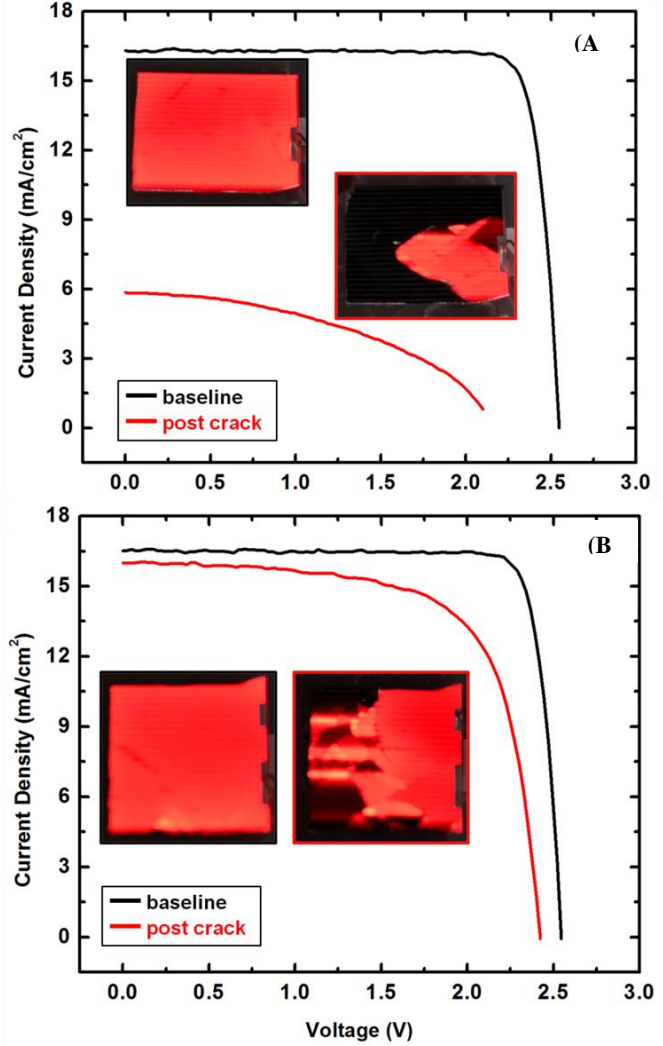


**Fig. 76.** *LIV* and EL measurements of ITJ sample before and after introducing microcracks through thermally-mismatched substrate cracking.

only a small inactive area without EL illumination. Examining the *DIV* performance of both cells (Fig. 77) we observe a more noticeable deviation in the performance of cell (A) vs. cell (B), particularly in the 0.5V – 1.5V range. These *DIV* results corroborate the *LIV* and EL measurements reported earlier. Table 3 summarizes the cell parameters of both cells before and after introducing cracks.

**Table 3**  
Summary of Cell Parameters Before and After Introducing Microcracks Using the Multi-Cracking Method Through Thermal Mismatching

<i>Sample</i>	$V_{oc}$ (V)	$J_{sc}$ (mA/cm <sup>2</sup> )	$FF$ (%)	$\eta$ (%)
<i>Cell A pre-cracking</i>	2.6	16	86	26
<i>Cell A post cracking</i>	2.1	5.9	46	4.1
<i>Cell B pre-cracking</i>	2.6	16.5	86	26
<i>Cell B post-cracking</i>	2.4	16	69	19

In the work presented here, we develop two ways of introducing microcracks on solar cells using a one-line bending setup to create single cracks at specified location, as well as introducing multiple-cracks simultaneously. The multiple cracks are introduced on the cells through thermally shocking a cell mounted on a thermally mismatched substrate. This later technique showed remarkable success in randomly creating cracks on cells, which is only possible through introducing stress points on the cell during

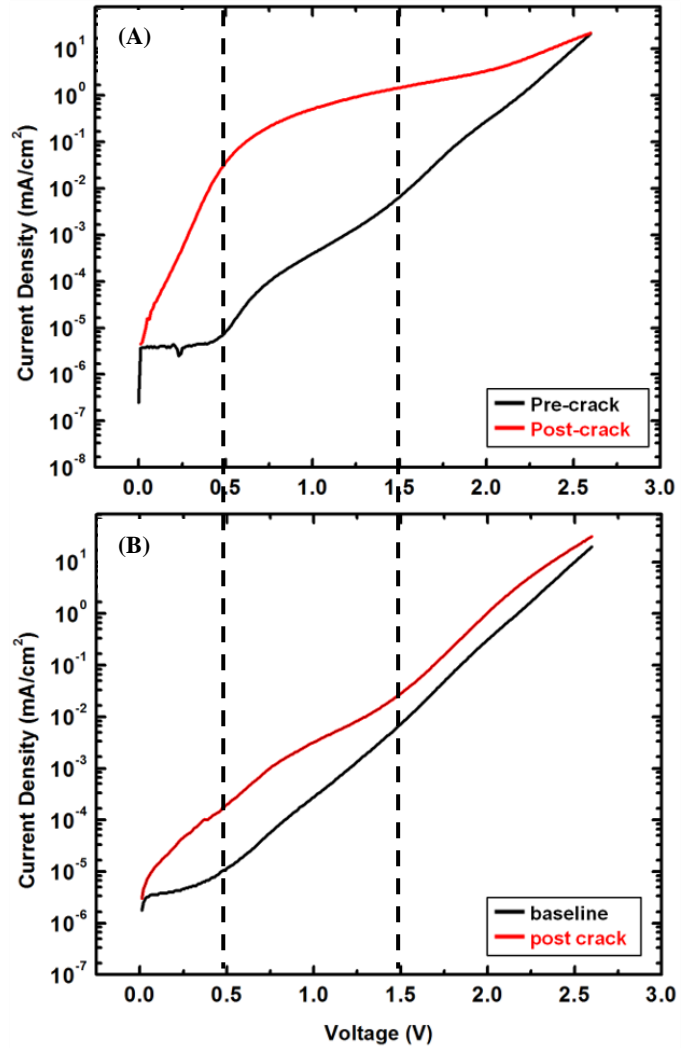


**Fig. 77.** DIV scans of cell before and after cracking through thermally shocking the cells that are mounted on a thermally mismatched substrate.

scribing. We investigate the effects of cracks on the cells performance in both cases, examining cell parameters through the different characterization techniques (*LIV*, *DIV*, EL and SEM). Using the single-crack method we observe a loss in  $J_{sc}$ ,  $V_{oc}$ , and a decrease in shunt resistance, these effects were observed independently, i.e. a loss in  $V_{oc}$  was not accompanied with a loss of  $J_{sc}$  or a decrease in shunt resistance or vice versa. Conversely, through randomly cracking the cells we observe a loss in performance that is attributed to a decrease in all the cell parameters simultaneously. However, using this method of cell cracking the severity of performance loss is significantly different from sample to sample and is highly irreproducible due to the stochastic approach in introducing cracks.

### **Effects of Microcracks on MMC-Enhanced TJ Cell**

To evaluate the effects of cracks on performance of TJ cells we first crack four control samples. Control samples are TJ cells with bare Ag gridlines, i.e. no CNTs were embedded. We investigate two sets of controls; the first set consists of cells with Ag gridlines deposited through electron beam evaporation while the second set consists of cells with electrochemically deposited Ag gridlines. We expect different metal properties to be obtained (grain size, ductility, porosity, ...etc.) due to the different metal deposition methods. Hence, two controls are examined to clearly observe the effects of embedding CNTs on overall gridline electromechanical properties without the metal contribution. The *LIV* is performed for control samples before and after cracking. Cracks are generated by resting cells against a curved surface ( $r = 6$  cm) while applying an external mechanical stress on the cell's top surface. Fig. 78 summarizes the results of all four control samples.

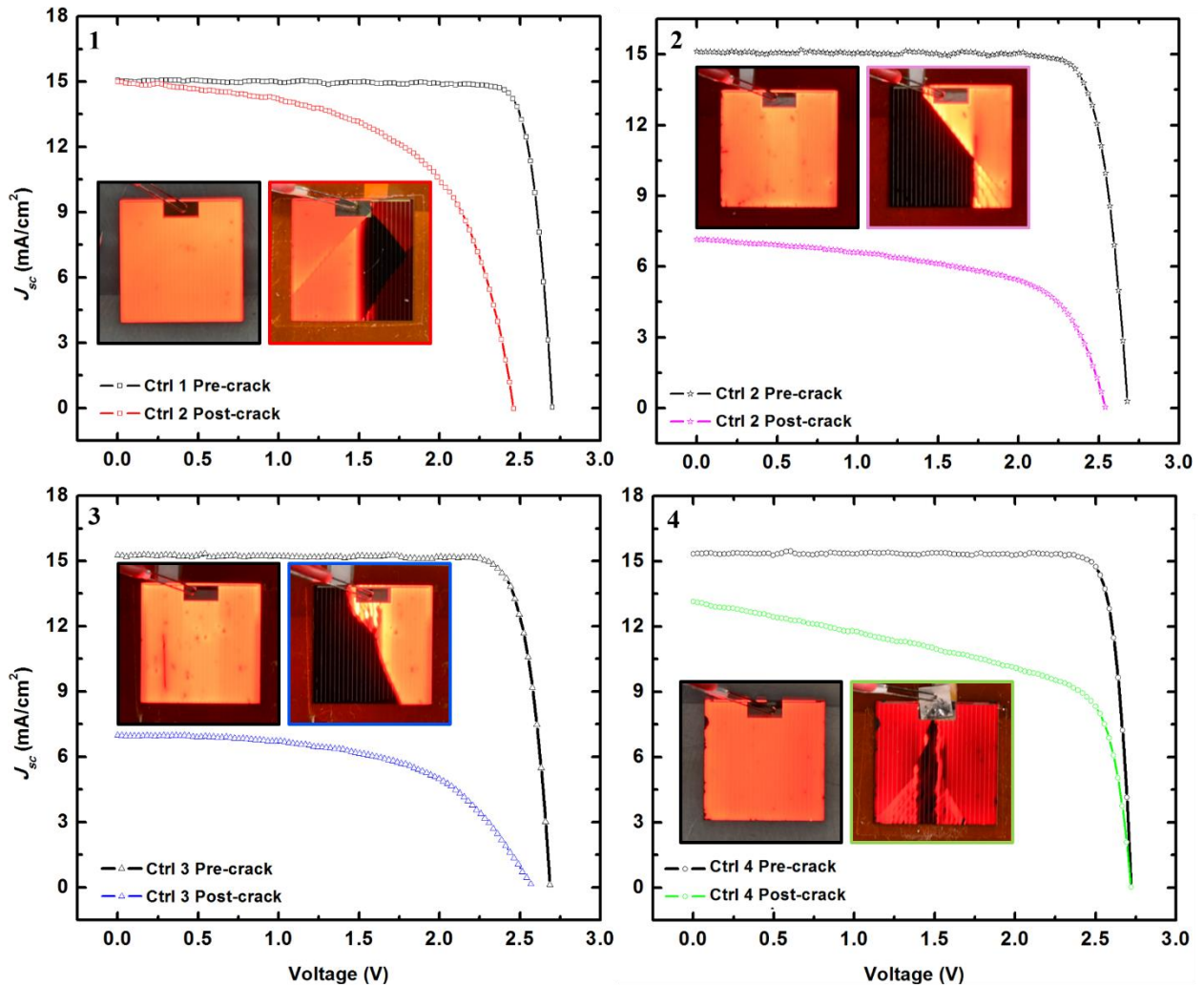


**Fig. 78.** *LIV* characteristics and electroluminescence response of TJ control samples pre- and post-cracking. Graphs (1) & (2) represent control samples with electron beam evaporated Ag gridlines. Graphs (3) & (4) represent control samples with electrochemically deposited Ag gridlines, Ref. [203].

Control samples 1 and 2 are evaporated Ag gridlines (Fig. 78, graphs 1 and 2) and samples 3 and 4 are electroplated Ag gridlines (Fig. 78, graphs 3 and 4). Examining first the EL response of all the cells, dark regions can be seen after introducing cracks. These regions indicate electrically isolated areas on the cell, in which cracks propagated through semiconductor material reaching metal gridlines and isolating portions of the cells from the busbar. The illuminated area from the EL response corresponds to the remaining active cell area that contributes to current generation in the *LIV* scans (Fig. 78). The open circuit voltage ( $V_{oc}$ ) in control sample 1 suffered the biggest impact while the short circuit current

density ( $J_{sc}$ ) remained unchanged after cracking. If the EL response is examined closely for control 1, it can be seen that the cracks did not fully propagate through the bus bar region, i.e. the dark regions seen are not truly dark rather having a faint EL response. That region may not have been properly captured due to the imaging equipment limitation. In control sample 4 (Fig. 78, graph 4) we notice the opposite case in which the  $J_{sc}$  was impacted the most while  $V_{oc}$  was unchanged. Control samples 2 and 3 (Fig. 78, graphs 2 and 3) we observe a similar cracking pattern and similar degradation in the performance in both cells, in which  $J_{sc}$  and  $V_{oc}$  are decreased. Table 4 summarizes the percentage change of control cells parameters ( $V_{oc}$ ,  $J_{sc}$ ,  $FF$ , and  $\eta$ ) pre- and post-cracking.

**Table 4**  
Summary Results of Percentage Change in Control TJ Cells

<i>Sample</i>	$\% \Delta V_{oc}$ (V)	$\% \Delta J_{sc}$ (mA/cm <sup>2</sup> )	$\% \Delta FF$ (%)	$\% \Delta \eta$ (%)
<i>Control 1</i>	9.1	2.6	34	43
<i>Control 2</i>	5.1	53	29	68
<i>Control 3</i>	4.4	54	34	65
<i>Control 4</i>	0.11	15	32	41

The discrepancy in the results arises due to the irreproducible/random method of introducing cracks on the cell. However, we can conclude that TJ cells with the bare Ag gridlines degrade significantly in performance due to cracks. The most pronounced impacts are seen in  $J_{sc}$  (54%) and  $V_{oc}$  (9.1%) of cells which in turn impacted the  $FF$  and  $\eta$  by up to 34% and 65%, respectively (Table 4).

In order to evaluate the role of CNTs in bridging cracks within the underlying semiconductor and remain electrically conducting, four TJ samples with MMC gridlines are prepared. The MMC gridlines are deposited in LBL microstructure with similar architectures. The cells are then fractured similarly to control samples while monitoring



the performance before and after mechanically stressing the cells. Fig. 79 summarizes the *LIV* and EL measurements of all four samples. The frequency of cracks generated from sample to sample is variable due to the nature of introducing the cracks on the cells, this can be seen in sample 3 (Fig. 79, graph 3 inset) vs. sample 4 (Fig. 79, graph 4 inset) where significantly more number of cracks are generated in the former sample.

Unlike the control samples, cells with MMC gridlines are capable of maintaining electrical connection even in the presence of cracks. Our samples with MMC gridlines are able to maintain a bright EL response without any visibly dark spot, which indicates that

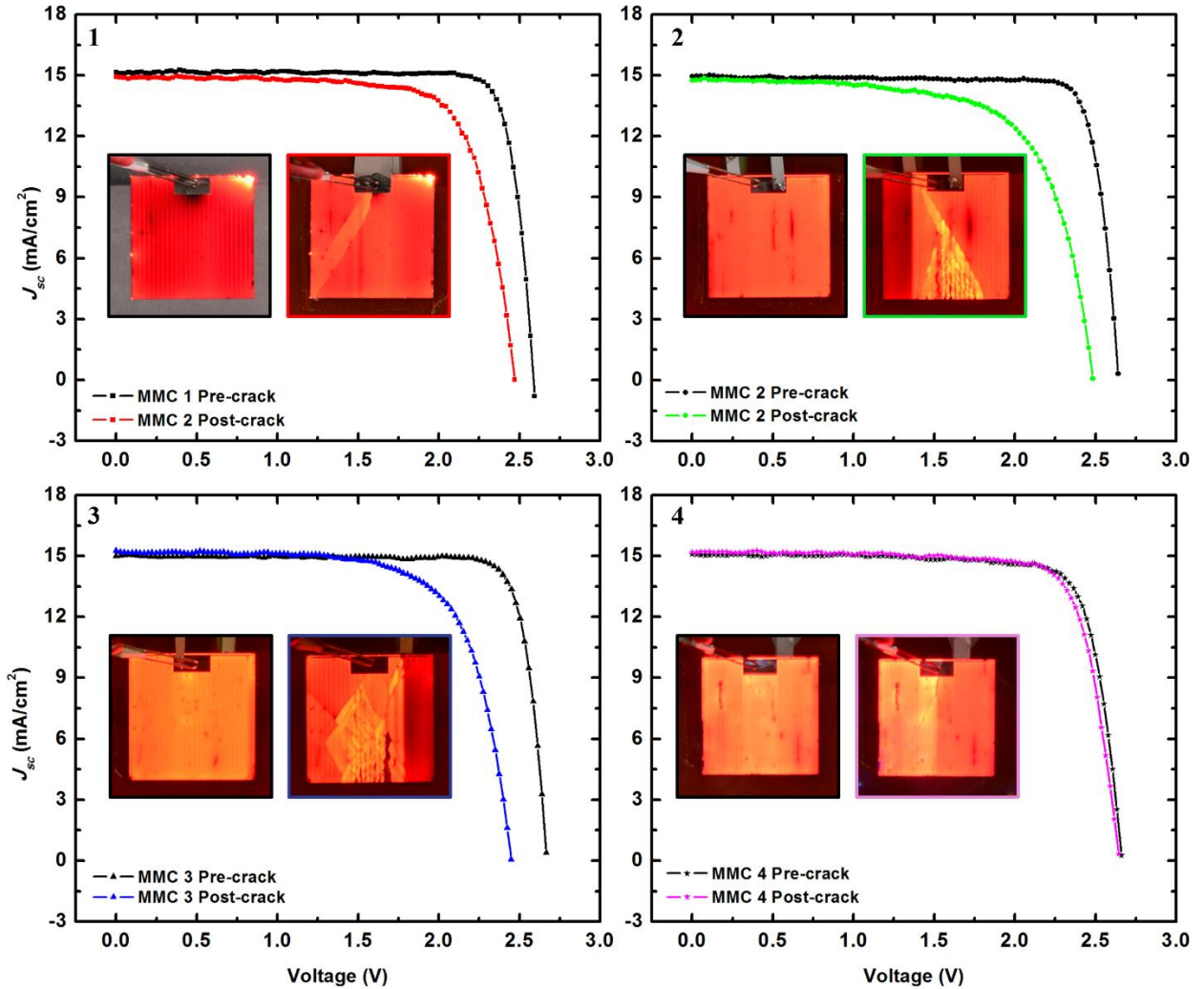


Fig. 79. LIV characteristics and electroluminescence response of TJ cell with MMC gridlines. Ref. [203].

electrical connection through the gridlines is not severed due to introducing cracks. At the fracture location, the EL intensity is brighter there and in the surrounding vicinity, while it is reduced farther away. The increased brightness indicates that more recombination sites for minority carriers are introduced at this location. A similar behavior is observed in [206], in which a bright region is observed in the top cell (GaInP) due to a microcrack that originated in the underlying subcell (GaInAs).

While the number of cracks generated may vary from sample to sample, unlike the control samples, the cells with MMC gridlines can maintain electrical continuity even in the presence of cracks. All test cells with MMC gridlines generate nearly the same  $J_{sc}$  after being fractured. As further evidence, our samples with MMC gridlines maintain a bright EL response with little to no visible dark spots. While both gridlines and substrate are completely fractured, the CNTs appear to provide a redundant electrical conduction pathway.

**Table 5**  
Summary Results of Percentage Change in MMC Cells

<i>Sample</i>	$\% \Delta V_{oc}$ (V)	$\% \Delta J_{sc}$ (mA/cm <sup>2</sup> )	$\% \Delta FF$ (%)	$\% \Delta \eta$ (%)
<i>MMC 1</i>	6.0	0.72	14	8
<i>MMC 2</i>	6.1	0.78	26	35
<i>MMC 3</i>	8.9	0.64	21	30
<i>MMC 4</i>	0.64	0.85	4.6	3.6

While  $J_{sc}$  remains virtually constant, we observe brighter EL intensity at and around the fracture location than the regions that remain intact. The increased brightness suggests an increased number of recombination sites for minority carriers at and around the fracture. A similar behavior is observed by Kong *et al.* [206], in which a bright region is observed

in the top cell (GaInP) due to a microcrack that originated from the underlying subcell (GaInAs). These recombination sites would reduce  $V_{oc}$ , which is clearly observed in Fig. 79 and listed in Table 5. As the number of cracks increases from Sample 1, to Sample 2, to Sample 3,  $V_{oc}$  decreases by 6.0, 6.1, and 8.9%, respectively.

For solar cells, the recombination rate at the edges is often much greater than elsewhere in the cell. At an edge, there is a complete disruption of the crystal lattice, which leads to an increase in the density of trap states inside the “forbidden gap.” These trap states subsequently increase the recombination rate [214]. Edge recombination has thus been found to significantly influence the efficiency of small-area, high efficiency solar cells [215]. As the number of cracks introduced increases, more edges are introduced within the cell, leading to a higher recombination rate and a greater loss in  $V_{oc}$ ,  $FF$ , and  $\eta$ .

Although  $J_{sc}$  is maintained, the series resistance of the MMC gridlines appears to increase after fracturing (see Fig. 79A – C). As the number of cracks increases, more gridlines get severed, where the electrical connection in that region is sustained only through the embedded CNTs. Thus, an increase in series resistance is closely correlated with the number of cracks introduced: i.e., a higher series resistance is observed in cells that are more fractured. The increase in the overall series resistance ultimately impacts the  $FF$ . With proper loading of CNTs within the composite and manipulation of the microstructure (e.g., multiple tiers of layer-by-layer architecture), we project that the series resistance can be reduced, improving the  $FF$ .

In comparison to control samples, the test cells integrated with our MMC gridlines are clearly more fracture tolerant. That is, embedding CNTs into a metal matrix mitigates the electrical disconnect due to microcracks. The continuous areal EL response and the

preservation of  $J_{sc}$  after substrate fracture are strong evidence that MMC lines are more resilient to microcracks developed in the semiconductor than bare metal gridlines. However, we acknowledge that the cracks may introduce other loss mechanisms that MMCs cannot fully counter, leading to an unavoidable loss in  $V_{oc}$ ,  $FF$ , and  $\eta$

## Conclusion

In the work presented here, we demonstrate the use of low-cost, multiwalled CNTs embedded in Ag matrix to mechanically and electrically reinforce metal gridlines used in multijunction photovoltaic cells. These composite metal gridlines show strong potential to replace conventional ones deposited by evaporation. Our metal matrix composites (MMCs) assume a layer-by-layer microstructure that consists of Ag/CNT/Ag, and we achieve this architecture, using simple deposition methods. Our process relies on electrochemical deposition (plating) of Ag, a low-cost, highly reproducible alternative to vacuum metal deposition. We also use spray-coating as a fast, cost-effective, and easily scalable method of depositing CNTs. The combined use of plating and spray-coating provides a manufacturable path to integrate MMCs.

We have successfully integrated MMCs onto commercially available TJ cells. For the purpose of demonstration and ease of integration, the dimensions of metal gridlines are made slightly larger than the state-of-practice design. Accounting for this minor deviation, we demonstrate excellent electrical properties comparable to cells with standard metallization:  $\eta$  and  $FF$  of 26% and 86%, respectively.

The most important outcome from this study is that MMC-enhanced cells are more crack-tolerant than control cells with standard metallization. Upon introducing cracks to

the cells, samples with the MMC gridlines exhibit virtually zero loss in  $J_{sc}$ , while retaining a continuous electroluminescence glow. The latter is strong evidence that the fractured portion of the substrate is electrically connected. In contrast, fractured control cells show a significant loss in  $J_{sc}$  up to 54% with noticeably dark regions during EL measurements. In addition, the average loss in  $FF$  and  $\eta$  in control cells is 32% and 54%, respectively, compared to 16% and 19% for MMC-enhanced cells. This demonstration supports that our MMC gridlines are suitable to replace traditional gridlines and to help mitigate the loss in cell performance as microcracks develop in cells.

## References

- [1] D. M. Chapin, C. S. Fuller, and G. L. Pearson, "A NEW SILICON P-N JUNCTION PHOTOCELL FOR CONVERTING SOLAR RADIATION INTO ELECTRICAL POWER," *Journal of Applied Physics*, vol. 25, pp. 676-677, 1954 1954.
- [2] T. Markvart, "RADIATION-DAMAGE IN SOLAR-CELLS," *Journal of Materials Science-Materials in Electronics*, vol. 1, pp. 1-12, May 1990.
- [3] J. R. Carter and H. Y. Tada, *Solar Cell Radiation Handbook: Jet Propulsion Laboratory*, 1973.
- [4] G. H. Kinchin and R. S. Pease, "THE DISPLACEMENT OF ATOMS IN SOLIDS BY RADIATION," *Reports on Progress in Physics*, vol. 18, pp. 1-51, 1955.
- [5] S. G. Bailey and D. J. Flood, "Space photovoltaics," *Progress in Photovoltaics*, vol. 6, pp. 1-14, Jan-Feb 1998.
- [6] C. G. Zimmermann, "Materials Challenges in Photovoltaic Energy Generation in Space," *Mrs Bulletin*, vol. 35, pp. 48-54, Jan 2010.
- [7] N. H. Karam, R. R. King, B. T. Cavicchi, D. D. Krut, J. H. Ermer, M. Haddad, *et al.*, "Development and characterization of high-efficiency Ga<sub>0.5</sub>In<sub>0.5</sub>P/GaAs/Ge dual- and triple-junction solar cells," *Ieee Transactions on Electron Devices*, vol. 46, pp. 2116-2125, Oct 1999.
- [8] A. Suzuki, M. Kaneiwa, T. Saga, and S. Matsuda, "Progress and future view of silicon space solar cells in Japan," *Ieee Transactions on Electron Devices*, vol. 46, pp. 2126-2132, Oct 1999.

- [9] *Solar Constant and Air Mass Zero Solar Spectral Irradiance Tables* vol. ASTM-E 490-73a. Philadelphia: American Society for Testing and Materials, 1992.
- [10] A. Goetzberger, J. Knobloch, and B. Voss, *Crystalline Silicon Solar Cells*. New York: Wiley, 1998.
- [11] M. A. Green, *Silicon Solar Cells: Advanced Principles and Practice*. Sidney: Bridge Printery, 1995.
- [12] W. Shockley and H. J. Queisser, "DETAILED BALANCE LIMIT OF EFFICIENCY OF P-N JUNCTION SOLAR CELLS," *Journal of Applied Physics*, vol. 32, pp. 510-&, 1961.
- [13] S. P. Bremner, M. Y. Levy, and C. B. Honsberg, "Analysis of tandem solar cell efficiencies under AM1.5G spectrum using a rapid flux calculation method," *Progress in Photovoltaics*, vol. 16, pp. 225-233, May 2008.
- [14] M. Yamaguchi and A. Luque, "High efficiency and high concentration in photovoltaics," *Ieee Transactions on Electron Devices*, vol. 46, pp. 2139-2144, Oct 1999.
- [15] T. Takamoto, M. Yamaguchi, S. J. Taylor, E. Ikeda, T. Agui, H. Kurita, *et al.*, "High-efficiency radiation-resistant InGaP/GaAs tandem solar cells," in *Conference Record of the Twenty Sixth Ieee Photovoltaic Specialists Conference - 1997*, ed New York: Ieee, 1997, pp. 887-890.
- [16] G. Timo, C. Flores, and R. Campesato, "Bottom cell growth aspects for triple junction InGaP/(In)GaAs/Ge solar cells," *Crystal Research and Technology*, vol. 40, pp. 1043-1047, Nov 2005.

- [17] M. Stan, D. Aiken, B. Cho, A. Cornfeld, J. Diaz, V. Ley, *et al.*, "Very high efficiency triple junction solar cells grown by MOVPE," *Journal of Crystal Growth*, vol. 310, pp. 5204-5208, Nov 2008.
- [18] M. Stan, D. Aiken, B. Cho, A. Cornfeld, J. Diaz, A. Korostyshevsky, *et al.*, "EVOLUTION OF THE HIGH EFFICIENCY TRIPLE JUNCTION SOLAR CELL FOR SPACE POWER," in *Pvsc: 2008 33rd Ieee Photovoltaic Specialists Conference, Vols 1-4*, ed New York: Ieee, 2008, pp. 1450-1455.
- [19] J. F. Geisz, S. Kurtz, M. W. Wanlass, J. S. Ward, A. Duda, D. J. Friedman, *et al.*, "High-efficiency GaInP/GaAs/InGaAs triple-junction solar cells grown inverted with a metamorphic bottom junction," *Applied Physics Letters*, vol. 91, p. 023502, 2007.
- [20] A. B. Cornfeld, M. Stan, T. Varghese, J. Diaz, A. V. Ley, B. Cho, *et al.*, "DEVELOPMENT OF A LARGE AREA INVERTED METAMORPHIC MULTI-JUNCTION (IMM) HIGHLY EFFICIENT AM0 SOLAR CELL," in *Pvsc: 2008 33rd Ieee Photovoltaic Specialists Conference, Vols 1-4*, ed New York: Ieee, 2008, pp. 88-92.
- [21] A. B. Cornfeld, D. Aiken, B. Cho, A. V. Ley, P. Sharps, M. Stan, *et al.*, "DEVELOPMENT OF A FOUR SUB-CELL INVERTED METAMORPHIC MULTI-JUNCTION (IMM) HIGHLY EFFICIENT AM0 SOLAR CELL," in *35th Ieee Photovoltaic Specialists Conference*, ed, 2010, pp. 105-109.
- [22] M. W. Wanlass, S. P. Ahrenkiel, R. K. Ahrenkiel, D. S. Albin, J. J. Carapella, A. Duda, *et al.*, "Lattice-mismatched approaches for high-performance, III-V



- photovoltaic energy converters," in *Conference Record of the Thirty-First IEEE Photovoltaic Specialists Conference - 2005*, ed New York: Ieee, 2005, pp. 530-535.
- [23] P. Patel, D. Aiken, A. Boca, B. Cho, D. Chumney, M. B. Clevenger, *et al.*, "Experimental Results From Performance Improvement and Radiation Hardening of Inverted Metamorphic Multijunction Solar Cells," *Ieee Journal of Photovoltaics*, vol. 2, pp. 377-381, Jul 2012.
- [24] N. Dharmarasu, M. Yamaguchi, A. Khan, T. Yamada, T. Tanabe, S. Takagishi, *et al.*, "High-radiation-resistant InGaP, InGaAsP, and InGaAs solar cells for multijunction solar cells," *Applied Physics Letters*, vol. 79, pp. 2399-2401, Oct 2001.
- [25] J. Boisvert, D. Law, R. King, E. Rehder, P. Chiu, D. Bhusari, *et al.*, "High Efficiency Inverted Metamorphic (IMM) Solar Cells," in *2013 Ieee 39th Photovoltaic Specialists Conference*, ed, 2013, pp. 2790-2792.
- [26] M. Demant, T. Welschehold, M. Oswald, S. Bartsch, T. Brox, S. Schoenfelder, *et al.*, "Microcracks in Silicon Wafers I: Inline Detection and Implications of Crack Morphology on Wafer Strength," *Ieee Journal of Photovoltaics*, vol. 6, pp. 126-135, Jan 2016.
- [27] M. Demant, T. Welschehold, S. Kluska, and S. Rein, "Microcracks in Silicon Wafers II: Implications on Solar Cell Characteristics, Statistics and Physical Origin," *Ieee Journal of Photovoltaics*, vol. 6, pp. 136-144, Jan 2016.
- [28] M. Kontges, I. Kunze, S. Kajari-Schroder, X. Breitenmoser, and B. Bjorneklett, "The risk of power loss in crystalline silicon based photovoltaic modules due to micro-cracks," *Solar Energy Materials and Solar Cells*, vol. 95, pp. 1131-1137, Apr 2011.

- [29] A. Dolara, S. Leva, G. Manzolini, and E. Ogliari, "Investigation on Performance Decay on Photovoltaic Modules: Snail Trails and Cell Microcracks," *Ieee Journal of Photovoltaics*, vol. 4, pp. 1204-1211, Sep 2014.
- [30] J. Kasewieter, F. Haase, M. H. Larrode, and M. Kontges, "Cracks in solar cell metallization leading to module power loss under mechanical loads," in *Proceedings of the 4th International Conference on Crystalline Silicon Photovoltaics*. vol. 55, A. Weeber, A. Aberle, R. Brendel, A. Cuevas, S. Glunz, G. Hahn, *et al.*, Eds., ed, 2014, pp. 469-477.
- [31] I. Berardone, M. Corrado, and M. Paggi, "A generalized electric model for mono and polycrystalline silicon in the presence of cracks and random defects," in *Proceedings of the 4th International Conference on Crystalline Silicon Photovoltaics*. vol. 55, A. Weeber, A. Aberle, R. Brendel, A. Cuevas, S. Glunz, G. Hahn, *et al.*, Eds., ed, 2014, pp. 22-29.
- [32] J. Kasewieter, F. Haase, and M. Kontges, "Model of Cracked Solar Cell Metallization Leading to Permanent Module Power Loss," *Ieee Journal of Photovoltaics*, vol. 6, pp. 28-33, Jan 2016.
- [33] A. Morlier, F. Haase, M. Kontges, and Ieee, "Impact of cracks in multicrystalline silicon solar cells on PV module power - A simulation study based on field data," in *2015 Ieee 42nd Photovoltaic Specialist Conference*, ed, 2015.
- [34] S. Spataru, P. Hacke, D. Sera, S. Glick, T. Kerekes, R. Teodorescu, *et al.*, "Quantifying Solar Cell Cracks in Photovoltaic Modules by Electroluminescence Imaging," in *2015 Ieee 42nd Photovoltaic Specialist Conference*, ed, 2015.

- [35] S. Kajari-Schroeder, I. Kunze, U. Eitner, and M. Koentges, "Spatial and orientational distribution of cracks in crystalline photovoltaic modules generated by mechanical load tests," *Solar Energy Materials and Solar Cells*, vol. 95, pp. 3054-3059, Nov 2011.
- [36] J. T. H. Tsai and H. L. Hwang, "Carbon Nanotube Reinforced Conductors for Flexible Electronics," *Journal of Display Technology*, vol. 5, pp. 232-235, Apr-Jun 2009.
- [37] S. Iijima, "HELICAL MICROTUBULES OF GRAPHITIC CARBON," *Nature*, vol. 354, pp. 56-58, Nov 1991.
- [38] E. T. Thostenson, Z. F. Ren, and T. W. Chou, "Advances in the science and technology of carbon nanotubes and their composites: a review," *Composites Science and Technology*, vol. 61, pp. 1899-1912, 2001.
- [39] H. J. Dai, "Carbon nanotubes: Synthesis, integration, and properties," *Accounts of Chemical Research*, vol. 35, pp. 1035-1044, Dec 2002.
- [40] M. S. Dresselhaus, G. Dresselhaus, and P. C. Eklund, *Science of fullerenes and carbon nanotubes*. New York: Academic Press, 1996.
- [41] R. Saito, M. S. Dresselhaus, and G. Dresselhaus, *Physical properties of carbon nanotubes*. London: Imperial College Press, 1998.
- [42] H. Kataura, Y. Kumazawa, Y. Maniwa, I. Umezu, S. Suzuki, Y. Ohtsuka, *et al.*, "Optical properties of single-wall carbon nanotubes," *Synthetic Metals*, vol. 103, pp. 2555-2558, Jun 1999.
- [43] O. Jost, A. A. Gorbunov, W. Pompe, T. Pichler, R. Friedlein, M. Knupfer, *et al.*, "Diameter grouping in bulk samples of single-walled carbon nanotubes from

- optical absorption spectroscopy," *Applied Physics Letters*, vol. 75, pp. 2217-2219, Oct 1999.
- [44] L. Kavan, P. Raptá, L. Dunsch, M. J. Bronikowski, P. Willis, and R. E. Smalley, "Electrochemical tuning of electronic structure of single-walled carbon nanotubes: In-situ Raman and vis-NIR study," *Journal of Physical Chemistry B*, vol. 105, pp. 10764-10771, Nov 2001.
- [45] N. Minami, S. Kazaoui, R. Jacquemin, H. Yamawaki, K. Aoki, H. Kataura, *et al.*, "Optical properties of semiconducting and metallic single wall carbon nanotubes: effects of doping and high pressure," *Synthetic Metals*, vol. 116, pp. 405-409, Jan 2001.
- [46] F. Hennrich, S. Lebedkin, S. Malik, and M. M. Kappes, "Free-standing single-wall carbon nanotube thin films," in *Structural and Electronic Properties of Molecular Nanostructures*. vol. 633, H. Kuzmany, J. Fink, M. Mehring, and S. Roth, Eds., ed Melville: Amer Inst Physics, 2002, pp. 619-623.
- [47] L. Hu, D. S. Hecht, and G. Gruner, "Percolation in transparent and conducting carbon nanotube networks," *Nano Letters*, vol. 4, pp. 2513-2517, Dec 2004.
- [48] N. Kouklin, M. Tzolov, D. Straus, A. Yin, and J. M. Xu, "Infrared absorption properties of carbon nanotubes synthesized by chemical vapor deposition," *Applied Physics Letters*, vol. 85, pp. 4463-4465, Nov 2004.
- [49] M. Kaempgen, G. S. Duesberg, and S. Roth, "Transparent carbon nanotube coatings," *Applied Surface Science*, vol. 252, pp. 425-429, Oct 2005.
- [50] A. Hirsch, "Functionalization of single-walled carbon nanotubes," *Angewandte Chemie-International Edition*, vol. 41, pp. 1853-1859, 2002.

- [51] P. J. de Pablo, C. Gomez-Navarro, M. T. Martinez, A. M. Benito, W. K. Maser, J. Colchero, *et al.*, "Performing current versus voltage measurements of single-walled carbon nanotubes using scanning force microscopy," *Applied Physics Letters*, vol. 80, pp. 1462-1464, Feb 2002.
- [52] E. D. Minot, Y. Yaish, V. Sazonova, J. Y. Park, M. Brink, and P. L. McEuen, "Tuning carbon nanotube band gaps with strain," *Physical Review Letters*, vol. 90, p. 4, Apr 2003.
- [53] E. S. Snow, J. P. Novak, M. D. Lay, E. H. Houser, F. K. Perkins, and P. M. Campbell, "Carbon nanotube networks: Nanomaterial for macroelectronic applications," *Journal of Vacuum Science & Technology B*, vol. 22, pp. 1990-1994, Jul-Aug 2004.
- [54] M. D. Lay, J. P. Novak, and E. S. Snow, "Simple route to large-scale ordered arrays of liquid-deposited carbon nanotubes," *Nano Letters*, vol. 4, pp. 603-606, Apr 2004.
- [55] M. Shiraishi, T. Takenobu, T. Iwai, Y. Iwasa, H. Kataura, and M. Ata, "Single-walled carbon nanotube aggregates for solution-processed field effect transistors," *Chemical Physics Letters*, vol. 394, pp. 110-113, Aug 2004.
- [56] M. A. Meitl, Y. X. Zhou, A. Gaur, S. Jeon, M. L. Usrey, M. S. Strano, *et al.*, "Solution casting and transfer printing single-walled carbon nanotube films," *Nano Letters*, vol. 4, pp. 1643-1647, Sep 2004.
- [57] Y. X. Zhou, A. Gaur, S. H. Hur, C. Kocabas, M. A. Meitl, M. Shim, *et al.*, "p-channel, n-channel thin film transistors and p-n diodes based on single wall carbon nanotube networks," *Nano Letters*, vol. 4, pp. 2031-2035, Oct 2004.

- [58] Z. L. Li, P. Dharap, S. Nagarajaiah, E. V. Barrera, and J. D. Kim, "Carbon nanotube film sensors," *Advanced Materials*, vol. 16, pp. 640+, Apr 2004.
- [59] J. K. Abraham, B. Philip, A. Witchurch, V. K. Varadan, and C. C. Reddy, "A compact wireless gas sensor using a carbon nanotube/PMMA thin film chemiresistor," *Smart Materials & Structures*, vol. 13, pp. 1045-1049, Oct 2004.
- [60] M. Penza, F. Antolini, and M. V. Antisari, "Carbon nanotubes as SAW chemical sensors materials," *Sensors and Actuators B-Chemical*, vol. 100, pp. 47-59, Jun 2004.
- [61] N. Ferrer-Anglada, V. Gomis, Z. Ei-Hachemi, U. D. Weglikovska, M. Kaempgen, and S. Roth, "Carbon nanotube based composites for electronic applications: CNT-conducting polymers, CNT-Cu," *Physica Status Solidi a-Applications and Materials Science*, vol. 203, pp. 1082-1087, May 2006.
- [62] S. Zhang, D. Sun, Y. Q. Fu, and H. J. Du, "Toughening of hard nanostructural thin films: a critical review," *Surface & Coatings Technology*, vol. 198, pp. 2-8, Aug 2005.
- [63] Z. H. Xia, W. A. Curtin, and B. W. Sheldon, "A new method to evaluate the fracture toughness of thin films," *Acta Materialia*, vol. 52, pp. 3507-3517, Jul 2004.
- [64] Y. Feng, H. L. Yuan, and M. Zhang, "Fabrication and properties of silver-matrix composites reinforced by carbon nanotubes," *Materials Characterization*, vol. 55, pp. 211-218, Sep 2005.
- [65] W. M. Daoush, B. K. Lim, C. B. Mo, D. H. Nam, and S. H. Hong, "Electrical and mechanical properties of carbon nanotube reinforced copper nanocomposites fabricated by electroless deposition process," *Materials Science and Engineering*

- a-Structural Materials Properties Microstructure and Processing*, vol. 513-14, pp. 247-253, Jul 2009.
- [66] A. Milchev, E. Vassileva, and V. Kertov, "ELECTROLYTIC NUCLEATION OF SILVER ON A GLASSY-CARBON ELECTRODE .1. MECHANISM OF CRITICAL NUCLEUS FORMATION," *Journal of Electroanalytical Chemistry*, vol. 107, pp. 323-336, 1980.
- [67] A. Serruya, B. R. Scharifker, I. Gonzalez, M. T. Oropeza, and M. PalomarPardave, "Silver electrocrystallization from a nonpolluting aqueous leaching solution containing ammonia and chloride," *Journal of Applied Electrochemistry*, vol. 26, pp. 451-457, Apr 1996.
- [68] I. Sondi and B. Salopek-Sondi, "Silver nanoparticles as antimicrobial agent: a case study on E-coli as a model for Gram-negative bacteria," *Journal of Colloid and Interface Science*, vol. 275, pp. 177-182, Jul 2004.
- [69] M. Rai, A. Yadav, and A. Gade, "Silver nanoparticles as a new generation of antimicrobials," *Biotechnology Advances*, vol. 27, pp. 76-83, Jan-Feb 2009.
- [70] E. A. Araujo, N. J. Andrade, L. H. M. da Silva, P. C. Bernardes, A. Teixeira, J. P. N. de Sa, *et al.*, "Antimicrobial Effects of Silver Nanoparticles against Bacterial Cells Adhered to Stainless Steel Surfaces," *Journal of Food Protection*, vol. 75, pp. 701-705, Apr 2012.
- [71] K. Roy, C. K. Sarkar, and C. K. Ghosh, "GREEN SYNTHESIS OF SILVER NANOPARTICLES USING FRUIT EXTRACT OF MALUS DOMESTICA AND STUDY OF ITS ANTIMICROBIAL ACTIVITY," *Digest Journal of Nanomaterials and Biostructures*, vol. 9, pp. 1137-1146, Jul-Sep 2014.

- [72] T. E. Graedel, "CORROSION MECHANISMS FOR SILVER EXPOSED TO THE ATMOSPHERE," *Journal of the Electrochemical Society*, vol. 139, pp. 1963-1970, Jul 1992.
- [73] A. K. Sikder, D. S. Misra, D. Singhbal, and S. Chakravorty, "Surface engineering of metal-diamond composite coatings on steel substrates using chemical vapour deposition and electroplating routes," *Surface & Coatings Technology*, vol. 114, pp. 230-234, May 1999.
- [74] S. T. Aruna, S. Diwakar, A. Jain, and K. S. Rajam, "Comparative study on the effect of current density on Ni and Ni-Al<sub>2</sub>O<sub>3</sub> nanocomposite coatings produced by electrolytic deposition," *Surface Engineering*, vol. 21, pp. 209-214, Jun 2005.
- [75] R. D. Xu, J. L. Wang, L. F. He, and Z. C. Guo, "Study on the characteristics of Ni-W-P composite coatings containing nano-SiO<sub>2</sub> and nano-CeO<sub>2</sub> particles," *Surface & Coatings Technology*, vol. 202, pp. 1574-1579, Jan 2008.
- [76] M. R. Vaezi, S. K. Sadrnezhad, and L. Nikzad, "Electrodeposition of Ni-SiC nanocomposite coatings and evaluation of wear and corrosion resistance and electroplating characteristics," *Colloids and Surfaces a-Physicochemical and Engineering Aspects*, vol. 315, pp. 176-182, Feb 2008.
- [77] *Electrolysis*. Available: <http://cnx.org/contents/BbtUNmjT@3/Electrolysis>
- [78] M. Schlesinger, *Modern Electroplating*, 4 ed. New York: Wiley: Electrochemical Society Series, 2000.
- [79] A. K. Graham and H. L. Pinkerton, *Electroplating Engineering Handbook*, 2 ed. New York Reinhold Pub. Corp., 1962.



- [80] Q. Y. Feng, T. J. Li, Z. T. Zhang, J. Zhang, M. Liu, and J. Z. Jin, "Preparation of nanostructured Ni/Al<sub>2</sub>O<sub>3</sub> composite coatings in high magnetic field," *Surface & Coatings Technology*, vol. 201, pp. 6247-6252, Apr 2007.
- [81] H. Li, Y. Z. Wan, H. Liang, X. L. Li, Y. Huang, and F. He, "Composite electroplating of Cu-SiO<sub>2</sub> nano particles on carbon fiber reinforced epoxy composites," *Applied Surface Science*, vol. 256, pp. 1614-1616, Dec 2009.
- [82] G. Elkington and H. Elkington, British Patent 8447, 1840.
- [83] B. M. Luce and G. Foulke, *Modern Electroplating*. New York: J. Wiley & Sons, 1974.
- [84] M. Ernes, German Patent 950,230, 1956.
- [85] T. Hata and T. Hanada, U.S. Patent 3,337,350, 1967.
- [86] D. J. Hood, U.S. Patent 2,120,203, 1938.
- [87] S. Horst, German Patent 2,063,334, 1972.
- [88] Y. Mori, Japan Patent 7,606,135, 1976.
- [89] T. Mukaiyama, Japan Patent 7,216,819, 1972.
- [90] S. Noguchi, Japan Patent 7,593,234, 1975.
- [91] S. Werner, German Patent 2,639,287, 1978.
- [92] I. Krastev, A. Zielonka, S. Nakabayashi, and K. Inokuma, "A cyclic voltammetric study of ferrocyanide-thiocyanate silver electrodeposition electrolyte," *Journal of Applied Electrochemistry*, vol. 31, pp. 1041-1047, Sep 2001.
- [93] J. Amblard, M. Froment, C. Georgoulis, and G. Papanastasiou, "ROLE OF TARTARIC ACID AND TARTRATES IN INHIBITION OF DENDRITIC

- GROWTH OF SILVER ELECTRODEPOSITED FROM AQUEOUS NITRATE SOLUTION," *Surface Technology*, vol. 6, pp. 409-423, 1978.
- [94] M. Froment, G. Maurin, Vereecke.J, and R. Wiart, "INFLUENCE OF DOUBLE SODIUM AND POTASSIUM TARTRATE ON GROWTH OF ELECTROLYTIC SILVER DEPOSITS OBTAINED FROM AN AQUEOUS NITRATE SOLUTION," *Comptes Rendus Hebdomadaires Des Seances De L Academie Des Sciences Serie C*, vol. 271, pp. 253-&, 1970.
- [95] J. Vereecken and R. Winand, "INFLUENCE OF INHIBITORS ON STRUCTURE OF SILVER DEPOSITS OBTAINED BY ELECTROLYSIS OF AQUEOUS NITRATE SOLUTIONS," *Journal of the Electrochemical Society*, vol. 123, pp. 643-646, 1976.
- [96] G. Papanastasiou, D. Jannakoudakis, J. Amblard, and M. Froment, "INFLUENCE OF TARTARIC ACID ON THE ELECTRODEPOSITION OF SILVER FROM AQUEOUS AGNO<sub>3</sub> SOLUTIONS," *Journal of Applied Electrochemistry*, vol. 15, pp. 71-76, 1985.
- [97] G. M. Zarkadas, A. Stergiou, and G. Papanastasiou, "Influence of tartaric acid on the electrodeposition of silver from binary water plus dioxane AgNO<sub>3</sub> solutions," *Journal of Applied Electrochemistry*, vol. 31, pp. 1251-1259, 2001.
- [98] G. M. Zarkadas, A. Stergiou, and G. Papanastasiou, "Silver electrodeposition from AgNO<sub>3</sub> solutions containing organic additives: Electrodeposition from binary water-methanol solvent systems in the presence of tartaric acid," *Journal of Applied Electrochemistry*, vol. 34, pp. 607-615, Jun 2004.

- [99] G. M. Zarkadas, A. Stergiou, and G. Papanastasiou, "Influence of citric acid on the silver electrodeposition from aqueous AgNO<sub>3</sub> solutions," *Electrochimica Acta*, vol. 50, pp. 5022-5031, Sep 2005.
- [100] G. Fuseya and K. Murata, *Transactions of the American Electrochemical Society L(1)*, p. 235, 1926.
- [101] F. C. Mathers and J. R. Kuebler, *Transactions of the American Electrochemical Society*, vol. 29, p. 417, 1916.
- [102] E. Chassaing, K. V. Quang, and R. Wiart, "KINETICS OF COPPER ELECTRODEPOSITION IN CITRATE ELECTROLYTES," *Journal of Applied Electrochemistry*, vol. 16, pp. 591-604, Jul 1986.
- [103] S. Cattarin, F. Furlanetto, M. M. Musiani, and P. Guerriero, "EFFECT OF COMPLEXING AGENT (CITRIC-ACID) AND PH ON THE CATHODIC DEPOSITION OF AS-SB ALLOYS," *Journal of Applied Electrochemistry*, vol. 24, pp. 439-448, May 1994.
- [104] V. C. Kieling, "Parameters influencing the electrodeposition of Ni-Fe alloys," *Surface & Coatings Technology*, vol. 96, pp. 135-139, Nov 1997.
- [105] T. Yamasaki, P. Schlossmacher, K. Ehrlich, and Y. Ogino, "Formation of amorphous electrodeposited Ni-W alloys and their nanocrystallization," *Nanostructured Materials*, vol. 10, pp. 375-388, Apr 1998.
- [106] S. S. Abd El Rehim, E. E. Fouad, S. M. Abd El Wahaab, and H. H. Hassan, "Electrodeposition of Zn-Ni-Cd ternary alloys from acetate bath," *Indian Journal of Chemical Technology*, vol. 5, pp. 387-392, Nov 1998.

- [107] J. Doesburg and D. G. Ivey, "Microstructure and preferred orientation of Au-Sn alloy plated deposits," *Materials Science and Engineering B-Solid State Materials for Advanced Technology*, vol. 78, pp. 44-52, Oct 2000.
- [108] D. Golodnitsky, N. V. Gudin, and G. A. Volyanuk, "Study of nickel-cobalt alloy electrodeposition from a sulfamate electrolyte with different anion additives," *Journal of the Electrochemical Society*, vol. 147, pp. 4156-4163, Nov 2000.
- [109] J. Gong and E. J. Podlaha, "Electrodeposition of Fe-Tb alloys from an aqueous electrolyte," *Electrochemical and Solid State Letters*, vol. 3, pp. 422-425, Sep 2000.
- [110] D. Golodnitsky, Y. Rosenberg, and A. Ulus, "The role of anion additives in the electrodeposition of nickel-cobalt alloys from sulfamate electrolyte," *Electrochimica Acta*, vol. 47, pp. 2707-2714, Jul 2002.
- [111] O. Younes and E. Gileadi, "Electroplating of high tungsten content Ni/W alloys," *Electrochemical and Solid State Letters*, vol. 3, pp. 543-545, Dec 2000.
- [112] M. D. Obradovic, R. M. Stevanovic, and A. R. Despic, "Electrochemical deposition of Ni-W alloys from ammonia-citrate electrolyte," *Journal of Electroanalytical Chemistry*, vol. 552, pp. 185-196, Jul 2003.
- [113] S. Rode, C. Henninot, C. C. Vallieres, and M. Matlosz, "Complexation chemistry in copper plating from citrate baths," *Journal of the Electrochemical Society*, vol. 151, pp. C405-C411, 2004.
- [114] O. Younes, L. Zhu, Y. Rosenberg, Y. Shacham-Diamand, and E. Gileadi, "Electroplating of amorphous thin films of tungsten/nickel alloys," *Langmuir*, vol. 17, pp. 8270-8275, Dec 2001.

- [115] E. Gomez, A. Llorente, and E. Valles, "Obtention and characterisation of cobalt plus copper electrodeposits from a citrate bath," *Journal of Electroanalytical Chemistry*, vol. 495, pp. 19-26, Dec 2000.
- [116] *E-Brite 50/50 RTP Alkaline Non-Cyanide Silver Process Produces a Finer Grain Structure than Cyanide Silver*. Available: <http://epi.com/user/files/E-Brite-50-50-Sell-Sheet.pdf>
- [117] *A New Alkaline CN-Free Process for Electronic, Industrial & Decorative Plating Applications*. Available: <http://epi.com/user/files/NewAlkalinecyanide-freeSilverPlating%281%29.pdf>
- [118] C. H. Hamann, A. Hamnett, and W. Vielstich, *Electrochemistry*, 2 ed. Germany, 2007.
- [119] H. N. Wang and L. Pilon, "Accurate Simulations of Electric Double Layer Capacitance of Ultramicroelectrodes," *Journal of Physical Chemistry C*, vol. 115, pp. 16711-16719, Aug 2011.
- [120] H. Helmholtz, "Ueber einige Gesetze der Vertheilung elektrischer Ströme in körperlichen Leitern mit Anwendung auf die thierisch-elektrischen Versuche," *Annalen der Physik*, vol. 165, pp. 211-233, 1853.
- [121] G. Gouy, *Journal De Physique*, vol. 9, p. 475, 1910.
- [122] D. L. Chapman, *Philosophical Magazine*, vol. 25, p. 475, 1913.
- [123] O. Z. Stern, *Electrochemistry* vol. 30, 1924.
- [124] X. Zhao, B. M. Sanchez, P. J. Dobson, and P. S. Grant, "The role of nanomaterials in redox-based supercapacitors for next generation energy storage devices," *Nanoscale*, vol. 3, pp. 839-855, 2011.

- [125] O. K. Abudayyeh, N. D. Gapp, C. Nelson, D. M. Wilt, and S. M. Han, "Silver-Carbon-Nanotube Metal Matrix Composites for Metal Contacts on Space Photovoltaic Cells," *Ieee Journal of Photovoltaics*, vol. 6, pp. 337-342, Jan 2016.
- [126] O. K. Abudayyeh, C. Nelson, S. M. Han, N. Gapp, D. M. Wilt, and Ieee, "Silver-Carbon-Nanotube Metal Matrix Composites for Metal Contacts on Space Photovoltaic Cells," in *2015 Ieee 42nd Photovoltaic Specialist Conference*, ed New York: Ieee, 2015.
- [127] J. X. Fang, H. Hahn, R. Krupke, F. Schramm, T. Scherer, B. J. Ding, *et al.*, "Silver nanowires growth via branch fragmentation of electrochemically grown silver dendrites," *Chemical Communications*, pp. 1130-1132, 2009.
- [128] I. S. Yasnikov, Y. D. Gamburg, and P. E. Prokhorov, "Peculiarities of morphology of silver microcrystals electroplated under potentiostatic conditions from ammonium solutions," *Russian Journal of Electrochemistry*, vol. 46, pp. 524-529, May 2010.
- [129] Y. H. Cheng and S. Y. Cheng, "Nanostructures formed by Ag nanowires," *Nanotechnology*, vol. 15, pp. 171-175, Jan 2004.
- [130] H. Takata, K. Okada, T. Koga, and H. Hirabayashi, "RELATION BETWEEN PREFERRED ORIENTATION AND YOUNGS MODULUS OF ELECTROPLATED NICKEL," *Journal of the Japan Institute of Metals*, vol. 55, pp. 1368-1374, Dec 1991.
- [131] Y. S. Won, D. Cho, Y. Kim, J. Lee, and S. S. Park, "Degradation of Poly(ethylene glycol) by Electrolysis During the Cu Electroplating: A Combined Experimental

- and Density Functional Theory Study," *Journal of Applied Polymer Science*, vol. 117, pp. 2083-2089, Aug 2010.
- [132] H. Tsuge, K. Tozawa, Y. Muguruma, M. Kawabe, M. Abe, and M. Sagiya, "Effect of gas holdup on current density distribution in horizontal electrolysis cell (vol 81, pg 707, 2003)," *Canadian Journal of Chemical Engineering*, vol. 81, pp. 1257-1257, Dec 2003.
- [133] *Electrolysis of Water*. Available: [https://en.wikipedia.org/wiki/Electrolysis\\_of\\_water](https://en.wikipedia.org/wiki/Electrolysis_of_water)
- [134] W. Ruythooren, K. Attenborough, S. Beerten, P. Merken, J. Fransaer, E. Beyne, *et al.*, "Electrodeposition for the synthesis of microsystems," *Journal of Micromechanics and Microengineering*, vol. 10, pp. 101-107, Jun 2000.
- [135] L. J. Gao, P. Ma, K. M. Novogradez, and P. R. Norton, "Characterization of permalloy thin films electrodeposited on Si(111) surfaces," *Journal of Applied Physics*, vol. 81, pp. 7595-7599, Jun 1997.
- [136] K. Attenborough, H. Boeve, J. De Boeck, G. Borghs, and J. P. Celis, "Electrodeposited spin valves on n-type GaAs," *Applied Physics Letters*, vol. 74, pp. 2206-2208, Apr 1999.
- [137] M. Cerisier, K. Attenborough, J. Fransaer, C. Van Haesendonck, and J. P. Celis, "Growth mode of copper films electrodeposited on silicon from sulfate and pyrophosphate solutions," *Journal of the Electrochemical Society*, vol. 146, pp. 2156-2162, Jun 1999.

- [138] P. C. Andricacos, C. Uzoh, J. O. Dukovic, J. Horkans, and H. Deligianni, *Damascene copper electroplating for chip interconnections* vol. 98. Pennington: Electrochemical Society Inc, 1999.
- [139] R. H. Baughman, A. A. Zakhidov, and W. A. de Heer, "Carbon Nanotubes--the Route Toward Applications," *Science*, vol. 297, pp. 787-792, 2002-08-02 00:00:00 2002.
- [140] P. M. Ajayan and O. Z. Zhou, *Carbon Nanotubes* vol. 80. Berlin: Springer-Verlag, 2001.
- [141] O. Breuer and U. Sundararaj, "Big returns from small fibers: A review of polymer/carbon nanotube composites," *Polymer Composites*, vol. 25, pp. 630-645, Dec 2004.
- [142] C. N. R. Rao, B. C. Satishkumar, A. Govindaraj, and M. Nath, "Nanotubes," *Chemphyschem*, vol. 2, pp. 78-105, Feb 2001.
- [143] M. F. L. De Volder, S. H. Tawfick, R. H. Baughman, and A. J. Hart, "Carbon Nanotubes: Present and Future Commercial Applications," *Science*, vol. 339, pp. 535-539, 2013-02-01 00:00:00 2013.
- [144] J. K. Holt, H. G. Park, Y. Wang, M. Stadermann, A. B. Artyukhin, C. P. Grigoropoulos, *et al.*, "Fast Mass Transport Through Sub-2-Nanometer Carbon Nanotubes," *Science*, vol. 312, pp. 1034-1037, 2006-05-19 00:00:00 2006.
- [145] R. Smajda, Á. Kukovecz, Z. Kónya, and I. Kiricsi, "Structure and gas permeability of multi-wall carbon nanotube buckypapers," *Carbon*, vol. 45, pp. 1176-1184, 5// 2007.



- [146] A. A. Mamedov, N. A. Kotov, M. Prato, D. M. Guldi, J. P. Wicksted, and A. Hirsch, "Molecular design of strong single-wall carbon nanotube/polyelectrolyte multilayer composites," *Nat Mater*, vol. 1, pp. 190-194, 11/print 2002.
- [147] C. Wang, M. Waje, X. Wang, J. M. Tang, R. C. Haddon, and Yan, "Proton Exchange Membrane Fuel Cells with Carbon Nanotube Based Electrodes," *Nano Letters*, vol. 4, pp. 345-348, 2004/02/01 2004.
- [148] M. Michel, A. Taylor, R. Sekol, P. Podsiadlo, P. Ho, N. Kotov, *et al.*, "High-Performance Nanostructured Membrane Electrode Assemblies for Fuel Cells Made by Layer-By-Layer Assembly of Carbon Nanocolloids," *Advanced Materials*, vol. 19, pp. 3859-3864, 2007.
- [149] W. Li, C. Liang, W. Zhou, J. Qiu, Zhou, G. Sun, *et al.*, "Preparation and Characterization of Multiwalled Carbon Nanotube-Supported Platinum for Cathode Catalysts of Direct Methanol Fuel Cells," *The Journal of Physical Chemistry B*, vol. 107, pp. 6292-6299, 2003/07/01 2003.
- [150] E. Frackowiak, S. Gautier, H. Gaucher, S. Bonnamy, and F. Beguin, "Electrochemical storage of lithium in multiwalled carbon nanotubes," *Carbon*, vol. 37, pp. 61-69, 1// 1999.
- [151] H. Shimoda, B. Gao, X. P. Tang, A. Kleinhammes, L. Fleming, Y. Wu, *et al.*, "Lithium Intercalation into Opened Single-Wall Carbon Nanotubes: Storage Capacity and Electronic Properties," *Physical Review Letters*, vol. 88, p. 015502, 12/14/ 2001.

- [152] R. S. Morris, B. G. Dixon, T. Gennett, R. Raffaele, and M. J. Heben, "High-energy, rechargeable Li-ion battery based on carbon nanotube technology," *Journal of Power Sources*, vol. 138, pp. 277-280, 11/15/ 2004.
- [153] D. N. Futaba, K. Hata, T. Yamada, T. Hiraoka, Y. Hayamizu, Y. Kakudate, *et al.*, "Shape-engineerable and highly densely packed single-walled carbon nanotubes and their application as super-capacitor electrodes," *Nat Mater*, vol. 5, pp. 987-994, 12//print 2006.
- [154] B.-J. Yoon, S.-H. Jeong, K.-H. Lee, H. Seok Kim, C. Gyung Park, and J. Hun Han, "Electrical properties of electrical double layer capacitors with integrated carbon nanotube electrodes," *Chemical Physics Letters*, vol. 388, pp. 170-174, 4/11/ 2004.
- [155] L. Zhang, A. V. Melechko, V. I. Merkulov, M. A. Guillorn, M. L. Simpson, D. H. Lowndes, *et al.*, "Controlled transport of latex beads through vertically aligned carbon nanofiber membranes," *Applied Physics Letters*, vol. 81, pp. 135-137, 2002.
- [156] T. Sugino, T. Yamamoto, C. Kimura, H. Murakami, and M. Hirakawa, "Field emission characteristics of carbon nanofiber improved by deposition of boron nitride nanocrystalline film," *Applied Physics Letters*, vol. 80, pp. 3808-3810, 2002.
- [157] P. M. Ajayan, L. S. Schadler, C. Giannaris, and A. Rubio, "Single-walled carbon nanotube-polymer composites: Strength and weakness," *Advanced Materials*, vol. 12, pp. 750+, May 2000.
- [158] G. B. Rossi, G. Beaucage, T. D. Dang, and R. A. Vaia, "Bottom-Up Synthesis of Polymer Nanocomposites and Molecular Composites: Ionic Exchange with PMMA Latex," *Nano Letters*, vol. 2, pp. 319-323, 2002/04/01 2002.

- [159] O. K. Abudayyeh, N. D. Gapp, G. K. Bradsahw, D. M. Wilt, S. M. Han, "Spray-Coated Carbon-Nanotubes for Crack-Tolerant Metal Matrix Composites as Photovoltaic Gridlines," in *2016 Ieee 43 rd Photovoltaic Specialist Conference*, Portland, OR, 2016.
- [160] L. Schlapbach and A. Zuttel, "Hydrogen-storage materials for mobile applications," *Nature*, vol. 414, pp. 353-358, 11/15/print 2001.
- [161] B. S. Sherigara, W. Kutner, and F. D'Souza, "Electrocatalytic Properties and Sensor Applications of Fullerenes and Carbon Nanotubes," *Electroanalysis*, vol. 15, pp. 753-772, 2003.
- [162] F. Valentini, S. Orlanducci, M. L. Terranova, A. Amine, and G. Palleschi, "Carbon nanotubes as electrode materials for the assembling of new electrochemical biosensors," *Sensors and Actuators B: Chemical*, vol. 100, pp. 117-125, 6/1/ 2004.
- [163] J. Liu, A. G. Rinzler, H. Dai, J. H. Hafner, R. K. Bradley, P. J. Boul, *et al.*, "Fullerene Pipes," *Science*, vol. 280, pp. 1253-1256, 1998-05-22 00:00:00 1998.
- [164] H. Hiura, T. W. Ebbesen, and K. Tanigaki, "Opening and purification of carbon nanotubes in high yields," *Advanced Materials*, vol. 7, pp. 275-276, 1995.
- [165] S. W. Lee, B.-S. Kim, S. Chen, Y. Shao-Horn, and P. T. Hammond, "Layer-by-Layer Assembly of All Carbon Nanotube Ultrathin Films for Electrochemical Applications," *Journal of the American Chemical Society*, vol. 131, pp. 671-679, 2009/01/21 2009.
- [166] N. Nakashima, Y. Tomonari, and H. Murakami, "Water-Soluble Single-Walled Carbon Nanotubes via Noncovalent Sidewall-Functionalization with a Pyrene-Carrying Ammonium Ion," *Chemistry Letters*, vol. 31, pp. 638-639, 2002.

- [167] A. Satake, Y. Miyajima, and Y. Kobuke, "Porphyrin–Carbon Nanotube Composites Formed by Noncovalent Polymer Wrapping," *Chemistry of Materials*, vol. 17, pp. 716-724, 2005/02/01 2005.
- [168] Y. Xing, L. Li, C. C. Chusuei, and R. V. Hull, "Sonochemical Oxidation of Multiwalled Carbon Nanotubes," *Langmuir*, vol. 21, pp. 4185-4190, 2005/04/01 2005.
- [169] S. C. Tsang, Y. K. Chen, P. J. Harris, and M. L. Green, "A Simple Chemical Method of Opening and Filling Carbon Nanotubes," *Nature*, vol. 372, pp. 159-162, 1994.
- [170] P. M. Ajayan, T. W. Ebbesen, T. Ichihashi, S. Iijima, K. Tanigaki, and H. Hiura, "Opening carbon nanotubes with oxygen and implications for filling," *Nature*, vol. 362, pp. 522-525, 04/08/print 1993.
- [171] Y. Xing, "Synthesis and Electrochemical Characterization of Uniformly-Dispersed High Loading Pt Nanoparticles on Sonochemically-Treated Carbon Nanotubes," *The Journal of Physical Chemistry B*, vol. 108, pp. 19255-19259, 2004/12/01 2004.
- [172] T. Ramanathan, F. T. Fisher, R. S. Ruoff, and L. C. Brinson, "Amino-functionalized carbon nanotubes for binding to polymers and biological systems," *Chemistry of Materials*, vol. 17, pp. 1290-1295, Mar 2005.
- [173] S. Osswald, M. Havel, and Y. Gogotsi, "Monitoring oxidation of multiwalled carbon nanotubes by Raman spectroscopy," *Journal of Raman Spectroscopy*, vol. 38, pp. 728-736, Jun 2007.
- [174] K. Kinoshita, *Carbon: Electrochemical and Physicochemical Properties*. New York: Wiley, 1988.

- [175] Z. C. Wu, Z. H. Chen, X. Du, J. M. Logan, J. Sippel, M. Nikolou, *et al.*, "Transparent, conductive carbon nanotube films," *Science*, vol. 305, pp. 1273-1276, Aug 2004.
- [176] Y. Kim, N. Minami, W. H. Zhu, S. Kazaoui, R. Azumi, and M. Matsumoto, "Langmuir-Blodgett films of single-wall carbon nanotubes: Layer-by-layer deposition and in-plane orientation of tubes," *Japanese Journal of Applied Physics Part I-Regular Papers Short Notes & Review Papers*, vol. 42, pp. 7629-7634, Dec 2003.
- [177] X. Kang, Z. Mai, X. Zou, P. Cai, and J. Mo, "A sensitive nonenzymatic glucose sensor in alkaline media with a copper nanocluster/multiwall carbon nanotube-modified glassy carbon electrode," *Anal Biochem*, vol. 363, pp. 143-50, Apr 1 2007.
- [178] B. G. Prevo and O. D. Velev, "Controlled, rapid deposition of structured coatings from micro- and nanoparticle suspensions," *Langmuir*, vol. 20, pp. 2099-2107, Mar 2004.
- [179] N. Ferrer-Anglada, M. Kaempgen, V. Skakalova, U. Dettlaff-Weglikowska, and S. Roth, "Synthesis and characterization of carbon nanotube-conducting polymer thin films," *Diamond and Related Materials*, vol. 13, pp. 256-260, Feb 2004.
- [180] M. Kaempgen, U. Dettlaff, and S. Roth, "Characterization of carbon nanotubes by optical spectra," *Synthetic Metals*, vol. 135, pp. 755-756, Apr 2003.
- [181] E. Ramasamy, W. J. Lee, D. Y. Lee, and J. S. Song, "Spray coated multi-wall carbon nanotube counter electrode for tri-iodide (I<sup>3(-)</sup>) reduction in dye-sensitized solar cells," *Electrochemistry Communications*, vol. 10, pp. 1087-1089, Jul 2008.
- [182] *Carboxylic acid*. Available: [https://en.wikipedia.org/wiki/Carboxylic\\_acid](https://en.wikipedia.org/wiki/Carboxylic_acid)

- [183] D. M. Kuncicky, R. R. Naik, and O. D. Velev, "Rapid Deposition and Long-Range Alignment of Nanocoatings and Arrays of Electrically Conductive Wires from Tobacco Mosaic Virus," *Small*, vol. 2, pp. 1462-1466, 2006.
- [184] P. Jiang, J. F. Bertone, K. S. Hwang, and V. L. Colvin, "Single-Crystal Colloidal Multilayers of Controlled Thickness," *Chemistry of Materials*, vol. 11, pp. 2132-2140, 1999/08/01 1999.
- [185] Z.-Z. Gu, A. Fujishima, and O. Sato, "Fabrication of High-Quality Opal Films with Controllable Thickness," *Chemistry of Materials*, vol. 14, pp. 760-765, 2002/02/01 2002.
- [186] A. S. Dimitrov and K. Nagayama, "Continuous convective assembling of fine particles into two-dimensional arrays on solid surfaces," *Langmuir*, vol. 12, pp. 1303-1311, Mar 1996.
- [187] M. Binda. (2011). *Organic Electronics: principles, devices and applications*. Available:  
<https://www.researchgate.net/file.PostFileLoader.html?id=550c9ed2d4c118d5298b467a&assetKey=AS%3A273739944529946%401442276098099>
- [188] E. J. Lavernia and Y. Wu, "Spray Atomization and Deposition," ed Chichester: John Wiley, 1996, pp. 50–153.
- [189] *SPRAY FORMING*. Available:  
[http://materials.iisc.ernet.in/~govind/spray\\_forming.htm](http://materials.iisc.ernet.in/~govind/spray_forming.htm)
- [190] V. Sivadas, M. V. Heitor, and R. Fernandes, "A Functional Correlation for the Primary Breakup Processes of Liquid Sheets Emerging From Air-Assist Atomizers," *Journal of Fluids Engineering*, vol. 129, pp. 188-193, 2006.

- [191] *Methods of Powder Production.* Available:  
<http://www.lpwtechnology.com/technical-library/technical-information/methods-of-powder-production/>
- [192] *Methods of metal powders production.* Available:  
<http://www.netramm.com/eng/tecnology/ch.htm>
- [193] N. Dombrowski and W. R. Johns, "THE AERODYNAMIC INSTABILITY AND DISINTEGRATION OF VISCOUS LIQUID SHEETS," *Chemical Engineering Science*, vol. 18, pp. 203-&, 1963.
- [194] E. Klar and J. W. Fesko, *Gas and water atomization Metals Handbook*, 9 ed. vol. 7. OH, USA: American Society for Metals, 1984.
- [195] M. A. Weiss and C. H. Worsham, "Atomization in High Velocity Airstreams," *Ars Journal* vol. 29, pp. 252-259, 1959.
- [196] K. Y. Kim and W. R. Marshall, "DROP-SIZE DISTRIBUTIONS FROM PNEUMATIC ATOMIZERS," *Aiche Journal*, vol. 17, pp. 575-&, 1971.
- [197] V. Scardaci, R. Coull, P. E. Lyons, D. Rickard, and J. N. Coleman, "Spray Deposition of Highly Transparent, Low-Resistance Networks of Silver Nanowires over Large Areas," *Small*, vol. 7, pp. 2621-2628, Sep 2011.
- [198] R. H. Fernando, L. L. Xing, and J. E. Glass, "Rheology parameters controlling spray atomization and roll misting behavior of waterborne coatings," *Progress in Organic Coatings*, vol. 40, pp. 35-38, Dec 2000.
- [199] J. E. Glass, *Technology for Waterborne Coatings*. Washington, DC: American Chemical Society, 1997.

- [200] M. Majumder, C. Rendall, M. Li, N. Behabtu, J. A. Eukel, R. H. Hauge, *et al.*, "Insights into the physics of spray coating of SWNT films," *Chemical Engineering Science*, vol. 65, pp. 2000-2008, Mar 2010.
- [201] D. C. Law, R. R. King, H. Yoon, M. J. Archer, A. Boca, C. M. Fetzer, *et al.*, "Future technology pathways of terrestrial III-V multijunction solar cells for concentrator photovoltaic systems," *Solar Energy Materials and Solar Cells*, vol. 94, pp. 1314-1318, Aug 2010.
- [202] H. Yoon, M. Haddad, S. Mesropian, J. Yen, K. Edmondson, D. Law, *et al.*, "PROGRESS OF INVERTED METAMORPHIC III-V SOLAR CELL DEVELOPMENT AT SPECTROLAB," in *Pvsc: 2008 33rd Ieee Photovoltaic Specialists Conference, Vols 1-4*, ed New York: Ieee, 2008, pp. 82-87.
- [203] O. K. Abudayyeh, G. K. Bradshaw, S. Whipple, D. M. Wilt, S. M. Han, "Crack-Tolerant Silver-Carbon-Nanotube Metal Matrix Composites as Photovoltaic Gridlines " *Ieee Journal of Photovoltaics*, 2016 (in review).
- [204] C. G. Zimmermann, "Performance Mapping of Multijunction Solar Cells Based on Electroluminescence," *Ieee Electron Device Letters*, vol. 30, pp. 825-827, Aug 2009.
- [205] T. Kirchartz, A. Helbig, and U. Rau, "Note on the interpretation of electroluminescence images using their spectral information," *Solar Energy Materials and Solar Cells*, vol. 92, pp. 1621-1627, Dec 2008.
- [206] L. J. Kong, Z. M. Wu, S. S. Chen, Y. Y. Cao, Y. Zhang, H. Li, *et al.*, "Performance evaluation of multi-junction solar cells by spatially resolved electroluminescence microscopy," *Nanoscale Research Letters*, vol. 10, pp. 1-7, Feb 2015.



- [207] H. Nessim, P. Lugli, A. W. Bett, and C. G. Zimmermann, "Electroluminescence and Photoluminescence Characterization of Multijunction Solar Cells," *Ieee Journal of Photovoltaics*, vol. 3, pp. 353-358, Jan 2013.
- [208] J. R. Mileham, S. J. Pearton, C. R. Abernathy, J. D. MacKenzie, R. J. Shul, and S. P. Kilcoyne, "Patterning of AlN, InN, and GaN in KOH-based solutions," *Journal of Vacuum Science & Technology a-Vacuum Surfaces and Films*, vol. 14, pp. 836-839, May-Jun 1996.
- [209] C. Youtsey, I. Adesida, and G. Bulman, "Highly anisotropic photoenhanced wet etching of n-type GaN," *Applied Physics Letters*, vol. 71, pp. 2151-2153, Oct 1997.
- [210] *Measurement of Solar Cell Efficiency*. Available: <http://pveducation.org/pvcdrom/characterisation/measurement-of-solar-cell-efficiency>
- [211] *IV Curve*. Available: <http://www.pveducation.org/pvcdrom/iv-curve>
- [212] *Dark IV Measurements*. Available: <http://pveducation.org/pvcdrom/characterisation/dark-iv-testing>
- [213] T. Fuyuki and A. Kitiyanan, "Photographic diagnosis of crystalline silicon solar cells utilizing electroluminescence," *Applied Physics a-Materials Science & Processing*, vol. 96, pp. 189-196, Jul 2009.
- [214] K. R. McIntosh and C. B. Honsberg, "The Influence of Edge Re-combination on a Solar Cell's Iv Curve," in *16th European Photovoltaic Solar Energy Conference*, 2000.

- [215] P. P. Altermatt, G. Heiser, and M. A. Green, "Numerical quantification and minimization of perimeter losses in high-efficiency silicon solar cells," *Progress in Photovoltaics*, vol. 4, pp. 355-367, Sep-Oct 1996.